Astrophysics with White Dwarfs

by

Jasonjot Singh Kalirai

B.Sc., The University of British Columbia, 2000
M.Sc., The University of British Columbia, 2001

A THESIS SUBMITTED IN PARTIAL FULFILMENT OF
THE REQUIREMENTS FOR THE DEGREE OF

DOCTOR OF PHILOSOPHY

in

The Faculty of Graduate Studies

(Department of Physics and Astronomy)

We accept this thesis as conforming
to the required standard

....

....

....

....

THE UNIVERSITY OF BRITISH COLUMBIA

September 28, 2004

In presenting this thesis in partial fulfilment of the requirements for an advanced degree at the University of British Columbia, I agree that the Library shall make it freely available for reference and study. I further agree that permission for extensive copying of this thesis for scholarly purposes may be granted by the head of my department or by his or her representatives. It is understood that copying or publication of this thesis for financial gain shall not be allowed without my written permission.

(Signature) _____

Department of Physics and Astronomy

The University Of British Columbia
    Vancouver, Canada

Date _____

Abstract

White dwarfs are the end products of the entire stellar evolutionary process in all intermediate and low mass stars. Over 99% of all stars in our Galaxy will eventually end their lives as white dwarfs. Observationally, studying white dwarfs has proven to be very difficult, primarily due to the faintness of the objects. Bright white dwarfs with $M_V = 11$ have a luminosity only 1/300th of the Sun's intrinsic brightness, while the faintest white dwarfs are $100{,}000\times$ fainter than the Sun. In this thesis, we describe three related projects aimed at better understanding white dwarfs themselves, as well as their role as inhabitants of our Galaxy. The data that we have acquired to study these faint stars are of unprecedented quality and depth, thereby making possible several scientific results that have eluded investigation in decades of previous effort. First, we provide new insight into one of the most important questions in astrophysics today, what is the nature of the dark matter? Specifically, we are able to marginally rule out the most likely candidates based on microlensing results, namely white dwarfs, as a strong contribution to the dark matter. This study represents the deepest ever look into the Galactic halo and uses *Hubble Space Telescope (HST)* data. Secondly, we present results from the continuing study of open star clusters in the *Canada France Hawaii Telescope (CFHT)* Open Star Cluster Survey. This work has improved the quality of the photometry of open star clusters by over an order of magnitude compared to what had been previously possible. We present our findings for two very young clusters, NGC 2168 (M35) and NGC 2323 (M50), including a study of their white dwarf populations. These two clusters, and the white dwarfs that we have found within them, will prove to be crucial in constraining one of the most fundamental relations in stellar evolution, the initial-final mass relationship. In the third project, we use the 8-metre *Gemini North* and 10-metre *Keck* telescopes to simultaneously obtain spectra for 22 white dwarfs in the rich cluster NGC 2099. This work represents a planned follow-up study of the white dwarfs in the richest clusters that we identified in the *CFHT* Open Star Cluster Survey, and has produced several interesting results. First, all white dwarfs in this cluster are hydrogen rich suggesting perhaps that the ratio of hydrogen to helium white dwarfs is different in clusters than in the field, or that all massive white dwarfs are hydrogen rich. Secondly, the NGC 2099 white dwarfs provide the first ever confirmation of a white dwarf cooling age for a star cluster. Thirdly, with just this one cluster, we

are able to almost double the number of white dwarfs that exist on the initial-final mass plane, and provide very strong, tight constraints on a key part of the initial-final mass relationship. The previous constraints on this relationship, which show a large scatter, had taken over 30 years to establish. Our findings directly show that stars with masses between 2.8–3.5 $M_\odot$ lose 75% of their mass through stellar evolution. Additionally, for the first time, we are beginning to see the effects of metallicity on the initial-final mass relationship. Finally, we are now in a position to obtain further spectroscopy of white dwarfs in the other rich clusters that we have imaged with *CFHT*, and, in the very near future, plan to put over 100 data points on the initial-final mass plane.

Contents

List of Tables

List of Figures

Preface

In accordance with the University of British Columbia thesis regulations, a summary of publications which have resulted from this work is presented to the reader. The work has all been completed under the supervision of Harvey Richer and the guidance of the co-authors. The thesis author's role in this work involved the reduction of the data, discovery of results, and the writing of the papers unless noted otherwise. The co-authors helped in interpreting the results and making suggestions/corrections to the work. Co-authors were also involved in data acquisition. This statement is understood and agreed upon by all of the co-authors' who contributed to these projects.

The first project that will be described in this thesis, the search for Galactic dark matter white dwarfs, is published in the Astrophysical Journal (Kalirai et al. 2004, ApJ, 601, 277). The second project describes continuing results from the *CFHT* Open Star Cluster Survey, for which the thesis author is the principal investigator. This Survey has so far resulted in six publications, for all of which the thesis author is first author. Most of that work comprised the author's MSc thesis at UBC. The relevant publications for this PhD thesis are the results from the analysis of NGC 2099 (Kalirai et al. 2001, 122, 3239), and the analysis of the young clusters NGC 2168 and NGC 2323 (Kalirai et al. 2003, AJ, 126, 1402). Other results, such as the numerical simulation of cluster colour-magnitude diagrams (CMDs) presented in Kalirai & Tosi (2004), MNRAS, 351, 649, are touched upon briefly in this work. A paper describing the third and final project in this thesis, spectroscopic observations of white dwarfs, is currently being prepared for submission in the Astrophysical Journal.

The thesis author has presented this research at various conferences, both local and international. I have given seven oral presentations and three poster presentations since the start of my PhD program, three years ago.

Acknowledgements

First and foremost, I wish to thank my supervisor, and good friend, Harvey Richer. You have always given me the freedom to choose my projects and helped me beyond what I can ever thank you for. You have provided me with more support than most graduate students ever receive and always encouraged me to do the best I can. Thank you.

I would also like to very much thank my family. My parents, brother, and sister always stood by me with pride as I followed a path that is outside the conventional stream, especially in our culture.

To my wife, Mandeep, I owe my inspiration and motivation to succeed. You are my best friend and have made the last four years of my life unlike any others. Thanks for everything.

I would like to acknowledge guidance from the many collaborators that I have worked with during my PhD, Harvey Richer, Brad Hansen, Pierre Bergeron, Greg Fahlman, Brad Gibson, Rodrigo Ibata, Peter Stetson, Michael Shara, Mike Rich, David Reitzel, Jarrod Hurley, Marco Limongi, Ivo Saviane, Robert Ferdman, Jason Rowe, Mark Huber, Paolo Ventura, and Ted von Hippel. All of you are responsible for my success.

To Harvey Richer, Jaymie Matthews, and Greg Fahlman, thanks for all the reference letters! To my thesis committee, thanks for all the revisions and corrections to the first versions of this thesis. I have received numerous types of funding through my PhD, mostly from the Natural Sciences and Engineering Research Council of Canada (NSERC) and the University of British Columbia (UBC) and so I thank these organizations for their support of my research. I would also like to thank both the Canada France Hawaii Telescope Corporation and the *Gemini North* telescope for granting me enough observing time so that I could carry out my research projects.

Finally, I would like to extend my gratitude to my friends and the lifelong members of EIP for their support.

Dedication

I would like to dedicate this thesis to my father, the most honest person that I know. You are truly the greatest role model that I have ever known. Thank you for always encouraging me and providing me with the support that I needed to succeed.

Chapter 1

Introduction

1.1   A Very Brief History

The observational discovery of white dwarfs began in 1834 when Friedrich Wilhelm Bessel noticed that the motion of the brightest star in the night sky, Sirius, was irregular. Sirius appeared to "wobble" in the sky, thereby suggesting that in fact the star is one component of a binary system. Using observations carried out from 1834 to 1844, Bessel (1844) concluded that the binary system of Sirius and its unseen companion revolved around one another with a period of about 50 years. However, it was not until January 31, 1862, that Alvan Graham Clark first imaged the faint companion (called Sirius B) using a new 18-inch telescope built for the Dearborn Observatory (Clark 1862).

Sirius A and B have a luminosity ratio of about 10^4, yet the colours of the two stars were noticed to be quite similar. To first order, similar colours indicate similar temperatures, and therefore it was estimated that the radius of Sirius B was about 100 times smaller than Sirius A (through $L = 4\pi R^2 \sigma T^4$). This was confirmed in 1915 when Walter Sydney Adams measured the first spectrum of Sirius B and confirmed that it was, in fact, a blue star (Adams 1915). The first white dwarf had been discovered, an object as massive as the Sun, yet only as large as the Earth. By 1925, Adams measured a gravitational redshift from Sirius B, thereby simultaneously confirming the very dense nature of this object (about 1×10^6 g/cm^3) and providing a successful test to Einstein's theory of relativity (Adams 1925). This then spurred a number of very important theoretical advancements to try and understand these objects, and in particular to understand the relativistic electron degeneracy equation of state (see e.g., Chandrasekhar 1937).

Since the discovery of the first white dwarf, over 3000 of these objects have been discovered in our Galaxy (see McCook & Sion 1999 and on-line updates). The Sloan Digital Sky Survey has already almost doubled this number, and will easily find 10000 new white dwarfs by the end of the Survey (Kleinman et al. 2004). With more new discoveries, the astrophysical uses of these objects continue to grow.

1.2 What are White Dwarfs?

Normal hydrogen burning stars (main-sequence stars) are in a state of hydrostatic equilibrium. The radially inward directed gravitational force is balanced by a thermal pressure exerted from the nuclear reactions occuring in the core of the star. The thermal timescales in a main-sequence star are much greater than dynamical timescales, and therefore the equilibrium holds as long as the star continues to burn hydrogen. However, a star eventually exhausts almost all of its core hydrogen supply and the previously established equilibrium is destroyed. The rate of this hydrogen burning depends almost entirely on the mass of the star, and the subsequent evolution of the star depends on its initial mass. The star will move through many post-main sequence stellar evolutionary stages, such as the sub-giant branch, red giant branch, horizontal branch (or red giant clump in the case of stars with initial masses $< 2 \; M_\odot$), asymptotic giant branch, planetary nebula stage, and finally the white dwarf stage (in the case of stars with initial masses $\leq 7 \; M_\odot$). Details of each of these stages can be found in the very thorough review of Chiosi, Bertelli & Bressan (1992). The end product of this chain of events is a "stellar cinder" which fades with time, becoming dimmer by radiating away any remaining stored thermal energy. We illustrate the locations of these phases and the evolution of a single star which will produce a white dwarf in a Hertzsprung-Russell (HR) diagram in Figure 1.1.

With all of the nuclear fuel exhausted, a white dwarf cannot generate pressure from reactions in the core. Earlier in the evolution, all of the hydrogen (and helium) were burnt and converted into carbon and oxygen. The resulting C/O core cannot support itself from gravitational contraction and therefore gravity compresses the star. The electrons in the core are packed together tighter and tighter. The Pauli exclusion principle only allows two electrons, of different spin, to occupy any energy level and therefore all of the energy levels from the ground level up are filled and the electron gas is said to be degenerate. Invoking the Uncertainty Principle, the space available to each electron, Δx, becomes very small in a white dwarf and therefore the momentum, p, is very large. It is this momentum that generates a degeneracy pressure that supports the star from further collapse. The typical mass of the resulting star is 0.6 $M_\odot$, with a radius of 10^4 km (i.e., $\rho \sim 10^8$ kg/m^3). More detailed properties of white dwarfs can be found in the excellent textbook by Shapiro & Teukolsky (1983).

Several interesting properties exist for degenerate matter. For example, if the mass of the white dwarf is increased, then the electrons are forced to "squeeze" together even more and consequently the radius of the star actually decreases. Therefore, more massive white dwarfs are smaller. Another property of white dwarfs, determined by Chandrasekhar (1937), is that they have a maximum mass. If enough mass is piled onto a white dwarf,
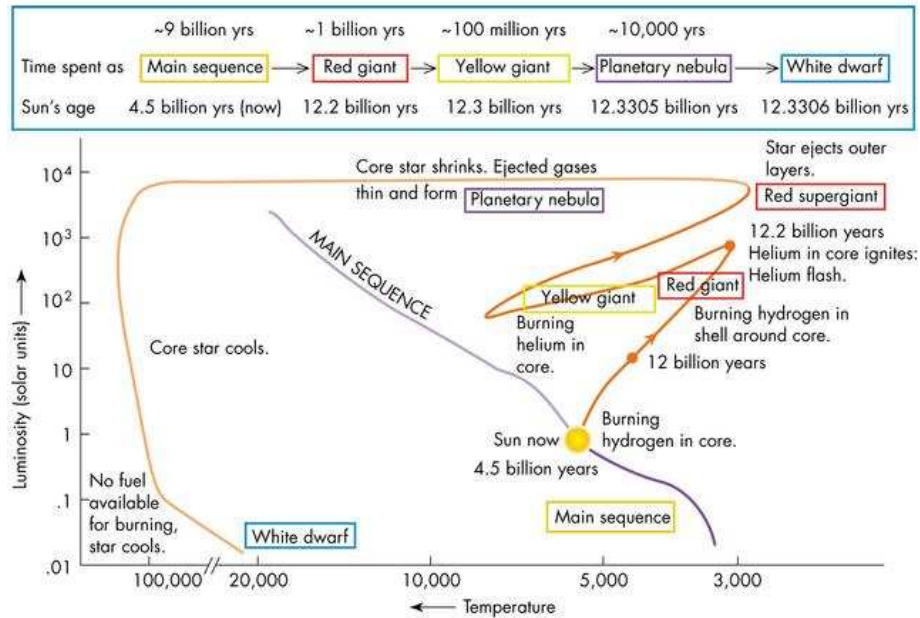
Figure 1.1: A Hertzsprung-Russell diagram is shown with the main sequence, post main sequence stellar evolutionary phases, and white dwarf cooling phase indicated. The evolution shown is for a 1 $M_\odot$ star.

the velocity of the electrons continues to increase until they approach the speed of light, at which point degenerate electron pressure can no longer support the star from further collapse. This maximum mass can be easily shown to be $\sim 1.4\ M_\odot$, and if reached, results in a type Ia supernova explosion of the star. These explosions occur when massive white dwarfs are members of close binary systems, in which the white dwarf accretes mass from a companion, pushing it over what is now called the "Chandrasekhar limit". Interestingly, an even more extreme type of degeneracy pressure governs the stability of neutron stars, the end products of more massive initial main-sequence stars that do not produce white dwarfs. In that regime, the densities are so high ($\rho \sim 10^{17}\ \mathrm{kg/m^3}$) that protons and electrons will combine through inverse beta decay to produce neutrons which support the star through degenerate neutron pressure. Observationally, most neutron stars are found to have a mass of about 1.5 $M_\odot$ and a radius of only 10 km! More information on neutron stars can be found in the review by Srinivasan (2002).

White dwarfs are found in many flavours. The most common spectral designations are DA, for those stars showing prominent hydrogen Balmer absorption features as in A type main-sequence stars, and DB, for those showing prominent helium (I) lines as in

B type main-sequence stars. The "D" designates that the object is degenerate. Very hot white dwarfs ($>$ 80,000 K) just beginning their evolution from the planetary nebula stage are labelled DO and show He (II) absorption lines. At the opposite regime of very cool temperatures ($<$ 5,000 K), both hydrogen and helium lines are invisible in the spectra of white dwarfs; these featureless spectra are designated DC. Slightly hotter helium rich white dwarfs are also designated DC, as they also do not show any absoption lines. Other designations include DQ white dwarfs (those with carbon lines), DH white dwarfs (magnetic white dwarfs) and DZ white dwarfs (those with other metal lines). Example spectra of each of these classes can be found in the first data release of the Sloan Digital Sky Survey (Kleinman et al. 2004).

The chemical evolution of white dwarfs is quite complicated and not completely understood (see e.g., Bergeron, Ruiz, & Leggett 1997). White dwarfs are believed to change spectral types, perhaps several times, through their evolution. The distribution of white dwarfs of various spectral classes as a function of temperature shows several gaps. For example, the DB gap, located at temperatures between 30,000 – 45,000 K, contains no DB white dwarfs. DB white dwarfs are, however, found both above and below the gap. At much cooler temperatures, between 5,000 and 6,000 K, a non-DA gap exists where only DA white dwarfs are present. Overall, the ratio of DA to non-DA white dwarfs is much greater (20:1) than at hot temperatures ($\sim$ 30,000 K). However, the DB and DC spectral type are abundant at cooler temperatures and the ratio drops to only 2:1 at temperatures under 10,000 K. It is believed that DA white dwarfs can have either thin ($10^{-10} M_{\odot}$) or thick ($10^{-4} M_{\odot}$) hydrogen surface layers. In the cases of thick surface layers, the stars will always remain of DA spectral type. However, for thin hydrogen layers, it is possible that the hydrogen layer mixes with the underlying more massive helium mantle ($10^{-2} M_{\odot}$) and is drowned out. This convective mixing requires cool temperatures and is a possible explanation for the abundance of cool non-DA white dwarfs. The non-DA gap may be explained by hydrogen accretion from the interstellar medium or from some yet unknown type of dilution or mixing of hydrogen and helium in that narrrow temperature range. More information on these issues as well as other parameters of white dwarfs can be found in the review paper by Fontaine, Brassard, & Bergeron (2001). Continued observations, such as those presented in this thesis, will help resolve these problems.

1.3   White Dwarfs as Interesting Objects

Over 99% of all stars will eventually end their lives as white dwarfs. These faint stellar remnants can be used in many different investigations. For example, white dwarfs cool with time in a predictable way. Recently, this white dwarf cooling process has been

used to date the globular star cluster M4 (Hansen et al. 2004; Hansen et al. 2002) and independently determine the age of the Galactic halo. The same study also used white dwarfs to determine the mass function of the cluster above the main-sequence turn-off (Richer et al. 2004; Richer et al. 2002). Since all stars with a mass above 0.8 $M_\odot$ have evolved off the main-sequence in a 12 Gyr population, white dwarfs represent our only link to the distribution of stars (i.e., the initial mass function) of intermediate and massive stars in these systems. White dwarfs are also astrophysically important when considering the chemical evolution of the Galaxy. All stars with an initial mass up to 7 or 8 $M_\odot$ will end up becoming white dwarfs with a final mass less than 1.4 $M_\odot$. Therefore, many solar masses of material will be expelled into the interstellar medium during a star's evolution and therefore affect future nucleosynthesis and star formation. A characterization of this mass loss, the initial-final mass relationship, remains today as one of the most poorly understood aspects of stellar evolution.

Recently, the possible nature of white dwarfs as Galactic dark matter candidates has been suggested by Alcock et al. (2000). Microlensing events towards the Large Magellanic Clouds suggest that approximately 20% of our Galactic halo is filled with 0.5 $M_\odot$ objects. A successful search for these objects by Oppenheimer et al. (2001) temporarily solved this long-standing problem. However, reanalysis of the results by several groups suggest that in fact Oppenheimer's population is not of halo origin and is more likely from a thick disk. Still, white dwarfs have not been excluded as a possible component of the Galactic dark matter.

Although white dwarfs are faint, studying them is becoming easier with larger telescopes and improved instrumentation. The few reasons listed above do not do justice to the number of interesting scientific developments that have resulted from studying white dwarfs. These studies range from using asteroseismology to probe the inner structure of these objects (see e.g., Kawaler 1995, Fontaine & Brassard 1994), to improving models of white dwarf cooling and atmospheres (Hansen 1999; Bergeron, Saumon, & Wesemael 1995; Wood 1995), to understanding the physics of matter at extreme densities, to using white dwarfs to determine the lower mass limit to type II supernovae (see e.g., Kaspi & Helfand 2002).

1.4   Format of Thesis

In this thesis, I will describe three individual projects related to studying white dwarfs. The data sets that we reduced to study white dwarfs were all very rich, and therefore a number of side projects and secondary science were done along the way. Occasionally, I will digress away from white dwarfs to discuss, for example, a measurement of the circular

speed of our Sun around the Galaxy, or look at dynamics in very young star clusters. These short sections will not detract from the central goal of the thesis, to carry out astrophysical studies with white dwarfs. The projects all combine various astrophysical techniques, such as imaging and spectroscopy, and ground- and space-based observations. Because of this, I have written three long chapters describing each study in turn, as opposed to individual chapters on the data reduction, calibration, results, etc. Each of these three chapters is therefore self-contained in the methods that were used to reduce the data and find scientific results for that particular study. The first project, the search for Galactic dark matter white dwarfs, is presented in Chapter 2, and is a space-based imaging study. Following this, I will discuss a ground based imaging study of white dwarfs in open star clusters in Chapter 3. Chapter 4 will present new results from a spectroscopic study of white dwarfs. In Chapter 5 I conclude the thesis and tie these projects together into a broader astrophysical picture. On-going studies as well as future prospects will also be discussed.

Chapter 2

White Dwarfs in the Field

2.1   Introduction

A recent *Hubble Space Telescope (HST)* imaging project of the Galactic globular cluster
Messier 4 (GO 8679) has investigated both the low-mass end of the hydrogen burning
main sequence (Richer et al. 2004) and the faint end of the white dwarf cooling sequence
(Hansen et al. 2004). Messier 4 (M4) is the closest globular cluster to us, and therefore
is more appealing for faint studies. The data for the cluster members were isolated from
background/foreground contaminants by using the proper motion of the cluster with re-
spect to the field over a 6 year baseline (previous epoch data obtained with *HST* in cycle
4, 1995 – Ibata et al. 1999; Richer et al. 1997; Richer et al. 1995). In this contribution,
we shift our focus to the background contamination itself (the spheroid and galaxies) and
isolate these populations for investigation.

Stars, gas and dust in the disk, bulge and spheroid of our Galaxy only account for
$\sim 10\%$ of the total mass within $R = 50$ kpc (Wilkinson & Evans 1999). The remaining
mass is believed to reside in the dark halo of our Galaxy (dark matter), and determining
the nature of this mass is a critical issue today in astrophysics. Recently, a project called
"the MACHO project" has analyzed data from microlensing events in the direction of the
LMC and determined that the mean mass of 20% of the lenses is 0.5 ± 0.3 $M_\odot$ (Alcock
et al. 2000). These lenses are referred to as MACHOs (MAssive Compact Halo Objects),
and the leading candidates as the source of these lenses are white dwarfs. Even if the
MACHOs cannot account for the total halo dark matter contribution, determining the
properties and number density of faint halo white dwarfs is important in several areas of
astrophysics. These include studying the initial mass function (IMF) of first generation
stars (population III stars) through their remnants and constraining the star-formation
history of our Galaxy.

Studying white dwarfs in the Galactic bulge or spheroid from the ground is difficult

---

[1]A version of this chapter has been published. Kalirai, J.S., Richer, H.B., Hansen, B.M., Stetson, P.B.,
Shara, M.M., Saviane, I., Rich, R. M., Limongi, M., Ibata, R., Gibson, B.K., Fahlman, G.G., and Brewer,
J. (2004) The Galactic Inner Halo: Searching for White Dwarfs and Measuring the Fundamental Galactic
Constant, Θ_0/R_0. Astrophysical Journal, 601: 277-288.

for two reasons. First, the end of the white dwarf cooling sequence for 0.5 $M_\odot$ objects in a population 12 Gyrs old has an absolute visual magnitude of $M_V \sim 17$ (Hansen 1999), which, at the centre of the Galaxy (8 kpc) corresponds to an apparent magnitude of $V > 31.5$. The depth of the M4 study ($V \sim 30$), however, is faint enough to detect the brighter end of this cooling sequence. Secondly, a line of sight through the disk of our Galaxy picks up many foreground metal-rich disk stars, which contaminate the sample. Although observing at higher latitudes above the centre helps avoid the thick disk, the resulting spheroid number density also drops off rapidly, $n(r) \propto r^{-3.5}$ (Binney & Merrifield 1998). With *HST* we can achieve the depth required to measure these faint stars, but there are several disadvantages. First, we are dealing with small-number statistics, due to the limited field of view. The Wide Field Planetary Camera 2 (WFPC2) on *HST* has a field area of 5.7 arcmin^2). More importantly, long exposures pick up many galaxies, such as those seen in the Hubble Deep Field (HDF), which can mimic stars in faint photometry.

Given the caveats listed above, we attempt here to isolate potential white dwarfs in the field by separating out populations using both their morphology and their kinematics. After briefly presenting the data in §2.2, we begin by finding galaxies and establishing our extragalactic zero-motion frame of reference. This then allows us to determine two important quantities: the velocity of the Local Standard of Rest (§2.3.3) and the first measurement of the absolute proper motion of M4 from an extragalactic reference frame (§2.3.4). In §2.4 we examine the different populations which make up the corrected proper-motion and colour-magnitude diagrams and discuss the inferred spheroid population. Next, we analyze faint, blue stars in this population and identify our best candidates for disk and spheroid white dwarfs (§2.5). This includes comparing our results to the expected numbers of white dwarfs, given the searchable volume in our data and the various population-density distributions along the line of sight. In §2.6, we discuss the current status of the search for dark halo white dwarfs, as well as some of the different views which have been presented in the recent literature. The present results are placed in the context of these independent efforts, and we present conclusions in §2.7.

2.2 The Data

The data for the present and previous observations (1995, cycle 4 - Ibata et al. 1999; Richer et al. 1997; Richer et al. 1995) were reduced using the DAOPHOT/ALLSTAR (Stetson 1987) and ALLFRAME (Stetson 1994) photometry packages. We acquired data in both of the wide optical filters F606W (> 35 hours) and F814W (> 53 hours). Individual frames were registered and co-added with the DAOMASTER and MONTAGE2 programs by Dr. James Brewer. The proper motions were determined by centering on the cluster

stars and measuring the apparent motion of the background spheroid stars over the 6 year baseline. This was done in an iterative manner. The ALLSTAR fitted point-spread function was allowed to recenter in determining the center of all stars on each frame. Over the 6 year baseline, the proper motion of the cluster stars compared to the background field stars amounts to about 1 *HST* pixel. To ensure that the individual frames were registered on the cluster stars, we built a transformation file iteratively by only using those stars which don't move little relative to one another. The internal mean motion of the cluster stars is very small given the small cluster velocity dispersion, 3.5 km/s (Peterson, Rees & Cudworth 1995), amounting to only 0.02 pixels over the 6 years. To compensate for distortions in the *HST* optics, we used a 20-term transformation equation (see Richer et al. 2002). The distribution of proper motions as a function of magnitude, and the errors, will be presented later. The final photometry list includes only those stars which were measured in both filters and at both epochs, and which passed a visual inspection. Further details of the reduction and calibration of the data set used in this analysis are described in Richer et al. (2004) (see also §2 of Richer et al. 2002). We summarize the key parameters for both the cluster and field population and present the observational log in Table 2.1.

Field Location:
α(J2000)	RA	$= 16^h23^m54.6^s$
δ(J2000)	declination	$= -26°32'24.3''$
l(J2000)	Galactic longitude	$= 351.01°$
b(J2000)	Galactic latitude	$= 15.91°$

Cluster Distance & Reddening[1] :
$(m-M)_V$	apparent distance modulus	$= 12.51$
$E(B-V)$	reddening	$= 0.35$
A_V	visual extinction	$= 1.32$
$(m-M)_0$	true distance modulus	$= 11.18$
d	distance from Sun	$= 1.72$ kpc

Background Field (Spheroid) Distance & Reddening:
$(m-M)_V$	apparent distance modulus	$= 15.71$
$E(B-V)$	reddening (all in front of M4)	$= 0.35$
A_V	visual extinction	$= 1.32$
$(m-M)_0$	true distance modulus	$= 14.39$
d	tangent point distance	$= 7.6$ kpc
z	projected distance above plane	$= 2.2$ kpc

Metallicity (Cluster[2] & Spheroid:
[Fe/H]	heavy metal abundance	$= -1.3$

Data (GO 5461[3] - cycle 4 & GO 8679 - cycle 9):
No. of Images – F555W - 1995	15×2600 seconds
No. of Images – F606W - 2001	98×1300 seconds
No. of Images – F814W - 1995	9×800 seconds
No. of Images – F814W - 2001	148×1300 seconds

Limiting Magnitude (Based on SEXTRACTOR Classifications):
V	29
I	27.5

Table 2.1: Cluster, field parameters and observational data – 1. Richer et al. (1997), 2. Djorgovski (1993), 3. Ibata et al. (1999)
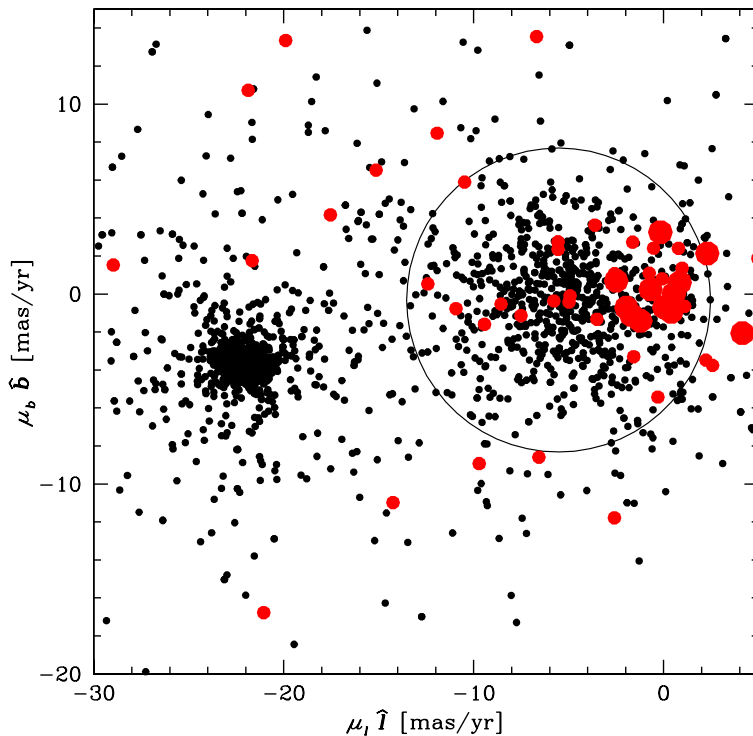
Figure 2.1: The proper-motion diagram for all stars (μ_l, μ_b) is shown with galaxies represented as red dots (see §2.3). The galaxies used to determine the zero-motion reference frame are displayed as larger dots (see §2.3.2). The tighter clump of M4 stars is clearly distinct from the more diffuse spheroid clump.

In Figure 2.1, we present the proper-motion diagram for our data. The motion of the cluster with respect to the field (6 year baseline), can be clearly seen as the tight clump toward negative proper motions. For the units, we first translated the x and y pixel motions into Galactic coordinates (l, b) by using a rotation angle which aligned the y axis of the CCD to the North Galactic Pole. The total proper motion is calculated using μ $= \sqrt{(\mu_l)^2 + (\mu_b)^2}$. We then converted the *HST* WFPC2 pixels into arcseconds using the plate scale (0.″1/pixel, Biretta et al. 2002) of the CCD. The motions are then divided by the baseline of 6 years and converted to mas/yr. Zero motion in the diagram, (μ_l, μ_b) = (0, 0), is centred on well measured, bright galaxies (larger red dots) and is described in detail in §2.3.2.

2.3 An Extragalactic Reference Frame

2.3.1 Measuring Galaxies

Isolating galaxies in the current study is crucial, as they can mimic faint blue white dwarfs in the data. Additionally, since the galaxies are not moving, they represent a fixed zero-motion position in the proper-motion diagram, from which we can measure absolute motions. Visually, the images of M4 show only a small number of obvious galaxies. Were it not for the much larger number of foreground stellar objects, the 1.3 magnitudes of foreground visual extinction and the higher background produced by scattered light and zodiacal light, this image would likely look similar to the HDF (Williams et al. 1996) which shows 1781 galaxies in the range $26 \leq V_{\mathrm{AB}} \leq 29.5$.

To measure galaxies in our field, we used the image morphology classification tool, SEXTRACTOR (Bertin & Arnouts 1996). SEXTRACTOR assigns a stellarity index to each object, which can then be used to distinguish between stars and galaxies. The stellarity is determined through a neural network, which learns based on other, high signal-to-noise, stars. Although SEXTRACTOR was not able to recover statistics for every object that ALLSTAR measured in our data, the classifications are $\sim 75\%$ complete through $V = 24$–29. Fainter than $V = 29$, SEXTRACTOR was only able to measure $\sim 40\%$ of the ALLSTAR sources and struggled to classify objects as stars or galaxies. Altogether, just over 50 galaxies were identified and measured using a stellarity < 0.2 cut (see below).

Figure 2.2 (top) shows the SEXTRACTOR classifications as a function of magnitude for all objects. We also note here that the images used in the analysis were expanded by a factor of 3 ($0.''033$/pixel) to improve centering. The distribution of points on this diagram can be broken into two classes, which are separated by the horizontal lines. The stars are found predominantly in a clump near stellarity $= 1$ down to a magnitude of $V \sim 28$. Fainter than this, the classifications are not as good. However a clump of stars can be seen extending to $V \sim 29$, with a sharp cutoff in stellarity at 0.7. The galaxies are found near the bottom of the figure, at stellarity $\simeq 0$. Here we have chosen a conservative stellarity < 0.2 cut to include possible outliers above the predominant galaxy sequence. Very few objects ($\sim 4\%$ for $V < 29$) are seen between the stars and galaxies, indicating that the classifications are reliable. At the faintest magnitudes, $V \sim 29$, a clump of objects can be seen at stellarity ~ 0.5. This is expected, as the program will, on average, choose stellarity $= 0.5$ for an object which it cannot classify. Therefore this magnitude represents the limit at which we can accurately separate stars from galaxies via morphology.

In Figure 2.2 (bottom) we use the stellarity to illustrate the separate populations in our data. Here, the stellarity of all objects is plotted against the total absolute proper motion, $\mu_{\mathrm{total}} = \sqrt{(\mu_l)^2 + (\mu_b)^2}$, as determined with respect to the centre of the large red
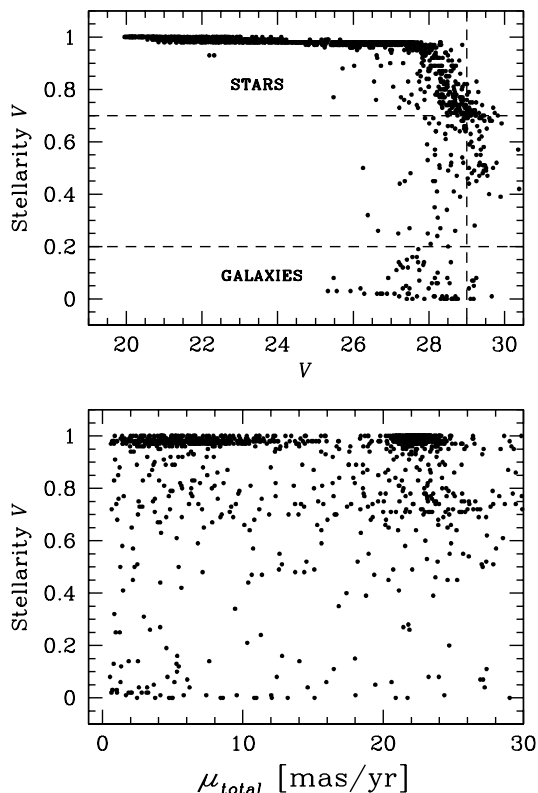
Figure 2.2: *Top* - A plot of stellarity vs magnitude shows that we have clearly separated stars from galaxies down to $V \sim 29$. *Bottom* - The stellarity of all objects is plotted against the total proper-motion displacement ($\mu_{\text{total}} = \sqrt{(\mu_l)^2 + (\mu_b)^2}$), to illustrate the different populations along the M4 line of sight (see §2.3.1).

dots in Figure 2.1. We will justify this location in the next section. First, we note two clear clumps for stars (at constant stellarity $\simeq 1$) representing the cluster ($\mu_{\text{total}} \sim 22.5$ mas/yr, with a small dispersion) and field populations ($\mu_{\text{total}} \sim 5$ mas/yr, with a much larger dispersion). This bi-modality continues for lower stellarities down to stellarity $\simeq$ 0.7. The galaxies (stellarity ~ 0) are obviously found at low μ_{total}. However, a tail is seen to higher proper-motion displacements (these are the small red dots in Figure 2.1). As we will see in §2.3.2, this tail represents the faintest galaxies and indicates that our ability to measure the proper motions has degraded, due to reduced signal-to-noise.

2.3.2   Centering the Zero-Motion Frame of Reference

In Figure 2.1, we showed the locations of bright, well-measured galaxies (large red dots), which represent an absolute background reference frame. As these galaxies clumped together, we first estimated their position and measure the absolute proper motion of all objects with respect to this point.

Figure 2.3 shows the total proper-motion displacement as a function of magnitude for both stars (top) and galaxies (bottom). The distributions are found to be very different. The stars behave as expected, and are confined within a constant envelope in μ_{total} across all but the faintest magnitudes. The two horizontal sequences represent the cluster stars near $\mu_{\text{total}} \sim 22.5$ mas/yr and a more diffuse field star sequence. The latter consists of stars in the disk and spheroid, along this line of sight. Note that the spread in the distribution of M4 cluster members ($\mu_{\text{total}} \sim 22.5$ mas/yr) for $V \geq 28$ is not due to the main-sequence stars. At $V > 28$, the main sequence of M4 contains very few stars (Richer et al. 2002) and so the scatter is due to the faintest white dwarfs in the cluster. On the other hand, the total proper-motion displacement of the galaxies (bottom) is found to completely degrade for $V > 27$. Considering that we know from Figure 2.2 that the stellarities for the galaxies are measured accurately to well beyond this limit, this flaring must be entirely due to difficulties in the astrometric centering on these faint extended sources. Therefore only the galaxies with $V < 27$ should dictate the location of the zero-motion frame, as some of their fainter counterparts have been poorly measured. The centroid of the 12 galaxies which satisfy this criterion represents the zero-motion frame of reference shown on all subsequent proper-motion diagrams (see large red dots in Figure 2.1). The one-dimensional error in this location is calculated as $\sigma/\sqrt{N} \approx 0.5$ mas/yr, where σ is the proper-motion dispersion of the galaxy sample ($\simeq 1.6$ mas/yr).

2.3.3   The Circular-Speed Curve

We now use the extragalactic stationary frame of reference, established above, to measure two important quantities in the next two sub-sections. The first, the circular-speed curve, is a plot of the velocity of a test particle (Θ_0) moving in a circular orbit in the Galactic plane and around the Galactic centre, versus the distance R at which it is located relative to the centre. The ratio of these quantities at the Solar radius ($\Omega_0 = \Theta_0/R_0$) represents one of the more difficult problems in Galactic structure and directly provides the mass interior to R_0. This constant is fundamentally important in understanding the dynamics of the Galactic halo and the Local Group.

For the motion in the Galactic plane, we measure an angular proper motion from the centre of the galaxy clump to the centre of the spheroid clump of $\mu_l = -5.53 \pm 0.50$
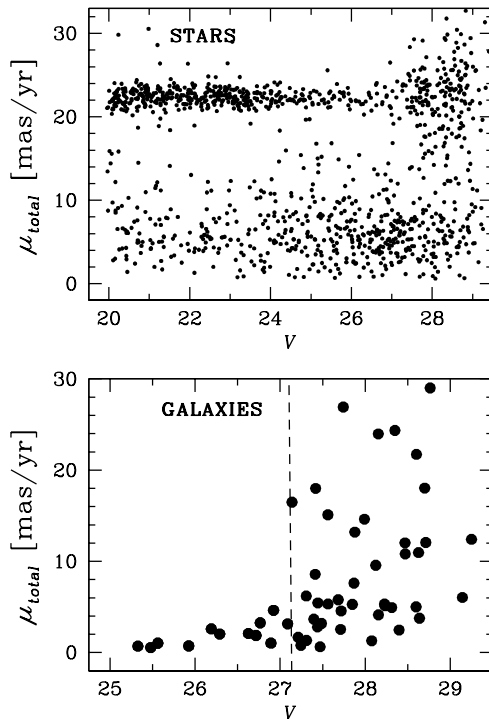
Figure 2.3: The total proper motion displacement is plotted as a function of V magnitude for both stars (*top*) and galaxies (*bottom*), as determined by SEXTRACTOR . The stars are found along two sequences, representing the cluster ($\mu_{\text{total}} \simeq 22.5$ mas/yr) and the spheroid ($\mu_{\text{total}} \simeq 5$ mas/yr) populations. The galaxies are confined to zero motion for $V < 27$, beyond which their astrometry degrades (see §2.3.2). These brightest galaxies are used to define the zero-motion frame of reference.

mas/yr. Assuming the spheroid is not rotating (see below), this represents the reflex motion of the Sun, a combination of the local standard of rest (LSR) circular orbit and the deviation of the Sun from that circular orbit (Solar motion). The uncertainty in this number is derived from the quadrature sum of the dispersions in each of the galaxy and spheroid clumps. We can now orient the known Solar motion $(U_\odot, V_\odot, W_\odot) = (+10.0, +5.2, +7.2)$ km/s (Dehnen & Binney 1998), where $U_\odot$ is positive towards the Galactic centre, $V_\odot$ is in the direction of Galactic rotation, and $W_\odot$ is out of the plane, into the M4 direction. The new U, for example, will be the radial velocity of the Sun, in the direction of M4. The correction term for the Solar motion, $V = -U_\odot \sin(l) + V_\odot \cos(l)$ is calculated to be 6.71 km/s which we can convert to a proper motion, $\Delta\mu_l = 0.19 \pm 0.02$ mas/yr.

Therefore the corrected μ_l = -5.34 $\pm$ 0.50 mas/yr, and $\Omega_0 = \Theta_0/R_0 = -4.74\mu_l = 25.3 \pm$ 2.4 km/s/kpc

The angular velocity of the circular rotation of the Sun can be directly compared to the Oort Constants, A and B (Kerr & Lynden-Bell 1986), which measure the shear and vorticity of the disk. Recent analysis based on *Hipparcos* measurements of 220 Galactic Cepheids gives $\Omega_0 \equiv A-B = 27.19 \pm 0.87$ km/s/kpc (Feast & Whitelock 1997), larger than our value, but consistent within the uncertainty. Other measurements, such as the Sgr A* proper-motion study (Reid et al. 1999), also find a higher value than ours, $\Omega_0 = 27.2 \pm 1.7$ km/s/kpc. At $R_0 = 8.0 \pm 0.5$ kpc, these two measurements give a Solar reflex velocity of $v_{LSR} = \Theta_0 \simeq 218$ km/s, in good agreement with the independent IAU adopted value of 220 ± 15 km/s (Binney & Tremaine 1987), based on kinematics of high velocity stars. However, other studies, such as Kuijken & Tremaine (1994) find much smaller values. Based on a set of self-consistent solutions for different Galactic parameters, they find $v_{LSR} = 180$ km/s. Merrifield (1992) also calculates a lower Local Standard of Rest velocity, $v_{LSR} = 200 \pm 10$ km/s, using rotation of HI layers. For $R_0 = 8.0 \pm 0.5$ kpc, our result gives a similar value to this latter study, $v_{LSR} = 203 \pm 23$ km/s. Only 15% of the uncertainty in our result is contributed by the 0.5 kpc uncertainty in the Galactocentric distance, with the remaining error almost entirely due to the dispersion in the galaxy sample.

Although our value is consistent with all of these studies given the uncertainties, we consider a few explanations for the difference. The choice of galaxies from which we calculate the zero-motion frame of reference has the most serious effect (see §2.3.2). Figure 2.3 (bottom) clearly shows that many fainter galaxies do have a similar motion to the 12 brighter objects. Although we could not separate these from those with degraded proper motions on the basis of independent criteria, including a few of these sources could easily affect the zero-motion position and provide a Solar reflex velocity in better agreement with the higher values ($\simeq 220$ km/s). Another consideration that we are currently investigating is the possible rotation of the spheroid itself, which would cause an over/underestimate of the Solar reflex motion depending on the degree to which stars in front of the tangent point dominate over stars behind it. Given the small field of view, we could also potentially be affected by debris tails or small groups of stars with peculiar orbits.

Despite these caveats, we stress the importance of this new measurement. Kuijken & Tremaine (1994) estimate that if they are correct and a reduction of Θ_0 from 220 km/s to 180 km/s is needed, the line-of-sight velocity of M31 relative to the Galactic centre would correspondingly increase by 25%. This, in turn, would increase the mass of the Local Group from timing arguments by 35%. Although additional methods (see Kuijken & Tremaine 1994 for a summary) to constrain the circular-speed curve are being used

(e.g., using Local Group kinematics, motions of globular clusters or halo stars, tangent-point measurements of the inner rotation curve and outer-rotation curve-measurements using OB stars and HII regions, etc.), they are not superior to measurements made with extragalactic reference frames. Global measurements, such as those of the present work and the Sgr A* proper motions (Backer & Stramek 1999; Reid et al. 1999) avoid Galactic variations in the sample of objects and therefore reduce systematic uncertainties (Binney & Tremaine 1987).

The apparent motion of the spheroid stars in the direction perpendicular to the plane is very small, $\mu_b = -0.32 \pm 0.49$ mas/yr (see Figure 2.1). The correction for the component of the known Solar motion, $v_{Z_\odot} = 7.17 \pm 0.38$ km/s (Dehnen & Binney 1998) in this direction is $\Delta\mu_b = -0.12 \pm 0.01$ mas/yr. Therefore, the residual velocity for $R_0 = 8.0 \pm 0.5$ kpc is found to be 7.4 ± 18.7 km/s, consistent with a stationary population.

2.3.4 The Absolute Proper Motion of M4

The space motions of Galactic globular clusters are of interest in order to constrain and reconstruct their orbits around the Galaxy. This yields important information on cluster origins and destruction processes, as well as galactic dynamics. Formation scenarios of the Galaxy can be better understood by coupling the kinematics of the clusters with other properties, such as the metallicities and ages (Dinescu et al. 1997).

Three primary methods exist to determine the space motions of globular clusters and all involve measuring the absolute proper motion of the stars in the cluster. The indirect methods involve either using secular parallaxes (which require a knowledge of Galactic rotation) or using the new 'bulge-relative' method (which requires the distance and proper motion of the bulge: Terndrup et al. 1998). The preferred method involves using extragalactic objects, galaxies or QSOs, and directly measuring the motion of the cluster.

Only two previous estimates, and one simultaneous one, of the M4 absolute proper motion exist in the literature. Cudworth & Rees (1990) used bright field stars as a reference to the brighter cluster stars to estimate $\mu_\alpha = -11.6 \pm 0.7$ mas/yr, $\mu_\delta = -16.3 \pm 0.9$ mas/yr. Dinescu et al. (1999) used *Hipparcos* field stars as a reference to carefully measure the motion of the cluster after accounting for plate-transformation systematics: $\mu_\alpha = -12.50 \pm 0.36$ mas/yr, $\mu_\delta = -19.93 \pm 0.49$ mas/yr. The Bedin et al. (2003) study finds $\mu_\alpha = -13.21 \pm 0.35$ mas/yr, $\mu_\delta = -19.28 \pm 0.35$ mas/yr using a single QSO in a different field of M4 than studied here. Here we present the first absolute proper-motion measurement of the cluster measured with respect to a sample of galaxies, an important measurement considering that M4 is a very well studied cluster.

As discussed earlier, our coordinate differences were measured by centering on the cluster stars. We then found the centre of the extragalactic distribution and directly

measured the difference between this and the centre of the M4 clump. Converting Galactic coordinates to the equatorial system, we find $\mu_\alpha = -12.26$ mas/yr, $\mu_\delta = -18.95$ mas/yr, with a one-dimensional uncertainty of 0.48 mas/yr. The error in the mean for the absolute proper motion is the quadrature sum of the total errors for each of the galaxy and cluster star distributions. The final errors in our absolute proper motion are completely dominated by the dispersion in the galaxy sample. Comparing these results directly to previous studies, we find that our total proper motion ($\mu_{\text{total}} = \sqrt{(\mu_\alpha)^2 + (\mu_\delta)^2}$) is about 4% smaller than the Dinescu et al. (1999) value, about 13% larger than the Cudworth & Rees (1990) value and about 3% smaller than the Bedin et al. (2003) study.

For completeness, we can also convert our cluster proper motions into absolute space motions. The Solar motion is $(U_\odot, V_\odot, W_\odot) = (+10.0, +5.2, +7.2)$ km/s (Dehnen & Binney 1998), where $U_\odot$ is positive towards the Galactic centre, $V_\odot$ is in the direction of Galactic rotation, and $W_\odot$ is out of the plane. Therefore, for M4 we derive an absolute space motion of $(U, V, W)_0 = (57.0 \pm 5.6, -186.1 \pm 5.6, -2.4 \pm 3.5)$ km/s with respect to the LSR, for a distance of $d_{\text{M4}} = 1720$ pc and a cluster radial velocity of $v_\text{r} = 70.9 \pm 0.6$ km/s (Peterson, Rees & Cudworth 1995). The uncertainties calculated for the space motions above do not include any distance uncertainty.

2.4 The Proper-Motion and Colour-Magnitude Diagrams

In Figure 2.4 we again present the final proper-motion diagram and also the corresponding colour-magnitude diagram (CMD) for all objects within the M4 field. As we mentioned earlier, the tighter clump of dots in the proper-motion diagrams represent M4 (proper-motion dispersion, $\sigma_{\text{total}} = 1.95 \pm 0.06$ mas/yr) whereas the more diffuse clump represents the spheroid population plus other stars along the line of sight (proper-motion dispersion $\sigma_{\text{total}} = 3.71 \pm 0.16$ mas/yr). The uncertainties in the dispersions have been calculated as $\sigma/\sqrt{2N}$ (see e.g., Lupton 1993) in each direction and then added in quadrature for the total uncertainty. The dispersions in these cases actually measure a combination of each population's intrinsic velocity dispersion, as well as scatter produced from instrumental errors. The latter is clearly evident, as we get smaller dispersions for brighter magnitude cuts which eliminate the lowest signal-to-noise ratio objects (the above numbers however do reflect the dispersions measured from using the entire data set). The extragalactic objects in our data, which have not moved during the 6 year baseline, are also convolved within the field clump identified above. These are identified with red dots in the top-right panel.

The CMD (left panel) shows the remarkably tight M4 main-sequence extending down to at least $V \simeq 27$ on top of the foreground/background stars. A rich cluster white-dwarf
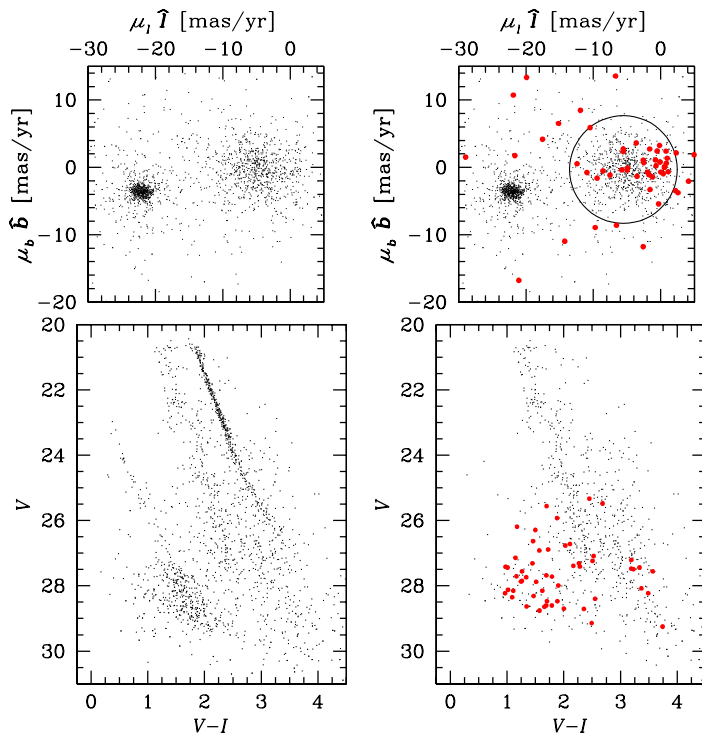
Figure 2.4: *Top* - The proper-motion diagram for all stars (μ_l, μ_b) is shown, with galaxies represented as red dots (see §2.3). The tighter clump represents M4 members and the more diffuse clump predominantly represents the background spheroid stars. *Bottom* - The CMD for all objects in the image is shown in the left panel and for only those objects which fall within the spheroid field clump in the right panel. The galaxies are again shown in red.

cooling sequence is also seen stretching from $23 \leq V \leq 29.5$. As mentioned earlier, the line of sight through M4 ($d_{\mathrm{M4}} = 1.7$ kpc) also intersects the spheroid of our Galaxy at a projected distance of 2.2 kpc above the Galactic nucleus (for a tangent point distance of 7.6 kpc). This population is more easily seen when the M4 main-sequence stars are removed by proper-motion selection (right panel). The field population clearly extends to $V \sim 30$ and shows some evidence for potential white dwarfs in the faint-blue region of the CMD. These can be confused with the galaxies in the V, $V-I$ plane, thereby illustrating the importance of stellarity measurements.

The main sequence of the field population in the range $V = 24$–30 is too broad to be consistent with the colour distribution expected from a population with no metallicity spread at the distance of the spheroid. However, we can rule out a contribution of stars

from the Galactic bulge in these data, given that the line of sight passing through M4 lies well outside the infrared bulge as imaged by *COBE* (Arendt et al. 1998). The field also misses the highest surface-brightness isophotes in Binney, Gerhard & Spergel (1997) and clearly avoids the classical metal-rich bulge population (McWilliam & Rich 1994; Frogel, Tiede & Kuchinski 1999). Similarly, the redder stars in the field cannot be stars in the tri-axial bar near the Galactic centre. The orientation of the bar is such that the near side of the semi-major axis ($\sim$ 2 kpc) lies in the first quadrant. The angle between the Sun-centre line and the bar's major axis in the plane of the disk is $\phi \simeq 20°$ (Gerhard 2002). The line of sight through M4 to the centre of the Galaxy, $(l, b) = (350.97°, 15.97°)$ also falls in this quadrant. Given the thickness of the bar and axis ratio 1.0:0.6:0.4 (Binney, Gerhard & Spergel 1997), an azimuthal angle of 20° would place the near side of the bar's major-axis only $\simeq$ 6.5 kpc from us (assuming an 8 kpc Galactocentric distance). However, with a latitude of $\simeq$ 16°, the line of sight through M4 is already 1.9 kpc above the plane at a distance of 6.5 kpc and therefore well above the thickness of the bar. Other bar models, such as those in Cole & Weinberg (2002), would also not intersect our line of sight.

A better explanation for the thickness of the main sequence is that a small admixture of metal-rich thick disk stars along the line of sight make up the redder population. This is expected in these data, given that the scale height of the thick disk is 1–1.5 kpc (Kuijken & Gilmore 1991; Bienaymé, Robin & Crézé 1987). This population would be co-rotating, perhaps with a small lag, and therefore reside closer to the location of the galaxies. However, the proper-motion diagram does not show any obvious evidence of this population even when isolating only the reddest, brightest possible thick disk stars. The exact interpretation of the thickness of the observed main sequence is therefore still somewhat unclear, and would be an interesting future study.

2.5 White Dwarfs

2.5.1 The Reduced Proper Motion Diagram

With galaxies clearly separated from stars in these data, finding spheroid/dark halo white dwarfs should be relatively easy, considering they must be faint, blue and have a proper motion consistent with the spheroid clump. Since we also may have contamination from the thin and thick disks along our line of sight, the best way to isolate the inner-halo white dwarfs is to select them from the reduced proper motion diagram (RPMD). This two dimensional plot (H_V vs $V-I$, where $H_V = V + 5\log(\mu_{\text{total}}) + 5$, and μ_{total} is measured in $''$/yr) removes the different distances of individual populations by using the size of the proper motion as an effective distance indicator to offset the apparent magnitude. Therefore, similar populations, despite their distance, will occupy similar regions on this

diagram based both on their stellar properties and kinematics. Figure 2.5 presents our stellar objects (stellarity > 0.7) for the large field clump (see Figure 2.4) on this plane, together with the M4 stars (red dots).
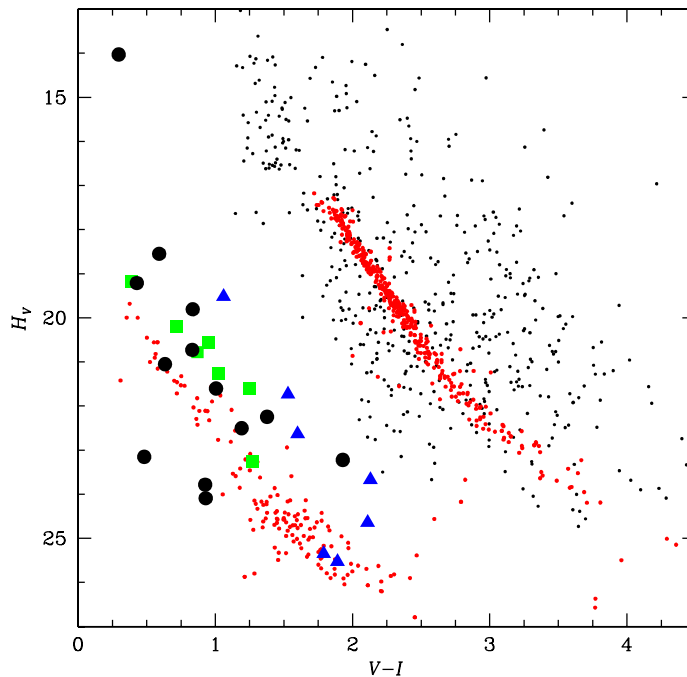
Figure 2.5: The reduced proper motion diagram ($H_V = V + 5\log(\mu''_{\text{total}}) + 5$) is shown for all field stars with stellarity > 0.7 and M4 members (red dots). Inner halo white dwarf candidates are displayed with larger circles. White dwarfs from the Mendez (2002) study (green squares) and the Nelson et al. (2002) study (blue triangles) are also displayed, after correcting for reddening and extinction differences.

The RPMD clearly shows that the majority of our spheroid main-sequence sample (small dark dots) is similar to that of M4 (red dots). This is expected, considering that the mean properties, such as the age and metallicity, are similar for both M4 and the spheroid. For a fixed magnitude, we see objects both above and below the M4 main-sequence stars on this plane. The M4 white-dwarf cooling sequence is seen towards the blue end of the diagram and represents a locus for potential halo white dwarfs. Several candidate white dwarfs from the field population (larger dark dots) are clearly seen sprinkled through the range $14 < H_V < 25$, near $V-I \sim 1$. Most of these objects are found above the M4

white dwarfs, suggesting they have smaller proper motions (disk objects). Three objects are found below the M4 white dwarf sequence, suggesting possible spheroid stars. Also shown are the locations of the thick-disk and putative dark halo-white dwarfs from the Mendez (2002) study (green squares) and those from the Nelson et al. (2002) study (blue triangles). The faintest Mendez object, as well as the faintest two Nelson objects, agree very well in location with the M4 white dwarfs on the RPMD (these are the claimed dark halo detections, see §2.6 for further discussion). The remaining Mendez and Nelson objects are found above the M4 stars, suggesting a possible thick disk origin. These points have all been corrected to match the reddening and extinction along this line of sight.

We also note that there is a good reason for not selecting white dwarfs based on their location in the colour-magnitude diagram. One would naively expect that the spheroid white dwarfs should be consistent with the location of the M4 white dwarf cooling sequence shifted down to the tangent point (3.2 magnitudes fainter). This point is the intersection of our line of sight with the shortest line of sight that is radially directed from the Galactic center. However we need to consider that the spheroid white dwarfs will occupy some depth in distance around the tangent point so there will be both closer and farther objects. Since the luminosity function (Hansen et al. 2002) of white dwarfs at the tangent point rises sharply at a point fainter than our limiting magnitude, we can expect to be systematically biased to seeing some fraction of the fainter white dwarfs within the region of the rising luminosity function slope if they reside closer to us than the tangent point. Since these fainter white dwarfs are redder than their brighter counterparts, the locus of these points will shift the +3.2-magnitude fiducial up to brighter magnitudes, on a parallel slope to the white dwarf cooling sequence. Therefore, we cannot use a colour cut on the CMD to select these objects. The approach used below does not suffer from these effects.

2.5.2 Simulations

In order to assign our candidate white dwarfs to particular Galactic components, we need to model the underlying white dwarf populations. These simulations were produced by Dr. Brad Hansen. We model four such components: the thin disk (a double exponential with radial scale length 3 kpc and vertical scale height 0.3 kpc); the thick disk (a double exponential with radial scale length 3 kpc and vertical scale height 1 kpc); the spheroid/stellar halo (a power law with $\rho \propto r^{-3.5}$, where r is the spherical Galactocentric radius); and a putative 'dark halo' (a power law with $\rho \propto r^{-2}$). The Solar-neighbourhood (white dwarf only) normalizations for the various components are taken to be $3.4 \times 10^{-3} M_\odot/\mathrm{pc}^3$ (Holberg, Oswalt & Sion 2002) for the thin disk, $10^{-4} M_\odot/\mathrm{pc}^3$ for the thick disk (Oppenheimer et al. 2001; Reid, Sahu & Hawley 2001), $3 \times 10^{-5} M_\odot/\mathrm{pc}^3$ for the spheroid (Gould, Flynn & Bahcall 1995) and $1.4 \times 10^{-3} M_\odot/\mathrm{pc}^3$ for the dark halo (corresponding to a fraction

20% of the dark matter density, as indicated by the MACHO group's results, Alcock et al. 2000).

The above density laws are projected onto the line of sight, taking into account the increasing volume at larger distance (for fixed solid angle). Using the same white dwarf models as in Hansen et al. (2002), we derive Monte-Carlo realizations of the field white dwarf populations distributed along our line of sight. The thin, thick and spheroid populations are drawn from a distribution with progenitor IMF $dN/dM \propto M^{-2.6}$. The dark halo population is drawn instead from a population with a Chabrier IMF (Chabrier 1999; IMF2 in the notation of that paper). The models of Hurley, Pols & Tout (2000) were used to provide main-sequence lifetimes. The thin-disk population was assumed to be forming stars at a continuous rate (over the past 10 Gyr), while all the others were assumed to be 12 Gyr old bursts. The Monte-Carlo calculations include the detection probability using the incompleteness corrections from Richer et al. (2002) and Hansen et al. (2002).

The final results indicate that, on average, we expect 7.9 thin-disk, 6.3 thick-disk and 2.2 spheroid white dwarfs. The dark halo will contribute 2.5 white dwarfs if 20% of the dark halo is made up of DA white dwarfs. The first three (i.e., the standard) populations are dominated by bright white dwarfs located near the tangent point (even for the disk populations, as the radial exponential largely compensates for the decrease due to the vertical exponential, at least for this line of sight). The dark-halo population, on the other hand, is dominated by objects at distances $\sim$ 2–3 kpc, a consequence of the bias inherent in the Chabrier IMF towards higher progenitor masses and thus shorter main-sequence lifetimes (corresponding to longer white dwarf incarnations). This results in an anticipated systematic colour difference between any dark-halo white dwarfs (relatively red) and those from standard populations (relatively blue). We stress this applies particularly to our data set and does not necessarily extend to wider-field surveys.

2.5.3 Results

In Figure 2.6, we display the location of the white dwarfs in the RPMD. We also overlay the positions of the simulated sample of white dwarfs (open circles) on this diagram (for a much larger area than that observed). The thin-disk (top-left) and thick-disk (top-right) stars are generally found brighter than the spheroid (bottom-left) stars, with a limit at $H_V \sim 25$ beyond which there are very few disk white dwarfs. A similar threshold was used by Flynn et al. (2001) to separate disk and halo white dwarfs. They found that most dark halo white dwarfs would lie at $24.3 \leq H_V \leq 26.3$ and peak at $H_V \simeq 25.3$ (corrected to the extinction along this line of sight). The *relative* numbers of simulated thin-disk, thick-disk and spheroid objects plotted in Figure 2.6 have been scaled to match the expectations in our data. The $H_V \sim 14$ cutoff at the top of the diagram indicates the saturation

limit of our data. The simulated dark-halo white dwarfs (open circles, bottom-right) are clearly distinct from these conventional populations and are found at redder colours (for an explanation see §2.5.2). Also included on this panel are those objects which did not satisfy the stellarity or proper motion cut (small crosses) to show that the data do extend fainter than $H_V = 25$ and well into the dark halo regime.

Although it is difficult to separate thin-/thick-disk white dwarfs, we can conclude that nine of our objects are consistent with disk white dwarfs ($H_V \leq 23$, $V-I \leq 1.5$). Three objects in our data (having $H_V = 23.15$, $V-I = 0.48$, $H_V = 23.78$, $V-I = 0.93$, and $H_V = 24.09$, $V-I = 0.93$) which are fainter than this cut are found within the tail of the thick disk simulated sample. These objects are, however, in excellent agreement with the simulated spheroid white dwarfs (bottom-left). These are the same three objects which fall below the M4 white dwarfs in Figure 2.5. Although the predicted number of stars allows for incompleteness in the data set, we must still correct these observed numbers of stars for the incompleteness caused by mismatches in the SEXTRACTOR versus ALLSTAR classifications. In §2.3.1 we estimated that 25% of the ALLSTAR sources were missed for these magnitude bins. Our final corrected numbers of detected objects are therefore 12 disk white dwarfs (14 expected) and 4 spheroid white dwarfs (2 expected) and therefore in good agreement with the simulations, considering that the observed spheroid number is an upper limit (i.e., two of the objects are consistent with the tail of the thick disk distribution).

A key result from Figure 2.6 is that the simulated dark halo region is basically not populated with data points. Only one object which we classified as thick disk (with $H_V = 22.25$, $V-I = 1.38$) marginally agrees with the edge of the simulated sample. Less than 4% of our simulated dark-halo sample is found with a reduced proper motion below that of this object, suggesting <0.1 expected real objects. Also, the colour of this star falls close to the blue edge of the simulated sample and is only marginally consistent with the expected location of dark-halo white dwarfs. A possible explanation for the other extremely red object, as well as possibly this object, is that these may be binary thin-/thick-disk white dwarfs with red main-sequence companions. We can also rule out the spheroid candidate objects as potential dark-halo white dwarfs given that they have much bluer colours. Finally, on Figure 2.6 we also indicate the limit at $H_V \sim 27$ above which we would have expected dark-halo white dwarfs, given our simulations and detection efficiency. Table 2.2 presents our final white dwarf candidate list, both for the disk and spheroid.
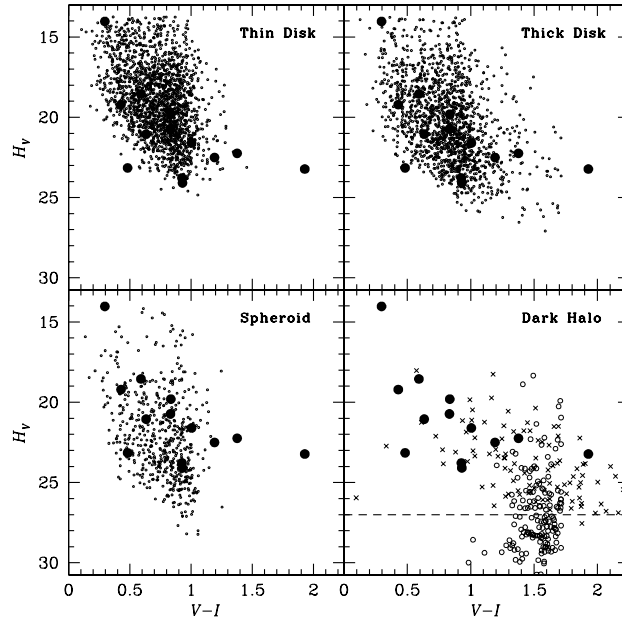
Figure 2.6: A simulated sample of white dwarfs belonging to the thin disk (top-left), thick disk (top-right), spheroid (bottom-left) and dark halo (bottom-right) are shown on the RPMD as open circles in all panels. Candidate white dwarfs from the present data are shown as large filled circles. After correcting for mismatches in the SEXTRACTOR versus ALLSTAR photometry, we find 12 (9 originally) probable thin/thick disk white dwarfs, 4 (3 originally) probable spheroid white dwarfs, and 1 outlier. Although 2.5 objects are expected from a 20% dark halo dominated by DA white dwarfs, we find none in these data (see §2.5.3). Small crosses depict those objects which did not satisfy the stellarity or proper motion cut and show that the data set is sensistive to $H_V <$ 27 and therefore to dark halo white dwarfs (dashed line).

Candidate	Designation	α_{J2000}	δ_{J2000}	V	$V-I$	μ (mas/yr)[1]	μ_l (mas/yr)	μ_b (mas/yr)
WD 1	disk	16:23:52.76	−26:33:13.07	24.60	0.30	0.77	+0.77	−0.05
WD 2	disk	16:23:54.49	−26:31:19.38	27.17	0.43	2.56	+2.33	+1.06
WD 3	disk	16:23:55.54	−26:32:36.64	24.18	0.59	7.47	−7.27	−1.71
WD 4	disk	16:23:55.87	−26:33:03.28	27.43	0.63	5.31	−5.22	+0.96
WD 5	disk	16:23:58.75	−26:32:40.13	25.22	0.84	8.28	−8.26	+0.51
WD 6	disk	16:24:02.33	−26:32:25.55	27.98	0.83	3.54	+0.88	+3.43
WD 7	disk	16:24:02.81	−26:32:42.61	27.82	1.01	5.70	−5.37	−1.91
WD 8	disk	16:24:03.10	−26:32:45.10	27.99	1.19	7.99	−7.41	−3.01
WD 9	spheroid	16:23:55.28	−26:32:47.47	27.02	0.48	16.85	−15.48	+6.66
WD 10	spheroid	16:23:55.87	−26:32:37.77	28.34	0.93	14.15	−13.69	+3.57
WD 11	spheroid	16:23:58.12	−26:32:10.13	27.82	0.93	15.58	−15.31	+2.89
WD 12	disk?	16:23:53.25	−26:33:10.66	28.25	1.38	6.30	−4.73	−4.17
WD 13	disk?	16:23:59.35	−26:31:28.52	27.49	1.93	13.99	−13.89	−1.67

Table 2.2: Disk and spheroid white dwarfs 1. $\mu_{\text{total}} = \sqrt{(\mu_l)^2 + (\mu_b)^2}$

2.6 Discussion

Contrary to our result, recent claims by Oppenheimer et al. (2001), Koopmans & Blandford (2001), Nelson et al. (2002) and Mendez (2002) suggest that a halo white-dwarf population exists and that the number of white dwarfs is in excess of that expected from the stellar spheroid alone. Others (Reid, Sahu & Hawley 2001; Hansen 2001; Richer 2001) have argued that this small population is a component of the thick disk. Gibson & Mould (1997) used simple chemical evolutionary arguments to show that it is difficult to reconcile the observed spheroid main-sequence chemical abundance with that expected from an IMF which would give the speculated halo white-dwarf density. We briefly summarize these independent studies and place them in the context of the present observations.

Oppenheimer et al. (2001) sampled 4165 deg^2 towards the Southern Galactic Cap and found 38 cool white dwarfs, the majority of which they assign to a dark-halo population. The data from this study were made available and consequently several authors have re-analyzed the result. Koopmans & Blandford (2001) used a dynamical model and performed a maximum-likelihood analysis on the Oppenheimer sample of white dwarfs and found two kinematically distinct populations (a thick disk and a flattened halo) at a greater than 99% confidence limit. However, Reid, Sahu & Hawley (2001) compared the kinematics of the Oppenheimer sample to the local M-dwarf sample and suggested that the majority of this population resides in the thick disk. Richer (2001) and Hansen (2001) examined the temperature and age distributions of the Oppenheimer white dwarf sample and found that the star-formation history for most of these stars is more representative of the disk rather than the halo.

The Nelson et al. (2002) study looked for high proper motion objects in the Groth-Westphal strip. They measured proper motions over a 7-year baseline using WFPC2 observations of a 74.8 arcmin^2 region. Of the 24 high proper motion objects detected, five are believed to be strong white dwarf candidates (two of these are possibly dark halo, three are disk) and a further two are classified as marginal candidates. The two halo objects are the faintest two blue triangles in Figure 2.5 and the three disk objects are the brightest three blue triangles in Figure 2.5. By creating a model of the stellar components of our Galaxy, Nelson et al. (2002) demonstrate that the observations are clearly in excess of the expected number of white dwarfs from the Galactic stellar components. Although systematic errors due to uncertainties in the model parameters are large, the observations suggest a 7% white dwarf dark halo.

Most recently, Mendez (2002) has presented new evidence for a bi-modal kinematic population of old white dwarfs and suggests that most of the required dark matter in the Solar vicinity can be accounted for by these populations. This analysis is based on

a proper-motion membership study of the Galactic globular cluster NGC 6397 (King et al. 1998). Mendez (2002) used both the reduced proper motion and the colours of field objects to assign six white-dwarf candidates to the thick disk and one to the dark halo (the faintest green square shown in Figure 2.5). The Mendez (2002) study gives no information on the morphology of the sources and possible extragalactic contamination.

There is clearly no convincing answer yet as to whether white dwarfs make up an important component of the dark matter in our Galaxy. The controversy spurred from these studies can only be resolved by obtaining deeper, larger images of halo fields which could contain many white dwarfs. The current data set represents an important constraint in the context of searching for these objects as it is sensitive to white dwarfs from all three (disk, spheroid and dark-halo) components and it is only the dark-halo ones that are not found. Furthermore, our images represent the deepest-ever probe into the inner halo of our Galaxy and we do see the stellar halo (spheroid) main-sequence progenitors of the white dwarfs. By using only directly observable quantities, such as the proper motions, magnitudes and colours we have demonstrated that these data do not support a white-dwarf component to the dark halo.

2.7   Summary of White Dwarfs in the Field

A 6-year baseline of imaging of the globular star cluster M4 has allowed us to separate out the cluster stars from the background spheroid population. Over this timescale, distant extragalactic sources have not moved and are identified using image morphology criteria. We establish a zero-motion frame of reference using these galaxies and search for halo white dwarfs based on their morphology and kinematics. We find that distinguishing faint galaxies from field stars is impossible when based solely on proper motions, and that an index of stellarity is crucial in separating the two classes. Based on the reduced proper motion diagram, we identify nine thin/thick disk and three spheroid white dwarfs in these data. These numbers are consistent with the expected contribution of the conventional populations along the line of sight. Additionally, 2.5 dark halo white dwarfs are expected in these data based on a 20% white dwarf dark halo and are not found. The Poisson probability of getting zero events when 2.5 are expected is about 8%, and therefore our conclusion of not needing a dark halo population of white dwarfs to explain the present data is marginal. A similar study with the Advanced Camera for Surveys (ACS) on *HST* would be sensitive to many more potential dark halo white dwarfs and is desirable given the importance of this problem.

The extragalactic reference frame also allows us to perform two other important measurements. First, this fixed frame gives us an independent measurement of the fundamental

Galactic constant, $\Omega_0 = \Theta_0/R_0 = 25.3 \pm 2.4$ km/s/kpc. This provides a velocity of the Local Standard of Rest $v_{\mathrm{LSR}} = \Theta_0 = 203 \pm 23$ km/s at $R_0 = 8.0 \pm 0.5$ kpc, in agreement with independent studies. Secondly, the galaxies give us a direct measurement of M4's absolute proper motion, $\mu_\alpha = -12.26 \pm 0.47$ mas/yr, $\mu_\delta = -18.95 \pm 0.48$ mas/yr, also in good agreement with the latest studies.

Chapter 3

White Dwarfs in Star Clusters

3.1 Introduction

For many reasons star clusters represent excellent environments in which we can explore the properties of white dwarf stars. The assumed single-burst star formation event that creates a star cluster produces stars with a spectrum of masses yet similar metallicity, age and (most importantly) distance. Since the evolution of stars is driven primarily by their initial mass, examining different populations of stars in a cluster can give us a snapshot of the life stages of a single star: turn-off, red giant, planetary nebula, white dwarf, etc. (see Renzini & Fusi-Pecci 1988). By applying a statistical argument to objects in different locations of a cluster colour-magnitude diagram, we can infer information about the properties of objects in different stellar evolutionary stages, such as white dwarfs. Studying white dwarfs in practice, however, is not this simple. The richest star clusters, the globular clusters, contain large numbers of white dwarfs but these clusters are also very old. Therefore the limiting magnitude of the coolest white dwarfs in these clusters occurs at magnitudes that are too faint for ground based observations. For example, the limiting white dwarf magnitude for a 12 Gyr cluster occurs at $M_V \simeq 17.5$ (Richer et al. 2000). Recently, a large *HST* imaging study of globular cluster M4 has successfully measured the age of the cluster (Hansen et al. 2004) by using new white dwarf cooling models that predict different behaviour in the emergent spectra of very cool white dwarfs (Hansen 1999; Saumon & Jacobson 1999).

An alternative method of studying white dwarfs is to utilize the much younger and more metal-rich open star clusters. However, there are four major difficulties in using open star clusters to study white dwarfs: (1) the majority of these clusters are not old enough to have produced a sizeable white dwarf population; (2) most are not rich enough to contain many white dwarfs; (3) these clusters lie in the plane of the Galaxy, so that foreground and background contamination is high; and (4) the photometric depth of most studies has not been great enough to clearly see white dwarfs. The first two factors result in very

---

[2]A version of this chapter has been published. Kalirai, J.S., Fahlman, G.G., Richer, H.B., and Ventura, P. (2003) The CFHT Open Star Cluster Survey. IV. Two Rich, Young Open Star Clusters: NGC 2168 (M35) and NGC 2323 (M50). Astronomical Journal, 126: 1402-1414.

few white dwarfs, often quite scattered somewhere in the faint, blue end of the colour-magnitude diagram, and the third results in a large amount of contamination from both field stars and background star-forming galaxies, which also appear as faint, blue objects. The fourth factor has always been a deterrent to the serious study of cluster white dwarfs. White dwarf cooling models and theoretical atmospheres (Wood 1995; Bergeron, Saumon, & Wesemael 1995), indicate that a significant number of white dwarfs are not expected brighter than an absolute magnitude of $M_V \sim 10$. At the opposite end, it is known that very old, cool white dwarfs may reach $M_V \geq 17.5$. Even the bright end of the white dwarf cooling sequence is often too faint for the limiting magnitude that could possibly be reached by many telescopes, even for moderately close clusters. The new large field detectors and imagers on 4-m class telescopes are ideal instruments to study these faint magnitudes in open star clusters. This was demonstrated in the white dwarf analysis of M67 (Richer et al. 1998).

What we require to address the properties of white dwarf stars are very rich, yet intermediate aged open star clusters with little reddening. The clusters must be old enough so that a significant number of white dwarfs have formed, yet young enough so that the end of the white dwarf cooling sequence does not occur at an unobservable magnitude. To find these objects, we began the *CFHT* Open Star Cluster Survey in late 1999. We selected 19 open star clusters in the Northern Hemisphere and obtained deep, wide-field photometry of each one in the B and V filters. The reduction of the data set and analysis of first results in both NGC 6819 and NGC 2099, two very rich clusters, comprised the author's Master's thesis. Both of these clusters (see Kalirai et al. 2001c; Kalirai et al. 2001b) satisfy the criteria for finding white dwarfs discussed above. We now continue this work and turn to two much younger clusters, NGC 2168 and NGC 2323. As we will see later, the turnoff masses of these clusters are quite large, $M \sim 5\ M_\odot$, and therefore if we can find any white dwarfs in the clusters, we know that they came from massive progenitors. These are therefore uniquely important for setting constraints on the high mass end of the initial-final mass relationship (see Chapter 4).

In the next section, we present the observations of NGC 2168 and NGC 2323 and discuss the data reduction. We then present the cluster colour-magnitude diagrams in §3.3 and determine the cluster reddening, distance and metallicity §3.3.1. In §3.4 we fit theoretical isochrones to determine the cluster ages. These results are key in determining main-sequence lifetimes of white dwarf progenitors later. We digress to discuss cluster dynamics and study the mass functions of each of these clusters in §3.5. Finally, we search for white dwarfs in these two young clusters in §3.6 and discuss candidate importance and implications. This particular study is summarized in §3.7.

3.2 Observations and Data Reduction

As with other clusters in the *CFHT* Open Star Cluster Survey, the data were obtained during a three night observing run in 1999 October. All observations were obtained at the Canada-France-Hawaii Telescope through standard *V* and *B* filters with the CFH12K mosaic camera, which has a $42' \times 28'$ field-of-view (Cuillandre et al. 2000). NGC 2168 was imaged during night 3 of the run, and NGC 2323 during night 1 (short exposures to obtain the photometry of giants were acquired at a later date). For NGC 2168, two 5-minute exposures were obtained in each colour, however, only one was usable. This was combined with individual 50, 10 and 1 second exposures to complete the photometry. For NGC 2323, the photometry from single exposures of 300, 50, 10 and 1 seconds in each colour were combined to produce a catalogue of magnitudes and colours. The seeing conditions during the observations of NGC 2168 was $1.15''$ and the air-mass was 1.60. For NGC 2323, the seeing was $0.85''$ and the air-mass was 1.18.

The data were processed (flat-field, bias and dark corrected) and combined using the FITS Large Images Processing Software (FLIPS) (J.-C. Cuillandre 2001, private communication) as described in §3 of Kalirai et al. (2001a). Over 53 flats and 13 bias frames were observed during the run.

We reduced the data using a preliminary version of the TERAPIX photometry routine PSFex (Point Spread Function Extractor) (E. Bertin 2000, private communication). We used a separate, variable PSF for each CCD in the mosaic. Some features of PSFex are described in §4 of Kalirai et al. (2001a).

Calibration was addressed by separately observing Landolt standard fields SA-92 and SA-95 (Landolt 1992) during the observing run. A total of 92 calibration stars (different configurations of exposure times, filters and airmasses) were used to calibrate the NGC 2168 data. For NGC 2323, 130 calibration stars were used (see Tables 2 and 3 in Kalirai et al. 2001a). Comparison of the aperture photometry of these stars with the PSFex photometry yielded the transformation equations required to calibrate the data (see §§5.1 and 5.2 of Kalirai et al. 2001a). The uncertainty in the zero points used for the calibration is estimated to be ~ 0.018 in *V* and ~ 0.017 in *B*. The air-mass coefficients are 0.087 ± 0.02 in *V* and 0.160 ± 0.006 in *B*, in good agreement with *CFHT* estimations of 0.10 and 0.17 respectively. The colour terms were averaged over the three night observing run and are in agreement with the nominal *CFHT* estimates in the *V* filter and are slightly lower for the *B* filter.

3.3 The NGC 2168 and NGC 2323 Colour-Magnitude Diagrams

Figures 3.1 and 3.2 present photometric colour-magnitude diagrams (CMDs) for both NGC 2168 and NGC 2323. The panels on the left show all objects measured with PSFex, whereas the panels on the right depict only those objects with a stellarity index ≥ 0.50. This SEXTRACTOR image morphology parameter (Bertin & Arnouts 1996) uses a robust procedure to estimate source resolution and we have shown in the past (Kalirai et al. 2001b; Kalirai et al. 2001c) that this cut is effective in removing faint-blue galaxies and other image defects. Clearly, the fainter parts of the CMDs in the right panels are much cleaner than the left panels. Some potential white dwarf candidates are also brought out at the faint blue end of the CMDs.
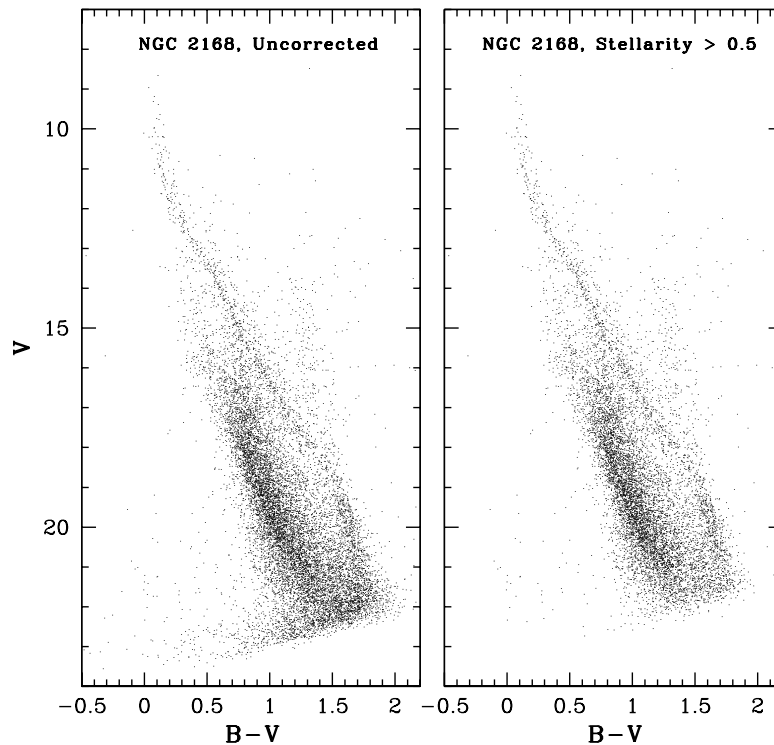
Figure 3.1: The CMD for NGC 2168 clearly shows a well populated main sequence stretching from $V \simeq 9$ to $V \simeq 22.5$. After eliminating faint, blue galaxies and other image defects with a 0.50 stellarity cut (right panel), some potential white dwarfs are seen at $V \simeq 21.5$, $B-V \simeq 0$.
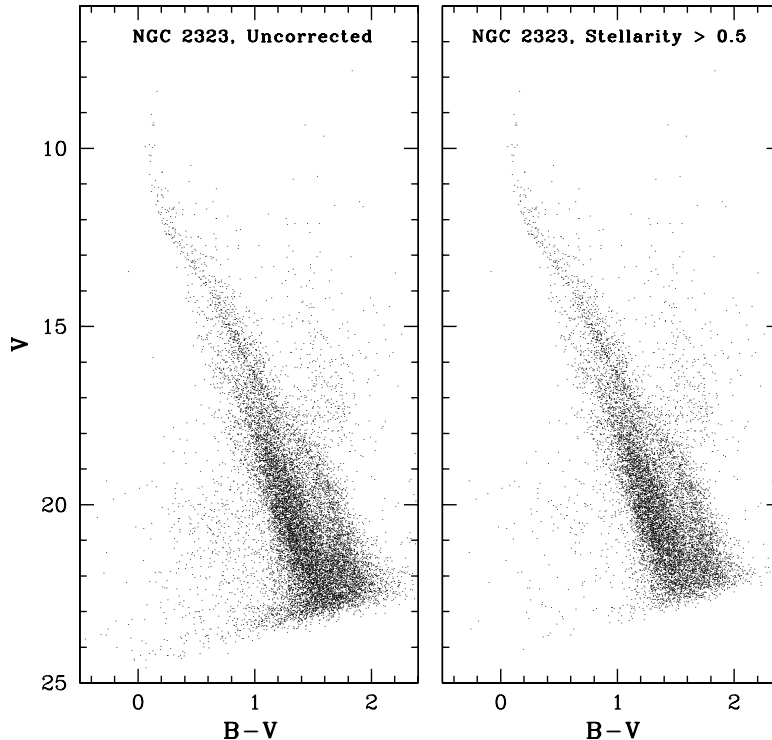
Figure 3.2: The CMD for NGC 2323 clearly shows a well populated main sequence stretch-
ing from $V \simeq 8$ to $V \simeq 23$. After eliminating faint, blue galaxies and other
image defects with a 0.50 stellarity cut (right panel), some potential white
dwarfs are seen scattered in the faint-blue corner of the CMD.

The CMD for NGC 2168 (Figure 3.1) shows a rich main sequence extending from $V \simeq$ 8.5 to $V \simeq 22.5$. One potential cluster red giant is also seen at $V \simeq 8.48$, $B-V \simeq 1.32$ and can be used to constrain the age of the cluster through fitting of the blue loop. The post main-sequence stellar evolution phase involves core Helium burning and the luminosity of this phase is a good age indicator. The morphology of the turn-off can also be used to determine the age, however this is quite difficult in younger clusters which have less pronounced turn-offs. The main sequence presented here is tighter than any of the previous studies on this cluster. This photometry is deep enough to detect the faintest white dwarfs in the cluster. These are believed to have originated from quite massive progenitors. The 'clump' of objects near $V \simeq 21.5$, $B-V \simeq 0$ most likely represents the end of the white dwarf cooling sequence in this young cluster. This will be further investigated in §3.6. The wall of stars bluer (or fainter) than the cluster main sequence is the background disk

star population. With a Galactic latitude of only $\sim 2°$, NGC 2168 resides very close to the plane of the Milky Way. Within our $40'$ diameter for the cluster field (one direction is cut off at $28'$ by the CFH12K mosaic) we have detected many field stars which overlap with cluster members on the faint main sequence. The vertical feature in the CMD to the red of the cluster main sequence (at $14 \leq V \leq 17.5$, $B-V \simeq 1.3$) may represent distant giant stars or even main-sequence red dwarfs in the disk. This is smeared out in V due to a distance spread along the line of sight. The defined field does not encompass the entire radial extent of NGC 2168.

For NGC 2323, the CMD (Figure 3.2) again shows a rich, long main sequence extending from the tip of the turnoff at $V \simeq 8$ down to $V \simeq 23$ at the limit of our data. As mentioned in §3.1, the previous best study of this cluster, the photo-electric work of Claria, Piatti & Lapasset (1998), only detected 109 cluster members brighter than $V \sim$ 14. The SEXTRACTOR cleaned CMD (right panel) again shows several potential white dwarfs scattered in the faint, blue region of the diagram. Before we can study these objects, we must first determine parameters for each cluster which will allow us to convert theoretical models for the white dwarfs on to the observational plane.

3.3.1 Cluster Reddening, Distance and Metallicity

As summarised in Table 3.1, several previous measurements of both the reddening and distance of each of NGC 2168 and NGC 2323 are available in the literature. We adopt reddening values from these studies, and re-compute the distances by comparing the cluster main sequences to the Hyades fiducial (de Bruijne, Hoogerwerf & de Zeeuw 2001). Since there is minimal scatter in the main sequences for these clusters, there is almost no ambiguity in the distance determination. For NGC 2168, we adopt $E(B-V) = 0.20$ from the recent 5-colour ($UBVRI$) photometry of Sarrazine et al. (2000). The metallicity of NGC 2168 is known due to the high resolution spectroscopic effort of Barrado y Navascues, Deliyannis & Stauffer (2001) who find [Fe/H] $= -0.21 \pm 0.10$ ($Z \simeq 0.01$). Other previous CCD studies, (e.g., Sung & Bessell 1999) have also found sub-solar metallicities for NGC 2168 using less robust techniques. To compare the Hyades sequence to NGC 2168, we first shift our CMD by $+0.09$ magnitudes in $B-V$ to account for the $\Delta Z \simeq$ 0.014 metallicity difference (the Hyades is given as $Z = 0.024$). The corresponding best fit distance modulus is found to be $(m-M)_0 = 9.80 \pm 0.16$, which gives $d = 912^{+70}_{-65}$ pc. The extinction has been corrected by using $A_V = 3.1E(B-V)$. This distance estimate is slightly greater than previous values for NGC 2168 (see Table 3.1), however, it is more precise because of the quality of the CMD.

For NGC 2323, we adopt a reddening value of $E(B-V) = 0.22$, which is an average of the recent Claria, Piatti & Lapasset (1998) study and the robust effort of Hoag et

al. (1961). Although no detailed spectroscopic abundance analysis is published for NGC 2323, photometric investigations (e.g., Claria, Piatti & Lapasset 1998) have found that solar metallicity models best reproduce the observed cluster main sequence. We shift the CMD by $+0.03$ magnitudes in $B-V$ to account for the $\Delta Z \simeq 0.004$ metallicity difference and find that the best fit distance modulus for NGC 2323 is $(m-M)_0 = 10.00 \pm 0.17$, which gives $d = 1000^{+81}_{-75}$ pc. As Table 3.1 shows, this distance is in good agreement with the most recent studies of NGC 2323

The uncertainties in the distances for these clusters are computed using an identical method to that used for NGC 2099 in Kalirai et al. (2001c). Briefly, the final uncertainty in the true distance modulus combines four individual uncertainties, and accounts for correlations between them. These are: (1) a scale factor translation from the $B-V$ axis to the V axis to account for the reddening uncertainty; (2) an estimated main-sequence fitting uncertainty at a fixed reddening value; (3) the error in the extinction, $\Delta_{A_V} = 3.1\Delta_{E(B-V)}$; and (4) the colour uncertainty due to an estimated metallicity uncertainty, Δ_Z. Kalirai et al. (2001c) describe the details of how these terms were combined.

More recently, Kalirai & Tosi (2004) have used synthetic colour-magnitude diagrams to model the populations of 4 rich open star clusters, including NGC 2168 and NGC 2323. By comparing the distribution of stars on the CMD with numerical simulations, they have obtained best fit reddening, ages and metallicity consistent with the values presented above.

Year	Redd. $E(B-V)$	Distance (pc)	Age (Myrs)	Data Type	Reference
NGC 2168					
1930		840		Photographic	Trumpler (1930)
1938		740		Photographic	Cuffey (1938)
1961	0.23	870			Johnson et al. (1961)
1961	0.23	871		Photoelectric/Photographic	Hoag et al. (1961)
1971	0.23	870	70–100	Photographic	Becker & Fenkart (1971)
1973	0.17	871	20–40	Photographic	Vidal (1973)
1992	0.26–0.44	725	85	Photoelectric	Sung & Lee (1992)
1999	0.255	832	200	CCD	Sung & Bessell (1999)
2000	0.3	731	100	CCD	von Hippel et al. (2000)
2000	0.198	809	160	CCD	Sarrazine et al. (2000)
2001		832	175	CCD	Barrado y Navascues et al. (2001)
2002	0.20	805	150	CCD	Deliyannis et al. (2002)
2003		912	180	CCD	This work
NGC 2323					
1930		780–860		Photographic	Trumpler (1930)
1930		500–800		Photographic	Shapley (1930)
1931		675		Photographic	Collinder (1931)
1935		520		Photographic	Rieke (1935)
1941	0.30	1210		Photographic	Cuffey (1941)
1961	0.20–0.26	1170		Photoelectric	Hoag et al. (1961)
1969			60	Photographic	Barbaro et al. (1969)
1983	0.33	995	140	Photographic	Mostafa (1983)
1998	0.25	931	100	Photoelectric	Claria et al. (1998)
2003		1000	130	CCD	This work

Table 3.1: Summary of published cluster parameters for NGC 2168 and NGC 2323

3.4 Theoretical Comparisons

As we will see in the next chapter, our primary goal after finding white dwarfs in young star clusters is to constrain the high mass end of the initial final mass relationship. In order to do this, however, we need to accurately measure cluster ages. The age measurement is an important input into determining progenitor lifetimes for any white dwarfs. We therefore now present a comparison of theoretical models to the observed cluster main-sequences to determine ages.

As with earlier clusters in the Survey, we are using a new set of theoretical isochrones to compare the observations to theory. This set of models was computed especially for the *CFHT* Open Star Cluster Survey by the group at the Rome Observatory (P. Ventura & F. D'Antona). Section 5.2 of Kalirai et al. (2001b) and section 3.4 of Kalirai et al. (2001c) provide a description of the models. Here we present only a brief summary and refer the readers to the earlier work for more insight. A description of the stellar evolution code that was used to build the tracks is given in Ventura et al. (1998). Convective core-overshooting is treated by means of an exponential decay of turbulent velocity out of the formal convective borders, and the convective flux has been evaluated according to the Full Spectrum of Turbulence (FST) theory prescriptions (Canuto & Mazzitelli 1992). The Bessell et al. (1998) conversions are used to convert luminosities to magnitudes, and temperatures to colours. The lower main sequence ($M < 0.7\ M_\odot$) has been calculated by adopting NextGen atmosphere models (Hauschildt, Allard & Baron 1999).

Figure 3.3 shows two panels with the best fit isochrones for NGC 2168. For the core-overshooting model shown in the left panel, we find an age of 180 Myrs. This is essentially identical to the 175 Myrs value found by Barrado y Navascues et al. (2001) and very close to the 150 Myrs value found by von Hippel et al. (2002). There is a possible red giant star at $M_V = -1.94$, $(B-V)_0 = 1.21$ which helps constrain the location of the blue loop. This star (as well as a turn-off star located at $M_V = -1.76$, $(B-V)_0 = -0.09$) falls directly under the line which is used to draw the isochrone on the figure, and therefore is difficult to see. We have increased the point size of all stars with $M_V \leq 0$ to help visualize the data. A non-core-overshooting model is also shown on the right and this gives an age of 130 Myrs. The ζ value in the figures represents the free parameter that specifies the e-folding distance of the exponential decay of turbulent velocities (Ventura et al. 1998). The value of 0.03 for this parameter is roughly consistent with the canonical 0.2 $H_{\rm p}$ (pressure scale height) assuming instantaneous mixing.

The 180 Myr isochrone reproduces the general shape of the main sequence very nicely. Near the turn-off, the model correctly falls on the blue-edge of the observed sequence, which is free of binary-contamination. Models of ages 160–200 Myrs in the overshooting
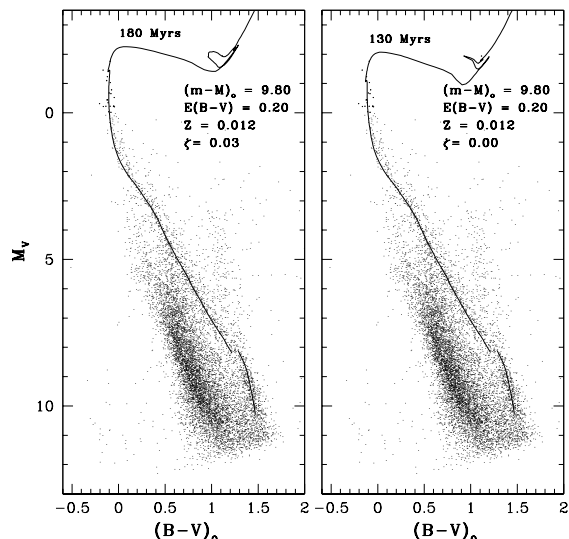
Figure 3.3: The left panel shows the best fit isochrones for NGC 2168 (age = 180 Myrs), based on a core-overshooting model. An equivalent fit is obtained by using a non-core-overshooting model of 130 Myrs (right panel). The discontinuity at $M_V = 8.2$ represents the limit to which we presently have non-grey atmosphere models for this metallicity ($Z = 0.012$). Fainter than this magnitude, we plot our solar metallicity isochrones. The metallicity difference causes a small shift between the colours of the two models, however, this does not spoil the excellent agreement on the lower main sequence between this model and the data. See §3.4 for a discussion of these results. Note that dots representing stars with $M_V \leq 0$ have been made slightly larger and bolder for comparison purposes.

case also provide acceptable matches to the observed cluster sequence. For the lower main sequence ($M_V > 8$), it was not possible to compute non-grey atmospheres for this metallicity. We therefore overplot the lower main sequence from a solar metallicity ($Z = 0.02$) model. A small colour shift (of approximately $\Delta(B-V) = 0.06$) is needed to correct for the metallicity of the cluster. Such a shift would move the lower main sequence blueward, but not by an amount which would produce a poor fit.

Figure 3.4 shows isochrone comparisons for NGC 2323. The age, using a core-overshooting model is found to be 120-140 Myrs (left panel). The solar metallicity isochrone fits the observed main sequence and turn-off well. As in the case of the similar metallicity clusters NGC 6819 and NGC 2099, the lower main sequence in this model again falls slightly bluer

than the data. This result is, however, a great improvement over previous grey atmosphere isochrones.
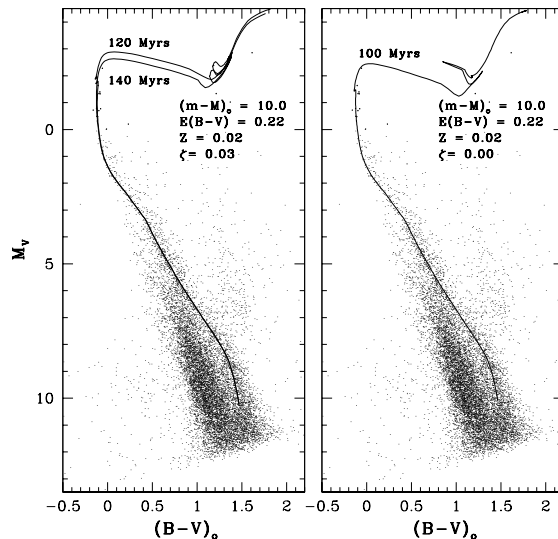
Figure 3.4: The left panel shows the best fit isochrones for NGC 2323 (age $\simeq$ 130 Myrs), based on a core-overshooting model. An equivalent fit is obtained from a non-core-overshooting model of 100 Myrs (right panel). The general shape of the main sequence is matched well to the solar metallicity isochrone. See §3.4 for a discussion of these results.

At this stage, we will digress from defining cluster parameters that will be useful for our white dwarf studies to discuss some other interesting science that this photometry can yield. We will measure the cluster luminosity functions, mass functions, and search for evidence of dynamical evolution and mass segregation in these very young systems.

3.5 Selection of Cluster Members

3.5.1 Previous Estimations and Control Fields

The most comprehensive study of NGC 2168's population (Barrado y Navascues, Deliyannis & Stauffer 2001) used main sequence counting techniques to discover $\sim$ 1700 cluster members in their data. When combined with data from other studies (significantly brighter stars), the total cluster mass, based on an average mass of 0.6 $M_\odot$, is estimated to be $\simeq$ 1600 $M_\odot$. Sung & Bessell (1999) used mass function integrations also to estimate a total mass of 1660 $M_\odot$ for the cluster, although only 640 $M_\odot$ of stars were counted in the

study. An earlier dynamical study by Leonard & Merritt (1989) placed the total cluster mass anywhere in the range 1600–3200 $M_\odot$.

All of these photometric studies of NGC 2168 have been limited in establishing the true cluster population due to its large size. The spatial extent of the cluster easily fills the areal coverage in most detectors and hence there are no documented faint studies of a blank field offset by at least 1 degree from the core. Although there is a small effect in these studies which will underestimate the total cluster population because of missed stars near the edge of the cluster, the true population may actually be overestimated due to improper blank field subtraction. To try and get around this, Barrado y Navascues, Deliyannis & Stauffer (2001) used a wide strip centred on the main-sequence locus and counted all stars within this envelope. Field star subtraction was then estimated by using counts of stars surrounding the main sequence. The filter choices of Barrado y Navascues, Deliyannis & Stauffer (2001) separates the disk stars from the cluster stars better than a V, $B-V$ CMD. However, their cluster luminosity function may still include some faint K and M-type disk dwarfs.

In the study of Sung & Bessell (1999), the observed cluster luminosity function was extrapolated beyond $V \sim 17.5$ (mass function beyond $\sim 0.7\ M_\odot$) based on counts in the Pleiades cluster. However, as mentioned in their paper, this overestimates the contribution of low-mass stars, as the Pleiades sample includes the low-mass dominated outer regions of the cluster, which are not detected by Sung & Bessell (1999). For the brighter stars, they used proper motion selection (a better technique for determining cluster membership). However, for the fainter stars they adjusted zero-age main-sequence (ZAMS) lines in different filters for reddening excesses and computed distances for individual objects. Objects with inconsistent distances are assumed to be disk stars and thrown out.

In the work of Leonard & Merritt (1989), an age of 30 Myrs was used to represent NGC 2168 (from the proper motion work of Vidal 1973), much lower than the value found in recent studies. Additionally, most of the mass in the Leonard & Merritt (1989) study resided in faint main-sequence stars which were beyond the proper motion detection limits. Therefore, an extrapolation was used to integrate the mass function (MF) using a power-law slope below $\sim 1\ M_\odot$. Binary effects and mass-segregation were ignored in the study

Our study also suffers from a lack of field stars. The blank field surrounding the cluster is too small in areal coverage with respect to the cluster field. However, rather than count stars over our entire mosaic we have chosen to build a blank field from the extreme outer regions of our field (an area of 122 square arcmin, outside of $R = 20'$ from the centre of the cluster). This field is almost a factor of 8 smaller in areal coverage than our cluster field. At this radius, the CMD shows no evidence of a main sequence. However, some

cluster stars are most likely still present, as previous proper motion studies have shown (see §3.1). Current generation instruments, such as MEGACAM on *CFHT*, will easily allow a deep blank field to be obtained around this cluster.

For NGC 2323, the only study investigating the luminosity function of the cluster is the $V \leq 14.5$ work of Claria, Piatti & Lapasset (1998). They reported a lower limit on the cluster population of 109 members (285 $M_\odot$). In this case, our areal coverage is not only large enough to encompass almost the entire cluster ($R \sim 15'$), but also large enough so that an almost areal equivalent blank field can be build up from the outer CCDs on the mosaic.

3.5.2   Luminosity and Mass Functions

We identify the cluster stars by first creating main-sequence fiducials (defined by clipping objects with $\Delta(B-V) \geq 3.5$-σ from the mean) after roughly isolating the cluster main sequence from the background distribution. This creates an envelope around the fiducial based on the errors in the photometry (the envelope broadens out towards faint magnitudes). Stars are then counted within this envelope, for both the cluster CMD and the background CMD. The observed cluster luminosity function is the difference between the counts in the two fields, after accounting for the difference in area between the cluster and background fields.

V (mag)	N (NGC 2168)	N (NGC 2323)	Completeness (Cluster/Background)	Comp. Error
9.0–10.0	5.0 ± 2.2	4.0 ± 2.0	1/1	0
10.0–11.0	32.0 ± 5.7	7.0 ± 2.6	1/1	0
11.0–12.0	33.4 ± 9.0	26.8 ± 6.4	1/1	6.9
12.0–13.0	46.5 ± 10.5	45.3 ± 8.2	1/1	8.0
13.0–14.0	73.0 ± 14.1	53.7 ± 10.0	1/1	11.2
14.0–15.0	83.5 ± 17.0	83.4 ± 14.4	1/1	14.3
15.0–16.0	93.5 ± 20.6	99.6 ± 20.0	1/1	18.2
16.0–17.0	76.8 ± 22.3	109.1 ± 23.5	1.02/1	20.5
17.0–18.0	55.0 ± 21.7	149.3 ± 23.0	1/1	20.4
18.0–19.0	81.9 ± 19.9	156.8 ± 26.7	1.03/1.02	17.7
19.0–20.0	176.6 ± 29.0	226.4 ± 34.5	1.08/1.05	25.8
20.0–21.0	162.4 ± 41.3	308.7 ± 49.3	1.13/1.09	39.3
21.0–22.0	52.1 ± 25.7	534.5 ± 75.6	1.21/1.16	24.7
22.0–23.0		259.7 ± 39.7	1.36/1.18	36.3

Table 3.2: Corrected cluster star counts and completeness

Incompleteness corrections are handled by repeatedly introducing a number of artificial stars into the data images. The method used for this has been described in both Kalirai
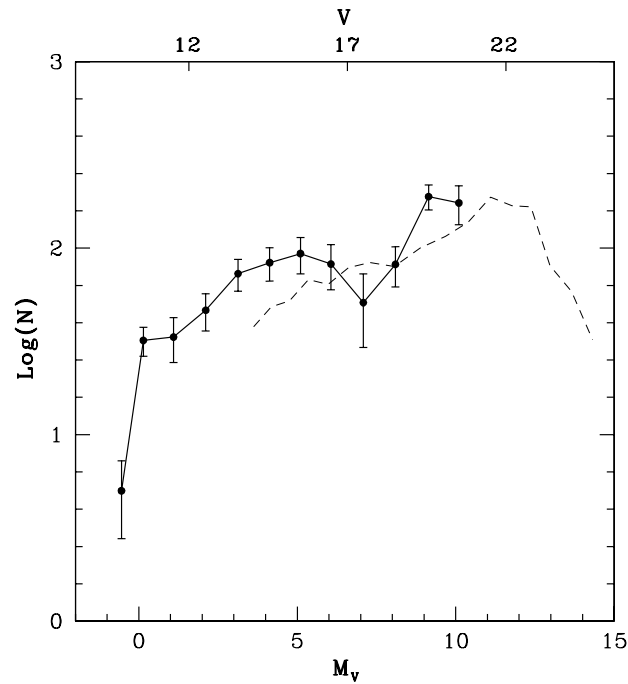
Figure 3.5: NGC 2168 luminosity function after correcting for data incompleteness. The error bars reflect a combination of Poisson errors and incompleteness errors added in quadrature. The NGC 2168 luminosity function from Barrado y Navascues, Deliyannis & Stauffer (2001) is also shown for comparison. The significance of the apparent dip at $M_V = 7$ is discussed in the text.

et al. (2001b) and Kalirai et al. (2001c), so we only present the results here. Table 3.2 shows the statistics for these tests in both the cluster and blank fields (ratio of number added to number recovered) in column 4. The incompleteness tests were carried out for the NGC 2168 data set and the recovered results are used for both clusters. This method is believed to be reliable, since both of these clusters were imaged for identical exposure times and exhibit similar crowding. The corrections found here are very similar to those determined for NGC 2099 in Kalirai et al. (2001c). To summarize: the completeness in the cluster field for main-sequence stars is found to be 73.5% at $V = 22.5$. The errors shown in columns 2 and 3 of Table 3.2 are the quadrature sum of the Poisson and incompleteness errors (shown in column 5).

The final corrected star counts are found by multiplying the cluster and blank field counts by the incompleteness corrections from Table 3.2. The final luminosity functions for each cluster are tabulated in columns 2 and 3 of Table 3.2 (corrected for incompleteness). Figures 3.5 and 3.6 show the corresponding luminosity functions for NGC 2168 (solid
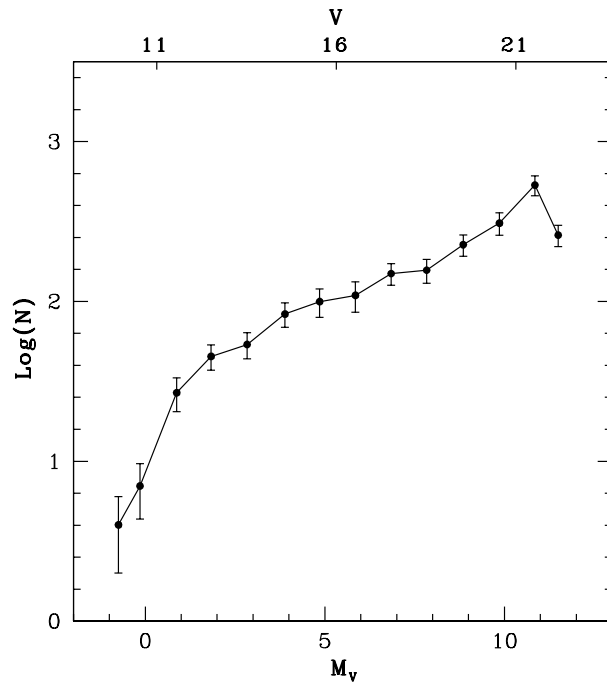
Figure 3.6: NGC 2323 luminosity function is shown after correcting for incompleteness. The luminosity function slowly rises up to $V \sim 21.5$ ($M_V = 10.82$). The error bars reflect a combination of Poisson errors and incompleteness errors.

line) and NGC 2323. For NGC 2168, the luminosity function rises until $M_V = 5$, and then dips down and rises again. This dip is most likely the result of poorer counting statistics and is unlikely to be physical. However, we are unable to fit a straight line through the error bars of the brighter points and the fainter ones without excluding this point. The dip therefore is significant (to within 1-σ). The luminosity function given in Barrado y Navascues, Deliyannis & Stauffer (2001) does not show a dip at this magnitude (dashed line). This line was constructed by using the I band luminosity function in Table 3 of Barrado y Navascues, Deliyannis & Stauffer (2001) and correcting to V by using the empirical fiducial in Table 1 of that paper. For NGC 2323, the luminosity function shows a steady climb all the way to the limit of our data (the final bin shows a drop off that is unlikely to be real). There is some evidence for a slow rise beyond $M_V \sim 8$. This rise is due to the change of slope in the mass-luminosity relation (see e.g., D'Antona 1998), and may also be seen as a change in slope of the cluster main sequence.

By summing the corrected luminosity function, we find a cluster population of just over 1000 stars down to $V = 22$ in the central $20'$ of NGC 2168. The number of stars here has not been corrected for the chopped off area on the N and S edges of the mosaic. Due
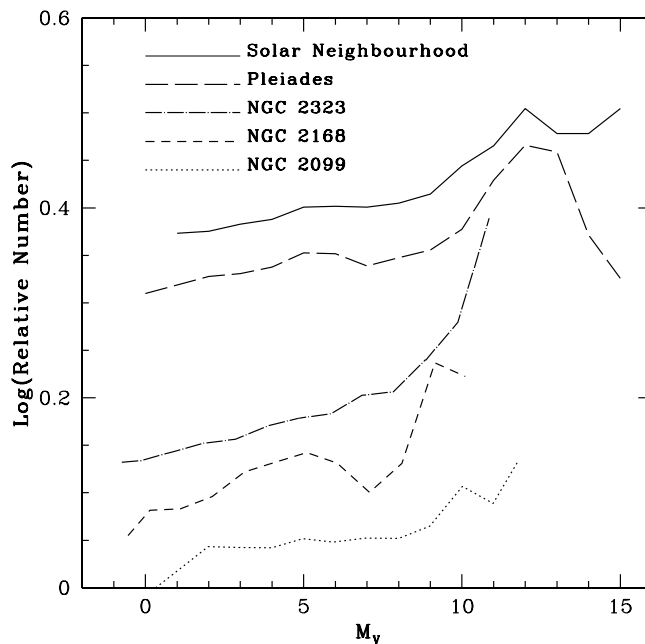
Figure 3.7: Luminosity functions of NGC 2168 and NGC 2323 are compared with those
of the Solar Neighborhood, the Pleiades, and NGC 2099. Each luminosity
function has been normalized by the total number of stars, and then scaled
up arbitrarily. The clusters are shown in terms of increasing age, with the
Pleiades, being the youngest, at the top.

to this, the effective area of the field is actually equivalent to a circular $18'$ field. Since our
background field may contain some cluster stars, the above estimate is likely to be a lower
limit. This number increases significantly when the cluster luminosity function is extended
to the hydrogen burning limit. For this, we normalize our luminosity function with respect
to the Barrado y Navascues, Deliyannis & Stauffer (2001) function, and predict that there
are $\simeq 500$ additional stars between $V = 22$ and 25.

For NGC 2323, we detect $\simeq 2050$ stars in the central $15'$ down to $V = 22$. Again,
since our data does not extend to the lowest mass stars, we use the well known Pleiades
luminosity function (Lee & Sung 1995) to estimate the total population down to $M_V = 15$.
From this, we find that an additional 1150 faint stars would exist in the cluster, raising
the total population to approximately 3200.

Figure 3.7 compares the luminosity functions for both NGC 2168 and NGC 2323 to
that for the Solar Neighbourhood (Binney & Merrifield 1998), the Pleiades (Lee & Sung
1995), and the 650 Myr old rich cluster NGC 2099 (see §4.4; Kalirai et al. 2001c). Each
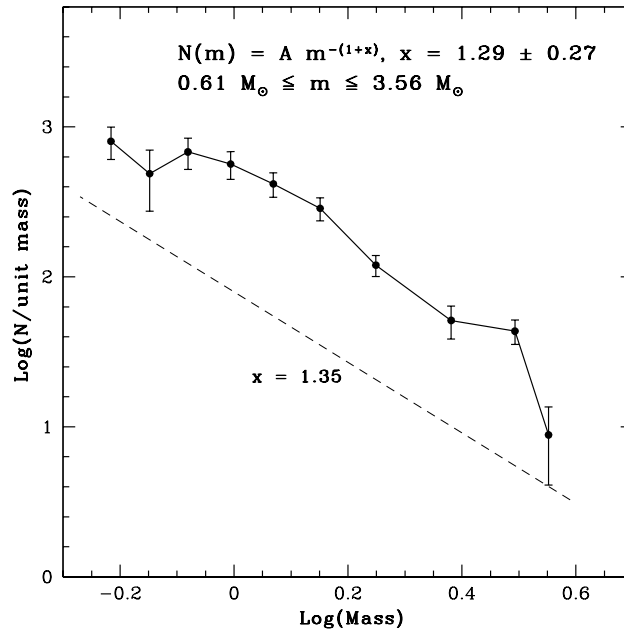
Figure 3.8: NGC 2168 global ($R < 20'$) mass function (solid, $x = 1.29 \pm 0.27$) is found to be consistent with a Salpeter IMF (dashed, $x = 1.35$).

of the functions has first been normalized by the total number of stars and then shifted arbitrarily in the vertical direction. The clusters are presented in order of increasing age, with the Pleiades (the youngest) at the top of the diagram. It is clear that our data do not reach deep enough to see the turn-over in the luminosity functions of NGC 2168 or NGC 2323 (the last data point in each function has been omitted given its large error bar).

To compute the mass functions of these clusters, we multiply the observed luminosity functions by the slope of the mass-luminosity relationship (from the models). The resulting mass function is usually expressed as a power law, $\Psi(m) \propto m^{-(1+x)}$, where $x = 1.35$ represents the Salpeter value. For NGC 6819 (Kalirai et al. 2001b), we found a very flat mass function ($x = -0.15$). This was expected, as the cluster is very old (10 times its dynamical relaxation time). For NGC 2099, the best-fit slope was found to be $x = 0.60$. Other studies, specifically Francic (1989) have shown that older clusters systematically show flatter mass functions. This is believed to be due to the preferential loss of low mass stars, a consequence of dynamical evolution toward energy equiparition.

The mass functions of NGC 2168 and NGC 2323 are presented in Figures 3.8 and 3.9. Fitting a slope to the global NGC 2168 mass function gives a value of $x = 1.29 \pm 0.27$, consistent with the Salpeter slope. Our result falls in the middle of the values found in

$$N(m) = A \; m^{-(1+x)}, \; x = 0.80 \pm 0.34$$
$$0.40 \; M_\odot \leq m \leq 0.69 \; M_\odot$$

$$N(m) = A \; m^{-(1+x)}, \; x = 2.42 \pm 0.14$$
$$0.79 \; M_\odot \leq m \leq 3.90 \; M_\odot$$
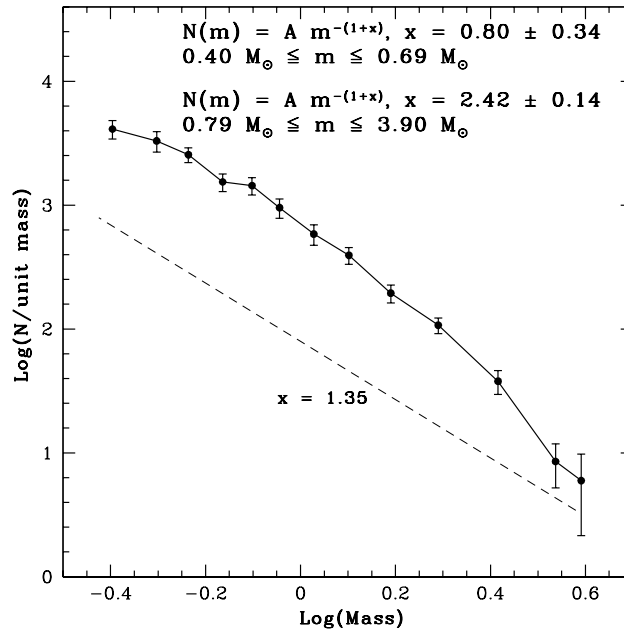
$x = 1.35$

Figure 3.9: NGC 2323 global ($R < 15'$) mass function (solid, $x = 1.94 \pm 0.15$) is found to be steeper than a Salpeter IMF (dashed, $x = 1.35$).

previous studies: Leonard & Merritt (1989) found $x = 1.68$ for the extreme high mass end of the cluster mass function; Sung & Bessell (1999) found a flatter value of $x = 1.1$; and Barrado y Navascues et al. (2001) found $x = 1.59$ for 0.8–6 $M_\odot$. For NGC 2323, we find $x = 1.94 \pm 0.15$ over the mass range (0.40–3.90 $M_\odot$). No previous estimations exist in the literature. Therefore, for the four clusters that we have looked at in the *CFHT* Open Star Cluster Survey (NGC 2323, NGC 2168, NGC 2099, and NGC 6819 in order of increasing age), the mass function is found to be systematically steeper as the cluster age decreases.

Dynamical State and Mass-segregation

As mentioned earlier, young open star clusters are excellent test cases to determine the IMF, as they represent a group of stars with similar age and composition. However, this IMF can only be determined if the cluster has retained the stellar population that it was born with or at least that the population has not suffered from preferential mass loss. This mass loss occurs as the cluster relaxes toward a state of energy equipartition due to distant two-body interactions between all the stars within the cluster. In an equilibrium state, the lower mass stars will be moving with a higher velocity and therefore will be

more likely to be found in the outskirts of the cluster. There, they are preferentially lost from the cluster tidal boundary. Thus, dynamical relaxation leads to mass-segregation, manifested by a systematic change in the slope of the local mass function with radius, and to an evolution of the global cluster MF, generally from a relatively steep slope (high value of x) to a shallower slope, with time. If we can show that there is no evidence of this dynamically induced mass-segregation, then there is a hope of setting constraints on the IMF from the observed MF. If rather, we find that dynamical effects have shifted the stellar distribution, then these dynamical effects can still lead to an important understanding of the timescales and levels of mass-segregation in clusters. The caveat is that we must disentangle dynamical evolution from primordial mass-segregation, a process that may be inherent to cloud collapse to begin with.

Annulus	Radius (′)	Radius (pixels)
NGC 2168		
A1	$0 \leq R < 5$	$0 \leq R < 1456$
A2	$5 \leq R < 10$	$1456 \leq R < 2912$
A3	$10 \leq R < 15$	$2912 \leq R < 4369$
A4	$15 \leq R < 20$	$4369 \leq R < 5825$
Global	$0 \leq R < 20$	$0 \leq R < 5825$
NGC 2323		
A1	$0 \leq R < 3$	$0 \leq R < 873$
A2	$3 \leq R < 7$	$873 \leq R < 2039$
A3	$7 \leq R < 11$	$2039 \leq R < 3204$
A4	$11 \leq R < 15$	$3204 \leq R < 4368$
Global	$0 \leq R < 15$	$0 \leq R < 4368$

Table 3.3: Geometry of annuli used for mass segregation study

Binney & Tremaine (1987) characterize the dynamical relaxation time in terms of the number of crossings of a star that are required for its velocity to change by order of itself, $t_{\rm relax} \sim t_{\rm cross} \frac{N}{8 \ln N}$, where N is the total number of stars. Using our distance and apparent size of NGC 2168, we estimate that the dynamical relaxation age is 110 Myrs, which implies that the cluster age is 1.6 times its relaxation age. For NGC 2323, the dynamical age is 100 Myrs, which gives a cluster age of less than 1.3 times the relaxation age. Hence we expect these clusters to be partially, but not dramatically relaxed.

To investigate signs of mass-segregation, we split the clusters into four annuli (with geometry given in Table 3.3), and present mass functions in each annulus in Figures 3.10 and 3.11. Note that each annulus with a radius greater than about 14′ is cut off horizontally at the top and bottom due to the edges of CFH12K (which are 14.06′ from the centre of the mosaic). The results show that mass-segregation is most likely present in

Figure 3.10: Mass functions in different annuli for NGC 2168 show only mild evidence for mass segregation in the cluster (steeper mass function in the outer rings) in the cluster.

both clusters. The outer annuli have steeper mass functions, indicating more lower mass stars relative to higher mass ones. Surprisingly, the effect is much more prominent in the younger NGC 2323, for which the mass function slope goes from $x = 2.74 \pm 0.40$ in the outer annulus ($11' \leq R < 15'$) to $x = 0.82 \pm 0.27$ in the innermost annulus ($0' \leq R < 3'$). For NGC 2168, the mass function slope changes from $x = 1.48 \pm 0.96$ in the outer annulus ($15' \leq R < 20'$) to $x = 0.66 \pm 0.32$ in the innermost annulus ($0' \leq R < 5'$).

As mentioned earlier, the mild mass-segregation that we see in these young clusters could be primordial. Different clusters themselves may form with different concentrations of high mass stars in the core, and low mass stars in the halo. This type of initial mass-segregation has been observed in extremely young open clusters (Zinnecker 1994) where the clusters are younger than the estimated relaxation timescales. Formation scenarios for these young clusters stress that the rapidity and efficiency of star formation is crucial in determining the final distribution of the stars (Battinelli & Capuzzo-Dolcetta 1991). Supernovae and stellar winds from the first generation of stars can effectively blow away remaining gas in the system to make the cluster unstable. The subsequent dynamical evolution of the cluster will be affected by the timescales of this gas removal (Stecklum
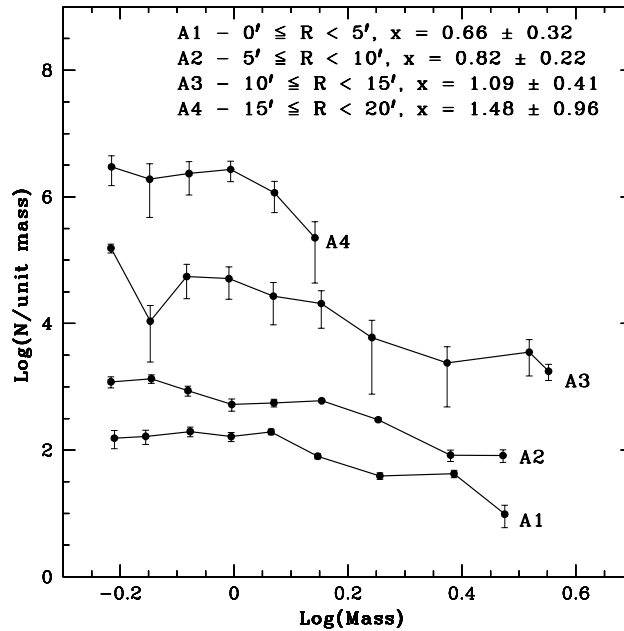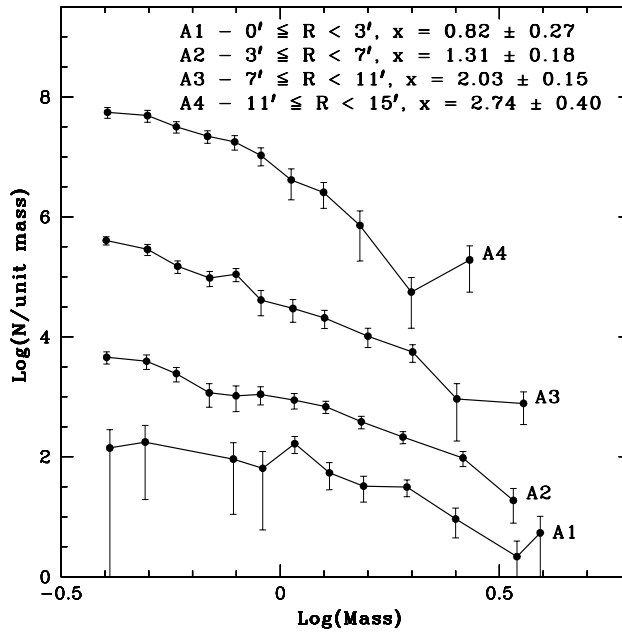
Figure 3.11: Mass functions in different annuli for NGC 2323 show clear evidence for mass segregation (steeper mass function in the outer rings) in the cluster despite its age being only 1.3 times the dynamical relaxation age.

1989). As for the IMF, it too depends on the local conditions of cloud collapse. For example, the final slope of the IMF will depend on how many cloudlets formed protostellar cores through collisions before the gravitational influence of the collapse ceased to be important (Murray & Lin 1996). Since the collisional frequency of the cloudlets will be greatest in higher density regions, such as the centers of clusters, more massive stars will also preferentially form in the centre. This leads to a natural mass-segregation within the cluster.

We can resolve these two cases of mass-segregation induced either from dynamical evolution or primordial mass-segregation by looking for signs of energy equipartition. Generally, dynamical mass-segregation can be demonstrated if stars of different masses obey the radial distributions predicted by multi-mass King models (Gunn & Griffin 1979).

3.6 White Dwarfs

The global goal of our Survey is to first identify white dwarf candidates in open star clusters and then obtain spectra to determine their masses. This will help us understand

both the upper mass limit to white dwarf production and the initial-final mass relationship which is a critical input for calculating ages from white dwarf cooling. The upper mass limit is also important in chemical evolution models of galaxies as it sets the lower mass limit for type II supernova.

3.6.1 Previous Results in the *CFHT* Open Star Cluster Survey

The first cluster that we looked at in the *CFHT* Open Star Cluster Survey was NGC 6819 (Kalirai et al. 2001b). Figure 3.12 shows the CMD for the cluster before any source rejection (left) and after we have imposed some constraints (middle and right). The constraints are: (1) only accept objects with a stellarity confidence index above 0.50 (middle); and (2) only accept those objects which also survive a subtraction procedure for statistically removing field objects (right). Even at a 0.50 stellarity cut, some of these objects could still be faint unresolved galaxies, AGN, or some other non-cluster object. We note, however, that a significant portion of the remaining objects have a very high stellarity, >0.9. Criterion (2) has been addressed by eliminating possible field objects in the cluster data that are in the same vicinity of the CMD as background field objects. We invoke this approach for a small region in the CMD surrounding and including all possible cluster white dwarfs, and use a nearest neighbour approach to eliminate objects. These objects are shown below the dashed line in Figure 3.12 (middle panel). The statistical subtraction shows that there is an over-density of objects in the cluster field. However, we cannot say for sure whether an individual object that we have removed is in fact a field object.

The statistically subtracted and star/galaxy corrected CMD (Figure 3.12, right panel) indicates a clear separation between the white dwarfs and the field stars. This potential white dwarf cooling sequence is separated from these field stars by an average of ~ 0.6 magnitudes in colour on the CMD. There are very few objects between the two populations. However, the putative white dwarf cooling sequence that is revealed is not particularly tight, as there is some evidence for a gap between these bluer objects and a redder potential white dwarf sequence. This is more easily seen on the next Figure, which presents a zoomed in view of the white dwarf region of the CMD. For the adopted reddening value of the cluster, no reasonable mass white dwarf cooling sequence fits the reddest objects in this location of the CMD. It is unlikely that photometric spread is causing some of these objects (the redder objects) to deviate so much in colour from those that agree with the 0.7 $M_\odot$ cooling sequence (Wood 1995). In Kalirai et al. (2001b), we concluded that a more likely scenario to explain the positions of these objects in the CMD is that they are just excess background or foreground objects which were not removed in the statistical subtraction. Alternatively, some could also be highly reddened background white dwarfs.
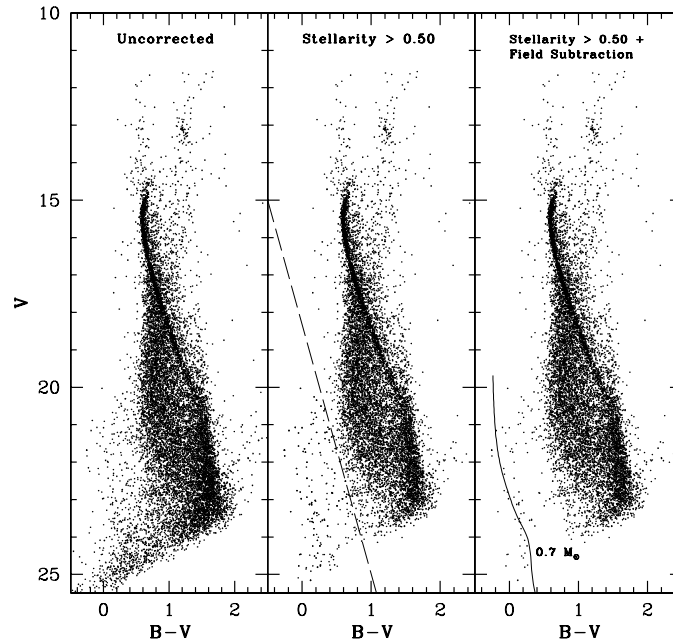
Figure 3.12: Uncorrected CMD for NGC 6819 (left panel). There is a general spread of stars in the lower left corner. After correcting for extended sources (centre panel) and field star subtraction (blue of dashed line, middle panel), a potential white dwarf cooling sequence is evident (right panel). We also show a 0.7 $M_\odot$ white dwarf cooling sequence which agrees with the bluest potential white dwarfs. This analysis is a purely statistical method of determining the most likely location on the CMD of the cluster white dwarfs.

Recently, Hurley & Shara (2003) used an N-body numerical code to model the NGC 6819 white dwarf population in our data. They find that the present morphology of the white dwarf cooling sequence in this cluster can be explained very well by invoking binary interactions in the cluster. Further support for this idea is provided by looking at the very rich population of blue stragglers in this cluster. Because of mass exchange and common envelope evolution, some white dwarfs in the cluster are believed not to evolve along the single degenerate cooling sequence. Figure 3.13 shows the observed NGC 6819 cooling sequence and the simulated sequences for various binary fractions of the cluster. The results clearly indicate that the morphology of the observed sequence is remarkably similar to the simulated sequence for a 50% primordial binary fraction in the cluster. This work represents the first ever finding of a putative binary white dwarf cooling sequence. Follow up spectroscopic observations, in collaboration with Dr. Jarrod Hurley, are planned.
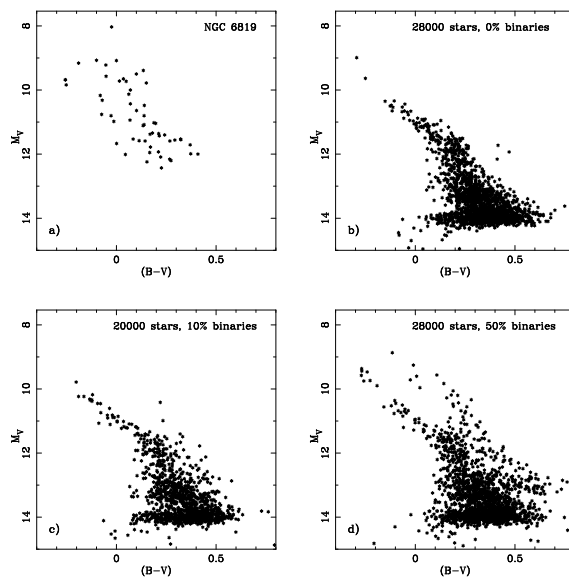
Figure 3.13: The observed NGC 6819 white dwarf cooling sequence (top left) is found to agree well with the brighter end of the simulated sequence for a 50% cluster binary fraction (bottom right).

The next cluster that we looked at in the *CFHT* Open Star Cluster Survey was NGC 2099. In this cluster we found a rich population of 50 white dwarfs and statistically estimated the white dwarf cooling age of the cluster to be 560 Myrs from the faintest white dwarfs. This is the cluster for which we are following the imaging study with spectroscopy of candidate white dwarfs using *Gemini*. That project is described in detail in Chapter 4, and so we will discuss those white dwarfs later.

3.6.2   White Dwarfs in NGC 2168 and NGC 2323

White dwarfs in NGC 2168 and NGC 2323 represent the most important sample in our study, as they constrain the high mass end of the initial-final mass relationship, where there are very few data points. With core-overshooting main-sequence turn-off masses of $\sim 5~M_\odot$, some white dwarfs in both of these clusters are expected to have massive progenitors.

Our photometry for these clusters is deep enough to detect the faintest white dwarfs which could have cooled during the lifetime of the clusters. Based on the cluster ages, we expect the faintest white dwarfs (assuming $1.0~M_\odot$ objects) in both clusters to be located at $V \simeq 22$. The younger age of NGC 2323 pushes this limit to a brighter magnitude. However, the larger distance modulus has an opposing effect. The combination of small number

statistics in the faint-blue end of the CMDs and much smaller blank fields do not allow us to build white dwarf luminosity functions. We will, however, attempt an estimation of the field white dwarf numbers by scaling up the blank field numbers to the area of the cluster field, and also by using the Galactic disk white dwarf luminosity functions (Leggett, Ruiz & Bergeron 1998). Previously, the only white dwarfs spectroscopically confirmed in either of these clusters are the two objects measured by Reimers & Koester (1988) in NGC 2168. We believe further spectroscopy of new candidates selected from the present photometry of this cluster will yield more objects. The cleaned CMDs (removal of galaxies and image defects, see §3.3) do show some concentrations of objects. For example, a clump of objects can be seen in NGC 2168 between $21 \leq V \leq 22.5$ at $B - V \simeq 0$. For NGC 2323 more of a scattered distribution of stars is seen in the white dwarf region.

We can predict the number of expected white dwarfs in each of these clusters by integrating the main-sequence mass functions from the present day turn-off mass to the upper limit for white dwarf production. For the latter, our models show $M_{\rm up} \sim 7\ M_\odot$, however, the value could be as low as $5.5\ M_\odot$ (Jeffries 1997). The calculation of the number of expected white dwarfs assumes that the observed mass function shape is similar to that for the higher masses which have evolved off the main sequence. Given both the range of masses represented by the present day mass functions (for NGC 2323, $0.4\ M_\odot$ to $3.9\ M_\odot$), and the smoothness of the data, only a mild extrapolation to higher masses is needed for these young clusters. For NGC 2168, we use the mass function slope from $0.83\ M_\odot$ to $3.56\ M_\odot$ ($x = 1.75$) to estimate 18 expected white dwarfs in our cluster field. For NGC 2323, the mass function slope from $0.79\ M_\odot$ to $3.90\ M_\odot$ ($x = 2.42$) predicts 6 white dwarfs in the cluster.

Before we can compare the number of white dwarfs seen to the number expected, we must first remove the number of field white dwarfs (assuming galaxies have already been removed through the stellarity cut). For this, we use the disk white dwarf luminosity function (Leggett, Ruiz & Bergeron 1998) and scale the number to our field of view. Since the Galactic disk is much older than these two clusters, we must truncate the counts in the field at the bright magnitudes, which are represented by the white dwarf cooling limits of the clusters. For the NGC 2168 field, the disk white dwarf luminosity function predicts 4 white dwarfs down to $V = 22$. For NGC 2323, 3 field white dwarfs are predicted in the cluster field of view down to $V = 22$ (12 are predicted down to the limiting magnitude). Counting objects on the CMD, and eliminating the blank field numbers gives 14.5 white dwarfs in NGC 2168 after accounting for incompleteness errors. This number is in excellent agreement with the 18 estimated from the mass function extrapolation. For NGC 2323, 5 white dwarfs are found after the statistical subtraction and 6 were predicted. Although we do not know which of the objects on our CMD are cluster white dwarfs, we now have

candidates for multi-object spectroscopic observations in these two clusters.
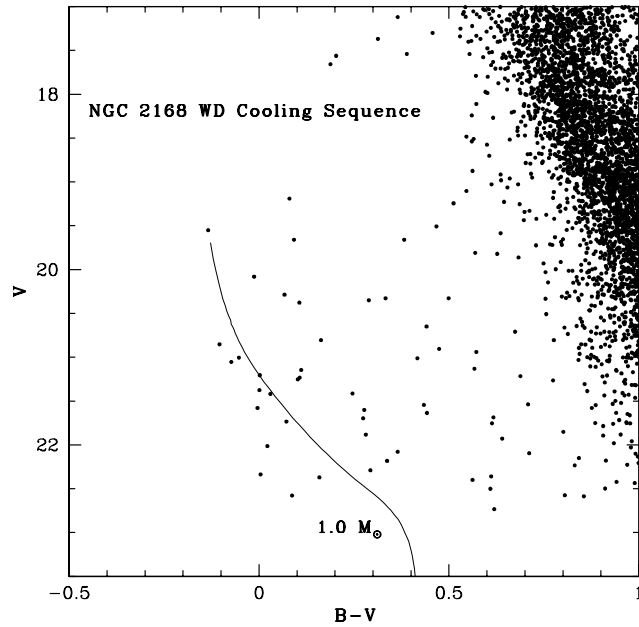
Figure 3.14: A 1.0 $M_\odot$ white dwarf cooling sequence (Wood 1995) is shown with respect to the potential white dwarfs in NGC 2168. The clump of objects located at 21 $\leq V \leq 22$, $-0.15 \leq B{-}V \leq 0.1$ falls slightly fainter than the cooling model, indicating that these are massive white dwarfs. The white dwarf cooling age from the faintest of these stars is found to be 190 Myrs, and therefore in excellent agreement with the main-sequence turn-off age (180 Myrs). Even fainter objects are likely to be field white dwarfs.

In Figure 3.14, we show a 1 $M_\odot$ cooling model (Wood 1995) with respect to the clump of potential white dwarfs in NGC 2168. The best white dwarf candidates are the 8 objects clustered together in the range $21 \leq V \leq 22$, $-0.15 \leq B{-}V \leq 0.1$. These are all found to be slightly fainter than this cooling sequence, suggesting perhaps an even higher mass and therefore a potentially very important constraint on the white dwarf initial-final mass relationship and upper mass limit to white dwarf production. For the 1 $M_\odot$ model, the corresponding white dwarf cooling ages for these objects range from 30 to 190 Myrs. These values are in excellent agreement with the expected white dwarf cooling ages from stars which have evolved off the main sequence in this young cluster. Therefore, if the clump of objects in NGC 2168 comprises bona fide cluster white dwarfs, then we can conclude that the white dwarf cooling age of the cluster (190 Myrs) is in good agreement with the

main-sequence turn-off age (180 Myrs). For the former age, we would also need to add on $\sim$ 50 Myrs for the main-sequence lifetime of a progenitor 7 $M_\odot$ star before making any comparisons. NGC 2168 can therefore uniquely set very important constraints on the initial-final mass relationship and should be a priority cluster for future spectroscopic work.

3.7 Summary of White Dwarfs in Star Clusters

Deep photometry of NGC 2168 and NGC 2323 in the V and B filters has allowed us to produce the tightest main sequences to date for these clusters. NGC 2168 is found to contain $\simeq$ 1000 stars brighter than $V = 22$, beyond which we can not reliably trust the luminosity function. In NGC 2323 we find $\simeq$ 2050 stars above the photometric limit of $V \simeq 23$. After accounting for uncertainties in the reddening, main-sequence fitting, extinction and metallicity, the distance to NGC 2168 is determined to be 912^{+70}_{-65} pc. For NGC 2323, we find $d = 1000^{+81}_{-75}$ pc. By comparing a new set of theoretical isochrones to the observational CMDs, we have determined both the ages of the clusters (180 Myrs for NGC 2168, 130 Myrs for NGC 2323) and also find a nice agreement between the theoretical isochrone and the observational main sequence. Spectroscopic confirmation of potential white dwarfs in both clusters is important for setting high mass constraints on the initial-final mass relationship. A summary of the results from this Chapter is given in Tables 3.4 and 3.5.

Position:		
α (J2000)	RA	$= 06^{\mathrm{h}}08^{\mathrm{m}}54.0^{\mathrm{s}}$
δ (J2000)	declination	$= +24^{\mathrm{o}}20.0'$
l	Galactic longitude	$= 186.58^{\mathrm{o}}$
b	Galactic latitude	$= 2.18^{\mathrm{o}}$
Distance and Reddening:		
$(m-M)_V$	apparent distance modulus	$= 10.42 \pm 0.13$
$E(B-V)$	reddening	$= 0.20$
A_V	visual extinction	$= 0.62$
$(m-M)_0$	true distance modulus	$= 9.80 \pm 0.16$
d	distance from Sun	$= 912^{+70}_{-65}$ pc
z	distance above Galactic plane	$= 36.6$ pc
Age:		
$t_{\mathrm{Dynamical}}$	dynamical relaxation timescale	$= 110$ Myrs
$t_{\mathrm{Isochrone}}$	main-sequence turnoff age	$= 180 \pm 20$ Myrs
t_{WD}	white dwarf cooling age	$\simeq 190$ Myrs
Metallicity:		
Z	heavy metal abundance	$= 0.012 \pm 0.003$
Size:		
D	linear diameter	$= 10.6$ pc
Θ	angular diameter	$= 40'$
N	number of stars down to $M_V = 15$	$\simeq 1500$
Stellar Distribution:		
α	mass function slope (Salpeter = 2.35)	$= 2.29 \pm 0.27$

Table 3.4: Summary of results for NGC 2168

Position:

α (J2000)	RA	$= 07^{\mathrm{h}}02^{\mathrm{m}}48.0^{\mathrm{s}}$
δ (J2000)	declination	$= -08^{\mathrm{o}}22'36''$
l	Galactic longitude	$= 221.67^{\mathrm{o}}$
b	Galactic latitude	$= -1.24^{\mathrm{o}}$

Distance and Reddening:

$(m-M)_V$	apparent distance modulus	$= 10.68 \pm 0.14$
$E(B-V)$	reddening	$= 0.22$
A_V	visual extinction	$= 0.68$
$(m-M)_0$	true distance modulus	$= 10.00 \pm 0.17$
d	distance from Sun	$= 1000^{+81}_{-75}$ pc
z	distance below Galactic plane	$= 22.7$ pc

Age:

$t_{\mathrm{Dynamical}}$	dynamical relaxation timescale	$= 102$ Myrs
$t_{\mathrm{Isochrone}}$	main-sequence turnoff age	$= 130 \pm 20$ Myrs
t_{WD}	white dwarf cooling age	$= $ ———

Metallicity:

Z	heavy metal abundance	$= 0.020$

Size:

D	linear diameter	$= 8.72$ pc
Θ	angular diameter	$= 30'$
N	number of stars down to $M_V = 15$	$\simeq 3200$

Stellar Distribution:

α	mass function slope (Salpeter = 2.35)	$= 2.94 \pm 0.15$

Table 3.5: Summary of results for NGC 2323

Chapter 4

Spectroscopy of White Dwarfs

As mentioned in the previous Chapter, the *CFHT* Open Star Cluster Survey has been a highly successful probe of white dwarfs in open star clusters. We have now successfully found over 100 white dwarf candidates in the four richest clusters. The next phase of our program is to obtain confirmation of the white dwarf nature of these stars using spectroscopy. In fact, this was the original motivation for obtaining the data for the Survey. With high quality spectra of white dwarfs, we can fit atmosphere models to the hydrogen absorption lines and measure both effective temperatures and gravities for each white dwarf. Linking this information to white dwarf cooling models gives white dwarf masses, from which we can constrain a key relation in astrophysics, the initial-final mass relation. This relation defines how much mass stars lose through their evolution. Additionally, if we are successful in confirming a large number of white dwarfs in these clusters, we can investigate several other questions, such as the fraction of hydrogen white dwarfs (DA) to helium white dwarfs (DB), and the upper mass limit to white dwarf production.

4.1   Introduction

The initial-final mass relationship connects the mass of the final products of stellar evolution, white dwarfs, to the mass that they once had when they were burning hydrogen as main-sequence stars. This mapping of masses remains today as one of the most poorly understood areas of stellar evolution. Despite this, the relationship has been used extensively in several astrophysical applications. For example, the initial-final mass relationship is a key ingredient needed to determine white dwarf cooling ages of star clusters. Hansen et al. (2004) have recently measured the age of the globular cluster M4 to be 12.1 Gyrs using the white dwarf luminosity function. This age determination complements recent Wilkinson Microwave Anisotropy Probe (*WMAP*) results (Spergel et al. 2003) and reveals that

---

[3]A version of this chapter has been submitted for publication. Kalirai, J.S., Richer, H.B., Reitzel, D., Hansen, B.M., Rich, R. M., Fahlman, G.G., Gibson, B.K., and von Hippel, T. (2004) The Initial-Final Mass Relationship: Spectroscopy of White Dwarfs in NGC 2099 (M37). Astrophysical Journal Letters, submitted Sept. 17, 4 pages.

globular cluster formation occurred 1.6 Gyrs after the Big Bang. The initial-final mass relationship is also very important for chemical evolution models of our Galaxy. During their evolution, stars can lose up to 80% of their mass, all of which is expelled into the interstellar medium. This enrichment plays an important role in the properties of second generation stars and the chemical makeup of galaxies. An independent reason one would like to understand the initial-final mass relationship is to constrain the lower mass limit to type II supernova explosions. The latter constrains supernova rates (van den Bergh & Tammann 1991) which are vital ingredients in our understanding of feedback processes and star formation in galaxies (e.g., Somerville & Primack 1999). If constrained well enough, the initial-final mass relationship can directly yield the maximum initial mass for white dwarf production, which is equivalent to the lower mass limit for a type II supervova. Currently, this number varies between 5 $M_\odot$ and 10 $M_\odot$ (Jeffries 1997). Williams (2002) points out that a reduction of this mass limit from the canonical 8 $M_\odot$ value to 5 $M_\odot$ increases the number of type II supernova by about a factor of two, thereby drastically changing the energetics involved in feedback processes. There are many other reasons to study the initial-final mass relationship, such as constraining the birth rates of neutron stars, that we will not discuss in detail here.

Most of the mass loss that a star suffers through its evolution occurs during very short lived post-main-sequence evolutionary phases such as the red giant branch (RG), asymptotic giant branch (AGB) and planetary nebula (PN) phases. In principal, the masses of the stellar cores during these last phases of stellar evolution could be determined directly from modelling the AGB phase and comparing with observations. An ideal model would then take an initial star of a certain mass ($M < 8 \ M_\odot$) and evolve it through all phases of stellar evolution to give a white dwarf with a certain mass. However, in practice the mass loss mechanisms and thermal pulses on the AGB are not yet theoretically understood well enough to provide any reliable constraints on the mapping of the initial stellar mass to the remaining core mass (see the review by Habing 1996 for more information). Detailed observations are also rare, given the short lifetimes of these phases ($\sim 10^5$ years), and heavy obscuration of the central star by dusty shells.

Another method to link the initial progenitor mass to the final white dwarf mass, is to directly observe white dwarfs in star clusters and use knowledge of the cluster age to determine the initial mass. The white dwarf masses and temperatures can be obtained from spectroscopy, and the cluster age can be determined by using main-sequence stellar evolution models. Given the mass and temperature of a white dwarf, the white dwarf cooling age (i.e., the age of the star after the AGB and PN phases) can be easily determined using cooling models (e.g., Wood 1995; Hansen 1999). Subtraction of this cooling age from the star cluster age directly gives the main-sequence lifetime of the progenitor star that

created the white dwarf. This latter age will include the small amount of time spent in post-main-sequence evolutionary phases as well. Stellar evolution models then directly yield the correct initial mass of the progenitor, given this pre-white dwarf lifetime.

The latter approach of using white dwarfs in open clusters to constrain the initial-final mass relationship has only been marginally successful. White dwarfs, being the end product of stellar evolution in intermediate mass stars, contain essentially no nucleur fuel and hence cannot generate heat. The stars will continue to release any remaining stored thermal energy and become dimmer with time. As a result, finding white dwarfs requires nearby samples or very deep photometry. Furthermore, finding large samples of white dwarfs in star clusters requires rich clusters. Unfortunately, there are few of these clusters nearby and most of the richest also tend to be the oldest, thereby placing the white dwarfs at fainter magnitudes. This is in part due to the quick disruption of poorly populated clusters by giant molecular clouds and tides in the Galaxy (Wielen 1991). Therefore, constraints on the initial-final mass relationship require a careful interplay between selecting rich clusters that are old enough to produce a substantial population of white dwarfs and yet young enough so that the white dwarfs have not cooled to immeasurably faint magnitudes. Pin-pointing one of these clusters would allow for a homogenous study of its white dwarfs rather than relying on a few objects from many young clusters. NGC 2099 is such a cluster, containing over 3000 stars and an age of 0.5 Gyrs (Kalirai et al. 2001c). With a turnoff mass of $\simeq 2.5\ M_{\odot}$, we would intuitively expect the white dwarfs in NGC 2099 to be quite massive, as their progenitor stars must have had a mass $>2.5\ M_{\odot}$.

In the next section we discuss the few studies in the past 30 years that have been able to provide constraints on the initial final mass relationship. The majority of these rely on the pioneering work of Dr. Volker Weidemann, both observationally and theoretically, and the almost two decades long efforts of Dieter Reimers and Detlev Koester. Next, in §4.3, we discuss at length the technical details about the new spectroscopic observations and data reduction for this project. We then briefly describe some properties of the rich cluster NGC 2099 from our previous imaging study with *CFHT* (Kalirai et al. 2001c). Recent constraints on both the cluster metallicity and reddening are presented and the age of the cluster is updated reflecting this information (§4.4). The spectra of 25 white dwarfs are provided in §4.5 and modelled to derive masses in §4.6. Finally, we present and discuss our new initial-final mass relationship in §4.7.

4.2 Previous Work on the Initial-Final Mass Relationship

The initial-final mass relationship was first examined in detail by Weidemann (1977) by comparing some theoretical relations (i.e., Fusi-Pecci & Renzini 1976) of mass loss to the

masses of a few white dwarfs in both the Pleiades and Hyades star clusters. A few years later, Romanishin & Angel (1980) searched for and found white dwarf candidates in open clusters by comparing the numbers of faint blue objects to those in blank fields. Koester & Reimers (1981) spectroscopically confirmed four of these objects, in NGC 2287 and NGC 2422, and found three additional white dwarfs spectroscopically in NGC 2516 (Reimers & Koester 1982). This led to a relatively flat white dwarf initial-final mass relationship (white dwarf mass is almost independent of the progenitor mass), indicating, for example, that 3 $M_\odot$ main-sequence stars produce 0.5–0.6 $M_\odot$ white dwarfs (Weidemann & Koester 1983). With only about a dozen data points spanning the entire initial-final mass plane, Weidemann & Koester (1983) were still able to conclude that the maximum mass for white dwarf production should be raised from 4–5 $M_\odot$ to 8 $M_\odot$, in excellent agreement with theoretical upper mass limits for the development of a carbon-oxygen core (Iben & Renzini 1983). Koester and Reimers continued finding a few white dwarfs in each of several young open clusters. These earlier results are summarised in Reimers & Koester (1988b). Weidemann (1987) calculated a semi-empirical initial-final mass relationship based on the data available at the time. The relationship is relatively flat for initial masses less than 3 $M_\odot$, and then curves upward to a maximum mass of 1.15 $M_\odot$ at an initial mass between 8–9 $M_\odot$.

Several important changes to the initial-final mass relationship were made in the 90's given the abilities of CCDs, larger telescopes, and more computing power. As Weidemann (2000) discusses, the masses of the Hyades white dwarfs were found to be previously underestimated. The age of the cluster was also found to be younger than previously measured (Perryman et al. 1998), thereby changing the calculated initial masses of the progenitor stars. Weidemann (2000) presents a nice summary of the improvements made, as well as new observations of white dwarfs in open clusters throughout the 90's. He concludes with an initial-final mass relationship containing 20 data points. The scatter in the relationship is, however, quite large. Initial masses near 3.5 $M_\odot$ are found to produce white dwarfs ranging anywhere from 0.65–0.8 $M_\odot$. Weidemann (2000) also discounts the measurements of Jeffries (1997) who, based on an improved metallicity of NGC 2516, calculated the initial progenitor masses of four cluster white dwarfs to be between 4.5–5 $M_\odot$. This is very surprising, given that the masses of these white dwarfs are all between 0.9–1.05 $M_\odot$, thereby resulting in an extremely steep relationship.

More recently, there has been another study that has put new data points on the initial-final mass plane. Claver et al. (2001) present masses of six new white dwarfs in the Praesepe open cluster. These objects further illustrate the scatter in the plot, with two white dwarfs of mass 0.91 $M_\odot$ and 0.63 $M_\odot$ both apparently having the same initial progenitor mass (3 $M_\odot$).

As the above studies show, it is extremely desirable to heavily populate the initial-final mass plane with many white dwarfs, all of which are reduced in a homogenous manner. To this end, we began the *CFHT* Open Star Cluster Survey (Kalirai et al. 2001a) to catalogue hundreds of white dwarfs in rich open star clusters. So far, we have looked at over 22 clusters and have selected the richest six for further investigations. Results on four of the clusters have been published in our *CFHT* series of papers (Kalirai et al. 2003; 2001b; 2001c). Simulateneously, we have begun a large program at the *Gemini North* telescope to obtain follow up multi-object spectroscopy of the candidate white dwarfs and to measure their masses. Here, we present the first results from that project, a homogenous study of 25 white dwarfs in NGC 2099.

4.3   Observations

In Figure 4.1 we present a $42'$ x $28'$ image of NGC 2099 obtained with the CFH12K detector at *CFHT* in 1999 (see Kalirai et al. 2001c). In the *CFHT* study, we identified 50 white dwarf candidates in NGC 2099 within the central $15'$ of the cluster. These objects were selected based solely on their location in the colour-magnitude diagram and passing the stellarity grade (>0.5 in both filters). The latter cut ensures minimum contamination from resolved galaxies in the field. A preliminary plot of the locations of the white dwarf candidates in the cluster provided us with three obvious field choices for spectroscopic follow up. These were manually shifted around the entire image until we statistically had the highest number of candidates in each one. Other factors, such as avoiding very bright foreground stars, also affected the field selection. For these fields, we will obtain multi-object spectroscopy of all white dwarf candidates using both the *Gemini* and *Keck* telescopes.

4.3.1   Gemini Data

Gemini Imaging Fields

In order to confirm the white dwarf nature of our candidates, we first obtained deep images of three smaller fields within NGC 2099 using the GMOS imager/spectrometer on *Gemini* (Murowinski, R. et al. 2002). The GMOS detector is composed of 3 CCDs with a pixel scale of $0.''0727$/pixel, projecting to a $5.'5 \times 5.'5$ area on the sky. The primary goal of the imaging was to provide accurate astrometry for the locations of the white dwarf candidates. We had hoped to also fill in some of the incompleteness (80% at $V = 23.5$) in the *CFHT* study and thereby increase the number of white dwarf candidates. Multiple exposures in both the g' and r' filters were obtained for a total length of 20 minutes in each filter. These
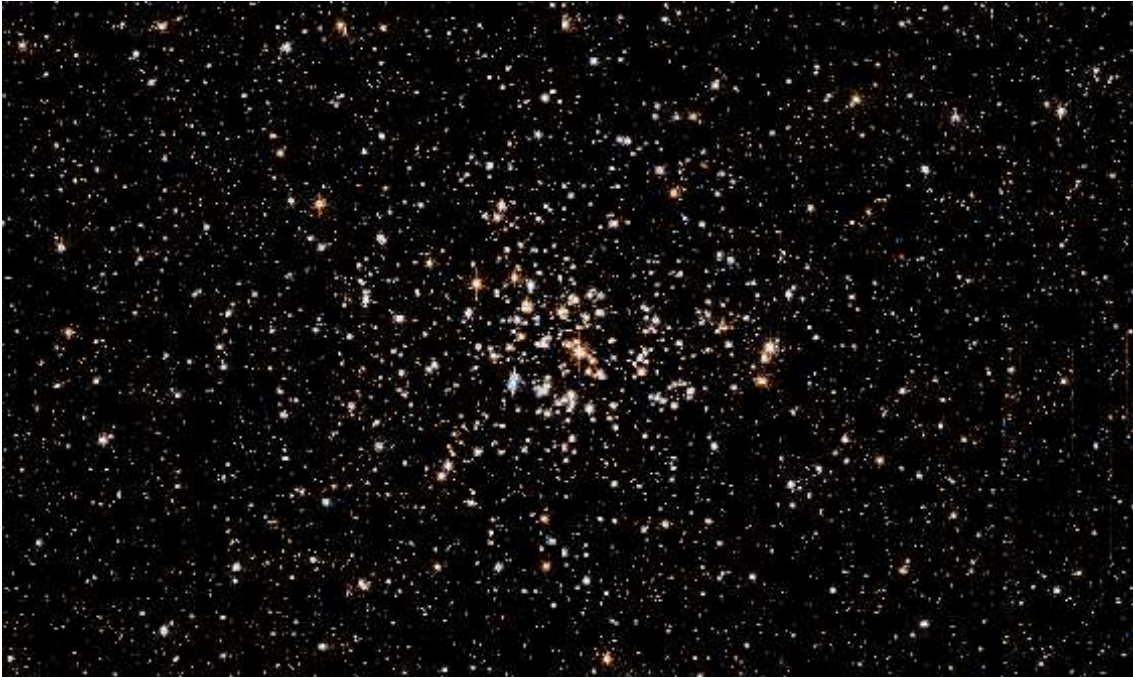
Figure 4.1: A colour image of the cluster NGC 2099 is shown. This *CFHT* image measures $42' \times 28'$.

filters most closely resembled our *CFHT BV* study. The images were provided to us very quickly in order to facilitate the follow up spectroscopic observations (see below). The data were pipeline processed at *Gemini* to remove instrumental signatures, such as pixel-to-pixel variations across the mosaic and bias levels. These procedures used the *Gemini* IRAF v1.3 reduction tools. In the final images, we detected all of the white dwarfs from the earlier *CFHT* observations, but were unable to find any new candidates. The best of the three fields showed 8 strong white dwarf candidates (same as *CFHT* candidates). An additional marginal candidate was also included in this field although this star appeared to be too red for a cluster white dwarf.

Gemini Spectroscopy Field

The success of this study requires multi-object spectroscopy given the large exposure time required to obtain enough signal-to-noise to identify and fit white dwarfs with models. These observations would not be feasible if we could only observe one white dwarf at a time using long-slit spectroscopy. With multi-object spectroscopy, we can simultaneously obtain spectra for 30–40 objects in a small field. The procedure first requires imaging the

field in order to define the locations of the stars for which spectra will be obtained, and then building a mask which only allows the light from tiny slits centred on these stars to be fed into the spectrograph's aperture (Crampton et al. 2000). The remaining light from other stars in the field is blocked out and does not affect the observations. The precise cutting of the slitlets in the mask is completed with a laser milling machine located in Hawaii. The sizes and positions for each slitlet must be defined by the observer based on the imaging data prior to any spectroscopic observations. This is done through a software program that reads in the input images.

A multi-object mask was prepared for the one field using the *Gemini* Mask Making Software. We prioritized the white dwarfs on the mask and included several additional objects which are scientifically interesting in this cluster. These are mostly faint M-type dwarfs on the lower main-sequence of the cluster. In total, 32 science slits were cut on the mask; for the 8 white dwarf candidates, one marginal candidate, and 23 other stars. An additional 5 box slits ($2'' \times 2''$) were also included at the locations of relatively bright cluster stars to help align the mask on the sky with short exposure times (see Figure 4.2). The science slits were are all $5''$ long and $0.75''$ wide. We used the B600_G5303 grating which simultaneously covers 2760 Å at $R = \lambda/\Delta\lambda = 1688$. The grating was centred at a wavelength of 4620 Å for half the exposures and 4720 Å for the other half (see below). This ensures spectral coverage of H_β, H_γ, and possibly higher order Balmer lines. As we will see later in §4.5, the exact spectral coverage for any given star in multi-object spectroscopy depends slightly on the location of the star on the mask. Therefore, some candidates have slightly bluer or redder spectral coverage. The spectra are binned by a factor of four in the spectral direction and two in the spatial direction to improve the signal-to-noise.

Twenty-two individual 1-hour exposures were obtained on the field in NGC 2099. The observations were spread over 22 days and taken at low airmasses (<1.2) and good seeing ($\sim 0.''8$). The extremely long exposure time is required, given the need for moderate/high signal-to-noise spectra when fitting Balmer lines in order to derive white dwarf masses (Bergeron, Saumon & Wesemael 1995). All of our white dwarf candidates in this field are quite faint, between $V = 22.5$–23.5. Figure 4.3 shows the gain that we achieve by signal averaging multiple exposures. The top panel shows a 1 hour exposure of a $V = 22.5$ white dwarf, whereas the bottom panel shows the same object after averaging 22 1-hour exposures. The H_β, H_γ, and H_δ absorption lines can be clearly seen in the final spectrum.

Gemini Spectroscopic Data Reduction

The raw data frames were obtained from *Gemini* in multi-extention FITS (MEF) format. We reduced the data using the *Gemini* IRAF Package, version 1.3. There are several steps
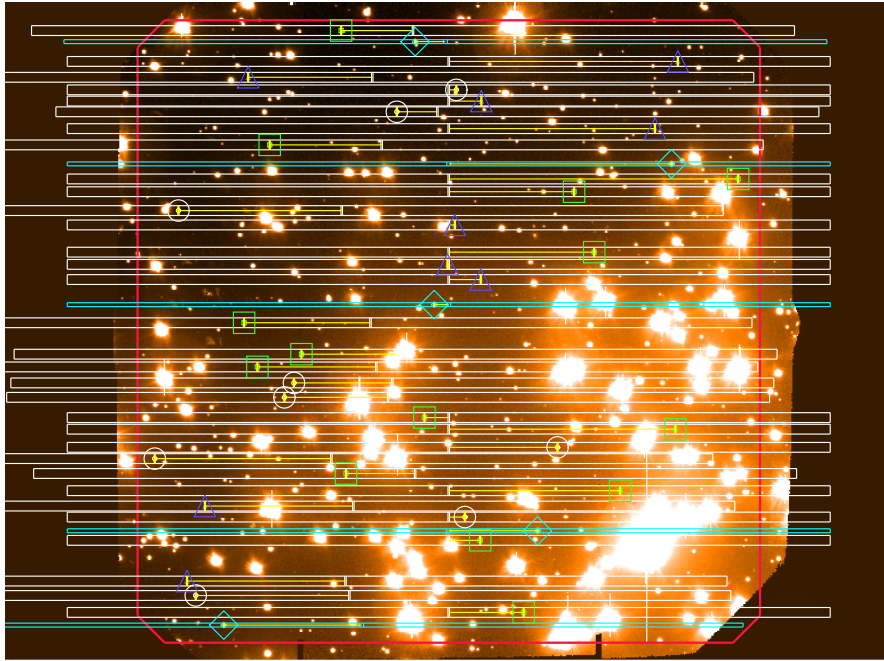
Figure 4.2: The locations of the 32 objects for which we simultaneously obtained spectra
in NGC 2099. The locations of the stars are indicated by small vertical lines
in the centers of each symbol. The horizontal rectangles show the locations
of the dispersed spectra for each object. Eight of the nine blue triangles are
our strong white dwarf candidates, with one more marginal object (based on
the location in the CMD). Other objects, such as faint M-type main-sequence
stars are also shown with different symbols. The five blue diamonds represent
acquisition objects.

involved in producing the final wavelength and flux calibrated, combined spectra. First,
the CCD is composed of three separate chips, and therefore the dispersed spectra will
contain gaps corresponding to the gaps between the chips. To avoid a gap falling on a
Balmer line and rendering the spectrum useless, we chose to obtain the spectrum at two
different grating offsets. The central wavelength was shifted from the default value of
4620 Å to 4720 Å for half the exposures. These two sets of spectra are handled separately
until the very last step of combining the data.

Before proceeding with any of the *Gemini* tasks, we first prepared the data for subse-
quent tasks. We used the GPREPARE.CL task to attach the Mask Definition File (MDF) as
a binary attachment to each science and calibration frame, and updated certain keywords
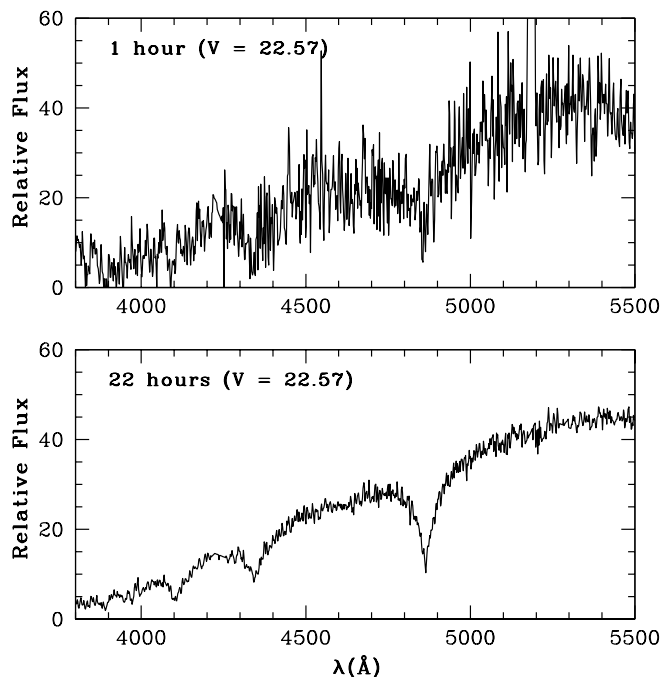
Figure 4.3: The top panel shows a 1-hour exposure of one of our brighter white dwarfs, whereas the bottom panel shows the same spectra after averaging 22 1-hour exposures. By increasing the signal-to-noise, we can clearly see the broad hydrogen Balmer absorption lines of this white dwarf. These spectra have not been flux calibrated.

in the headers of the frames, such as those for gain and read noise. Next we produced a master bias frame, using the GBIAS.CL task, by averaging together 34 individual bias frames taken during the run. Three bias frames were removed due to abnormal features. For the flat-fielding, we averaged together 13 individual flats for the data centred at 4260 Å, and 10 frames for the 4720 Å data, to create two normalized spectroscopic MOS flats. A few saturated and too low signal-to-noise frames were rejected from this procedure. The master bias frame was subtracted from each flat field frame during the averaging.

The master bias image and appropriate flats were applied to the science data using the GSREDUCE.CL task. This task completed several functions, including trimming the overscan region, subtracting the bias frame, cleaning the image for cosmic rays, applying the flat field correction, mosaicing the three chips together, interpolating the pixels within each chip gap, and cutting the MOS slits into separate spectra. This task required a lot of user interaction for several reasons. First, we found post facto that that the spectral extraction routines require very good cosmic ray rejection or else the extracted aperture

will miss the star in the centre of the slit. Residual spikes were abundant in our final spectra due to cosmic rays. We therefore used trial and error to optimize the σ clipping threshold in the cosmic ray rejection task, GSCRREJ.CL . Our chosen threshold, 6-σ, was sensitive enough to remove most of the cosmic ray hits on our long 3600 second exposures, while at the same time, too high to remove any signal from the faint white dwarfs. We modified the cut for the slits that did not contain very faint stars. A second reason that the GSREDUCE.CL task was rerun many times was due to the failure of the automatic spectra cutting routine. Ideally, the Mask Definition File along with a specific parameter file for our grating would dictate the correct locations of the slits on the MOS. However, as reported by others, this task does not yet work consistently. We therefore manually adjusted the parameter file to find the right offset (ranging from 85 to 108 pixels from the default) so that each slit was cut at the correct position. Furthermore, we found that individual exposures required different offsets which all had to be determined. The final flat-fields had to be recreated for each offset as dictated by the science frames, to ensure the correct pixel-to-pixel variations were mapped onto the CCD. With 32 slits on each mask, 22 science exposures, and multiple grating offsets on each frame, this process ended up being very time-intensive. These issues have since been addressed in the latest *Gemini* releases (version 1.6, for example).

For the wavelength calibration, we obtained multiple spectroscopic frames from a CuAr lamp exposure. The automatic wavelength fitting routine in the GSWAVELENGTH.CL task were not available at this time and so the calibration was done interactively. In the end, the residuals in the fit to the emission lines were all well behaved, typically at the 0.4 Å level. With this template, we next used the GSTRANSFORM.CL task to apply the wavelength calibration to the science frames.

The sky subtraction was completed with the GSSKYSUB.CL task. For the white dwarfs, we included the central 1″ of each slit for the signal, and estimated the sky from 80% of the remaining pixels around the star. This gave us 6 pixels for the star, and 11 pixels both above and below the star for the sky estimation (the stars are centred in the slits). There are only 37 spatial pixels due to our factor of two binning in this direction. A number of pixels at both the top and bottom of each slit were discarded. Despite the improved cosmic ray rejection, we manually extracted each of the spectra into a 1D format using the GSEXTRACT.CL task. The automated routines were successful for most slits, but occasionally failed due to the detection of a residual cosmic ray that had not been cleaned earlier. The resulting manually extracted spectra were all combined in a weighted average based on the signal-to-noise of each spectra. A few remaining residual sky lines and small spikes from poor interpolation over the chip gaps were removed simply by cutting out the features manually. None of these features landed near absorption lines.

The final combined spectra were flux calibrated by using the spectrophotometric standard star, HZ 14. This DA white dwarf is located nearby and is very bright. We obtained a 20 second exposure of the star using the same set-up as for the science frames, and then used the standard IRAF calibrate task to flux calibrate and extinction correct the science frames.

4.3.2 Keck Data

As mentioned earlier, we also obtained multi-object spectroscopy of white dwarfs in NGC 2099 using the *Keck* telescope. These data were reduced at UCLA by Dr. David Reitzel using the standard AUTOSLIT (version 3.0) package. First, three fields were imaged to provide ($5' \times 7'$ each) accurate astrometry. Slit masks were constructed for each field based on the positions of the white dwarfs. Two of these fields were spectroscopically observed for 8000s each.

Given the increased sensitivity of LRIS in the blue, the *Keck* data showed better defined, higher-order Balmer lines. These lines are the first ones to be destroyed in higher mass white dwarfs because of perturbations that atoms feel from neighbouring atoms, and are therefore more sensitive to mass (see §4.6.1). So, despite the lower signal-to-noise in the *Keck* spectra, we are still able to accurately measure masses from these data given that we measure more absorption lines (see §4.6.2).

Given the scheduling on the telescope, both fields were observed in one night. The cluster was low on the horizon during the end of the observing run, causing some problems with the data in the second Keck field. Flux, at the blue end of the slit, was lost in these spectra due to atmospheric dispersion. As we discuss later, we do not believe that this affects fitting of the spectral lines in these white dwarfs. Two of the objects in this field are in common with the *Gemini* white dwarfs, and therefore we can directly test whether the missing flux has any effect on the masses.

The total area observed in the three spectroscopic fields (one from Gemini and two from Keck) was 100 square arcminutes, whereas the total extent of the cluster is at least 700 square arcminutes, based on our derivation of radial star counts (Kalirai et al. 2001c). Two of the fields are located very close to the cluster center, with one further out. There is a very small amount of overlap between two of the fields. However, given the careful positioning of the fields, we include over 34% of the white dwarfs in the cluster field (cluster and field stars). This is therefore the biggest star cluster white dwarf sample that has been spectroscopically acquired.

Table 4.1 summarizes the *Gemini* and *Keck* science observations of NGC 2099.

Dates	ID	α_{J2000}	δ_{J2000}	Telescope	Type	Filter	Exp. Time (s)	Airmass
2002-11-02	*Gemini* Field 1	05:52:31.7	32:37:55.0	*Gemini North*	Imaging	g'	4×300	1.038
2002-11-02	*Gemini* Field 1	05:52:31.7	32:37:55.0	*Gemini North*	Imaging	r'	4×300	1.068
2002-11-02	*Gemini* Field 2	05:52:26.1	32:31:11.3	*Gemini North*	Imaging	g'	4×300	1.122
2002-11-03	*Gemini* Field 2	05:52:26.1	32:31:11.3	*Gemini North*	Imaging	r'	4×300	1.071
2002-11-03	*Gemini* Field 3	05:51:58.6	32:37:02.2	*Gemini North*	Imaging	g'	4×300	1.069
2002-11-03	*Gemini* Field 3	05:51:58.6	32:37:02.2	*Gemini North*	Imaging	r'	4×300	1.115
2002-11-30 – 2002-12-09	*Gemini* Field 2	05:52:26.1	32:31:11.3	*Gemini North*	Spectroscopy	open	22×3600	1.239
2001-08-19	*Keck* Field 1	05:52:16.1	32:37:09	*Keck* I	Imaging	B	1×200	1.498
2001-08-19	*Keck* Field 1	05:52:16.1	32:37:09	*Keck* I	Imaging	V	1×200	1.498
2001-08-19	*Keck* Field 1	05:52:16.1	32:37:09	*Keck* I	Imaging	B	1×100	1.463
2001-08-19	*Keck* Field 1	05:52:16.1	32:37:09	*Keck* I	Imaging	V	1×100	1.463
2001-08-19	*Keck* Field 2	05:52:19.4	32:27:25	*Keck* I	Imaging	B	1×300	1.439
2001-08-19	*Keck* Field 2	05:52:19.4	32:27:25	*Keck* I	Imaging	V	1×300	1.439
2001-08-19	*Keck* Field 3	05:52:56.4	32:33:02	*Keck* I	Imaging	B	1×200	1.402
2001-08-19	*Keck* Field 3	05:52:56.4	32:33:02	*Keck* I	Imaging	V	1×200	1.402
2002-12-04	*Keck* Field 1	05:52:14.7	32:38:10	*Keck* I	Spectroscopy	open	4×2000	1.056
2002-12-04	*Keck* Field 2	05:52:17.5	32:28:11	*Keck* I	Spectroscopy	open	4×2000	1.299

Table 4.1: Summary of imaging and spectroscopic observations of NGC 2099

4.4 NGC 2099

In Kalirai et al. 2001c, we investigated several properties of this cluster. By assuming the metallicity of the stars to be similar to the solar value ($Z \sim 0.02$), we determined the distance to be $(m-M)_V = 11.65 \pm 0.13$ and the reddening to be $E(B-V) = 0.23 \pm 0.03$. These values were both found simultaneously, based on a best fit to the Hyades fiducial, after making a slight correction for the small metallicity difference between the clusters. To allow a slightly better isochrone fit, we adjusted the reddening to $E(B-V) = 0.21$ and redetermined the distance to be $(m-M)_V = 11.55$ (~ 1.5 kpc). The resulting cluster age, based on an excellent fit of the new Ventura et al. (1998) stellar evolution models, was determined to be 520 Myrs.

Recently, there has been an in-depth study of both the reddening and metallicity of NGC 2099. Deliyannis et al. (2004, private communication) use five colour photometry of NGC 2099 and find that the reddening of the cluster is $E(B-V) = 0.23 \pm 0.01$. Furthermore, they spectroscopically determine the metallicity of the cluster to be less than solar, $Z \simeq 0.011 \pm 0.001$. Prior to their work, no spectroscopically determined metallicity measurement had been acquired. Given these latest results, we re-derive the age of NGC 2099 using the correct reddening and metallicity. This will prove to be a key step in determining the white dwarf initial-final mass relationship (§4.6.2).

Figure 4.4 shows the very good agreement of the main sequence of NGC 2099 with the main sequence of the Hyades star cluster. The Hyades metallicity is known to be $Z = 0.024$ (Perryman et al. 1998). In Figure 4.4 we have adjusted the NGC 2099 main-sequence redder by 0.09 to account for the new $\Delta Z = 0.14$ between the two clusters, and used the new reddening estimate of $E(B-V) = 0.23$. The resulting best fit distance is found to be $(m-M)_V = 11.5$, larger than the Deliyannis et al. (2004, private communication) value of $(m-M)_V = 11.22 \pm 0.12$. The latter was derived by comparing the observed main-sequence to theoretical models. Other values, summarized in Table 4 of Sarajedini et al. (2004), are in excellent agreement with our estimate, typically deviating by less than 0.10 in $(m-M)_V$.

Using the Ventura et al. (1998) models, the new age of NGC 2099 is found to be 650 Myrs. Our age is larger than the 530 Myrs value found by Deliyannis et al. (2004, private communication) who used the Yale-Yonsei isochrones (Yi et al. 2001). We have experimented with both of the Yale-Yonsei isochrones and those from the Padova group Girardi et al. (2000), and determined best fit ages of 630 Myrs and 620 Myrs, respectively. These are in good agreement with the age from the Ventura et al. (1998) models and therefore we conclude that there must be differences in the data between our photometry and the Deliyannis et al. (2004, private communication) photometry rather than just
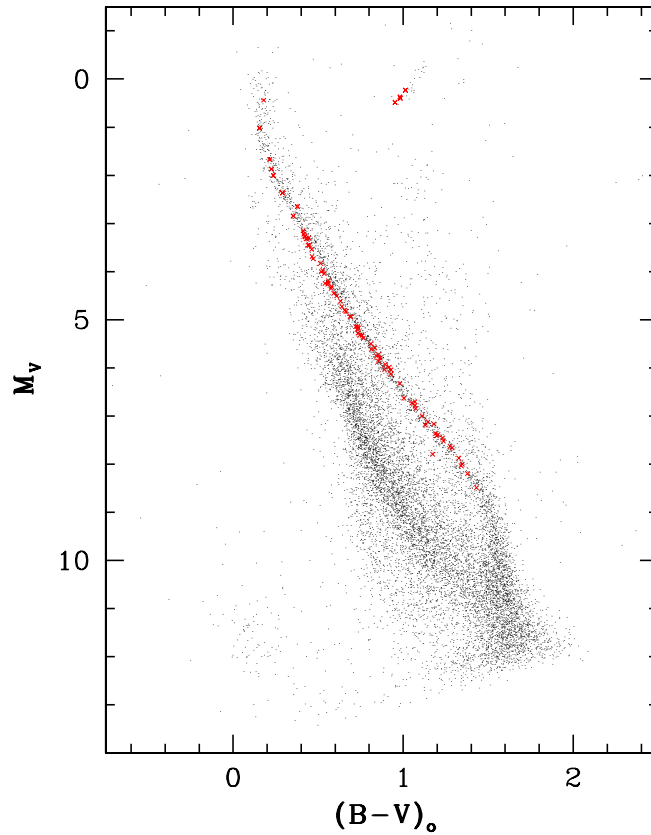
Figure 4.4: The location of the NGC 2099 main sequence is shown with respect to the Hyades cluster members (red dots). The NGC 2099 data set has been adjusted by $E(B-V) = 0.23$ and $(m-M)_V = 11.5$, as discussed in the text.

differences in the modelling. Although we trust our work, we quantify what the effect on the white dwarf initial-final mass relation is from this age discrepency in §4.7. Given this age, the turn-off mass of NGC 2099 is 2.4 $M_\odot$, and so we would expect most of our white dwarfs to have an initial mass close to (but larger than) this value to reflect those stars which have evolved off the main sequence. We do not expect many white dwarfs that came from very massive progenitors (6–8 $M_\odot$) since the IMF of the cluster dictates that only a small number of stars with those masses would have been produced (see Kalirai et al. 2001c for the present day mass function of the cluster).

In Figure 4.5 we zoom in to the faint-blue end of the CMD of NGC 2099. All objects are shown with crosses. We also overlay model white dwarf cooling sequences with masses

ranging from 0.5–1.1 $M_\odot$ in blue (Wood 1995). Clearly, there are a large number of white dwarf candidates in this cluster. However, a number of these objects could also be field white dwarfs, binaries, or even other extragalactic objects such as faint-blue galaxies, compact galaxies, or QSOs. We select objects from the region approximately bounded by the cooling curves in an unbiased way for the spectroscopic sample in this study. The objects which we believe are white dwarfs, and for which we have obtained spectroscopy, are shown as dark squares (*Gemini*) and dark circles (*Keck*). In total, there are nine *Gemini* objects, one of which is outside the bounds of the diagram. The latter object was assigned a lower priority and included only because there was an available slit which didn't interfere with other objects. This leaves eight strong white dwarf candidates. For the *Keck* candidates, there are 22 objects on this diagram for which we obtained spectroscopy (dark circles). A few of these objects sit very close to each other on the CMD and it is difficult to separate the dots. Additionally, three of these objects overlap with the *Gemini* objects and so are shown as dark squares (the circles are plotted first and are therefore covered up). These are the objects with $V = 23.26$ and $B - V = 0.35$, $V = 22.70$ and $B - V = 0.226$, and $V = 22.57$ and $B - V = 0.41$. We can also definitely eliminate two other objects (with $V = 24.49$ and $B - V = 0.07$ and $V = 21.66$ and $B - V = 0.42$) as cluster white dwarf candidates given that they are clear outliers from the location of the white dwarf clump in NGC 2099. Two further objects (with $V = 23.76$ and $B - V = 0.47$ and $V = 24.14$ and $B - V = 0.50$) will be classified as marginal candidates, as they sit 0.5 magnitudes fainter than the termination of the white dwarf cooling sequence (Kalirai et al. 2001c). In fact, the confirmation of a non-white dwarf nature for these two objects is very important in defining the end of the cooling sequence. In §4.6.2 we will plot white dwarf isochrones along with those stars which are confirmed white dwarfs. A final object which is common between the *Gemini* and *Keck* studies ($V = 22.57$ and $B - V = 0.40$) appears to be too undermassive for a cluster white dwarf, as it sits brighter than the 0.5 $M_\odot$ cooling sequence. However, it is close enough that we will call it a white dwarf candidate. Therefore, in total 18 of the 22 *Keck* objects will be referred to as strong white dwarf candidates. A large fraction of these clump near the 0.8 $M_\odot$ white dwarf cooling sequence, suggesting that this young cluster will provide a population of massive white dwarfs.

Without proper motion separation it is difficult to determine which objects in the NGC 2099 CMD are cluster members and which are Galactic disk members. NGC 2099 has a Galactic longitude of 178 degrees and therefore the motions of stars along this line of sight are almost entirely in the transverse direction. The radial velocity variations of the cluster with respect to the disk stars are too small to separate out the cluster members. We can, however, statistically estimate the number of stars in the foreground/background
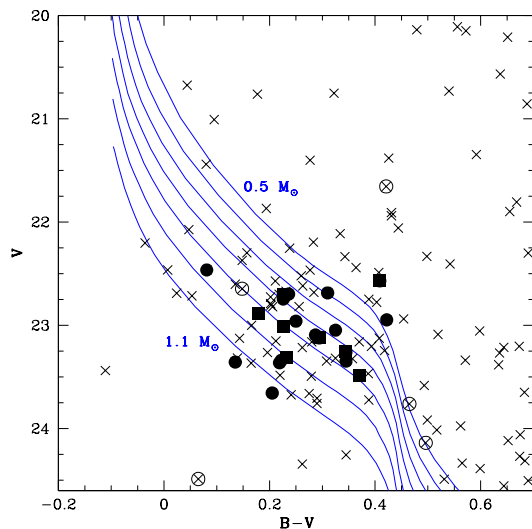
Figure 4.5: A zoom in of the faint-blue end of the CMD of NGC 2099 is shown. The crosses mark all objects in the CMD. The model sequences represent white dwarf cooling models (Wood 1995) at increments of 0.1 $M_\odot$, with 0.5 $M_\odot$ at the top and 1.1 $M_\odot$ at the bottom. A large number of strong white dwarf candidates clearly exist in the cluster. The candidates for which we have obtained spectroscopy are shown as dark circles (*Keck*) and dark squares (*Gemini*). The five objects shown as open circles with crosses inside will be discussed in section 4.5. A number of candidates appear to follow closely the 0.8 $M_\odot$ white dwarf cooling sequence. White dwarf isochrones will be shown later.

by using our blank field from the *CFHT* study (Kalirai et al. 2001c). Counting the number of objects at the faint-blue end of the CMD of the blank field gives 17 objects, which scales up to 23 after multiplying by the small difference in area between the two fields. The total number of objects in the cluster field faint-blue end CMD is 71, suggesting that $\sim 30\%$ of our objects may be field contamination. Since we know the distance to NGC 2099, we may be able to identify these objects by comparing the theoretical luminosity from fitting the spectra to the observational magnitudes. A field object would clearly have discrepent absolute magnitude as we would have applied the wrong distance modulus to it. Binary stars can also be found by looking for overluminous objects (see §4.6.3).
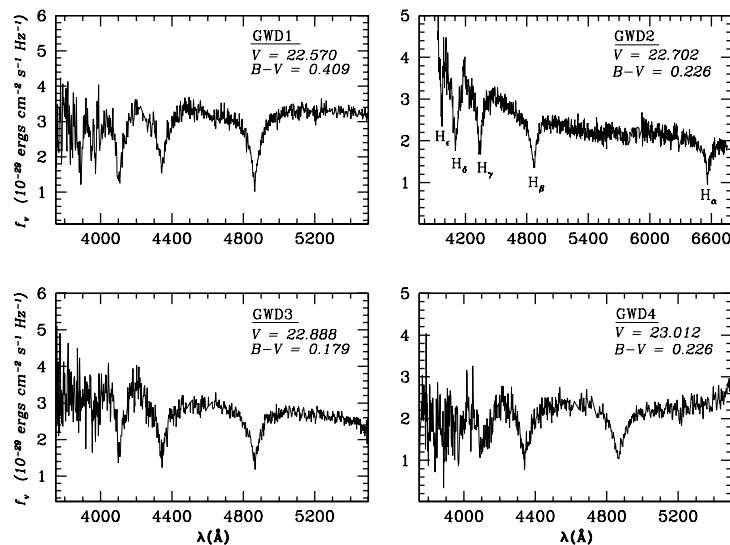
Figure 4.6: Spectra of the four brightest objects in the *Gemini* field are shown. All four objects show broad hydrogen Balmer absorption lines, indicating DA white dwarf classification. Although the spectral coverage for most stars extends from H_β (4861 Å) to H_δ (4102 Å), one star, GWD2 shows H_α (6563 Å), H_β (4861 Å), H_γ (4341 Å), H_δ (4102 Å), and H_ϵ (3970 Å) absorption lines. We indicate the locations of these lines for this star only in the top-right panel.

4.5 Spectroscopic Observations of White Dwarfs

As mentioned in §4.3.1, our best *Gemini* GMOS $5.'5 \times 5.'5$ field contained 32 slits in which 8 stars were believed to be potential white dwarfs. As Figures 4.6 and 4.7 show, all 8 of our candidates are in fact confirmed white dwarfs. This is a remarkable result, given, that our selection for these objects was entirely unbiassed and only used the *CFHT* photometry and image classification. In other open clusters, such as M67, the yield of objects which were believed to be white dwarfs and those that were spectroscopically confirmed is quite low, at least at the bright end. Bolte et al. (2002, private communication) found that most of the objects at the top of the putative white dwarf cooling sequence identified in Richer et al. (1998) are in fact extragalactic.
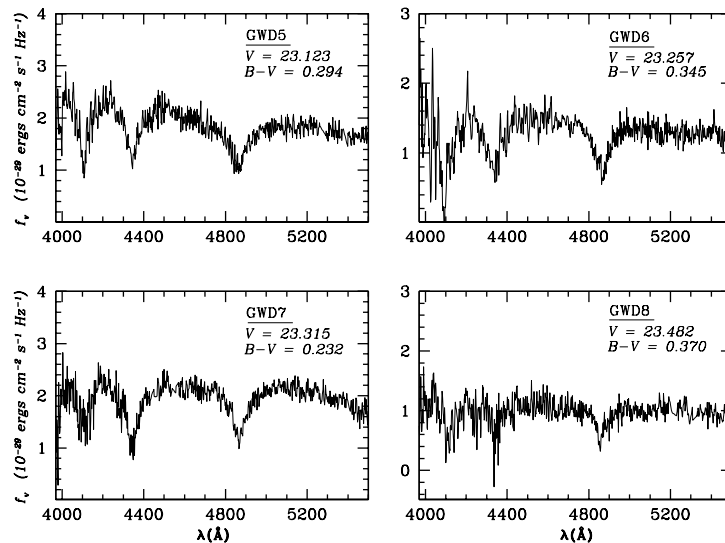
Figure 4.7: *Gemini* spectra of four of the fainter objects in NGC 2099 also indicate DA white dwarf classification.

In Figures 4.8, 4.9, and 4.10 we present the spectra for 17 confirmed white dwarfs from the two spectroscopic *Keck* LRIS fields in NGC 2099. The number of objects that were believed to be white dwarfs in the *Keck* fields was 18, again an excellent ratio of positive detections. Two more *Keck* objects were classified as marginal candidates, as they sit 0.5 magnitudes fainter than the termination of the white dwarf cooling sequence, and are found not to be white dwarfs. These, as well as the other objects which are confirmed not to be white dwarfs, are shown as open circles in Figure 4.5. Three of the objects are in common between the *Gemini* and *Keck* data sets. These multiple measurements will provide an additional constraint on our spectroscopic errors, as well as indicate whether the missing flux in the field 2 *Keck* data has any effect on our measured masses. All spectra have been arranged from brightest to faintest, within each group. The designation for these stars is such that we refer to objects in field 1 of Keck as K1– and objects in field 2 as K2–. It should be mentioned that these spectra are unprecedented in terms of quality given the faintness of the objects. All of the stars presented here have $V > 22.4$, a remarkable depth and huge improvement over previous efforts, which have mostly been
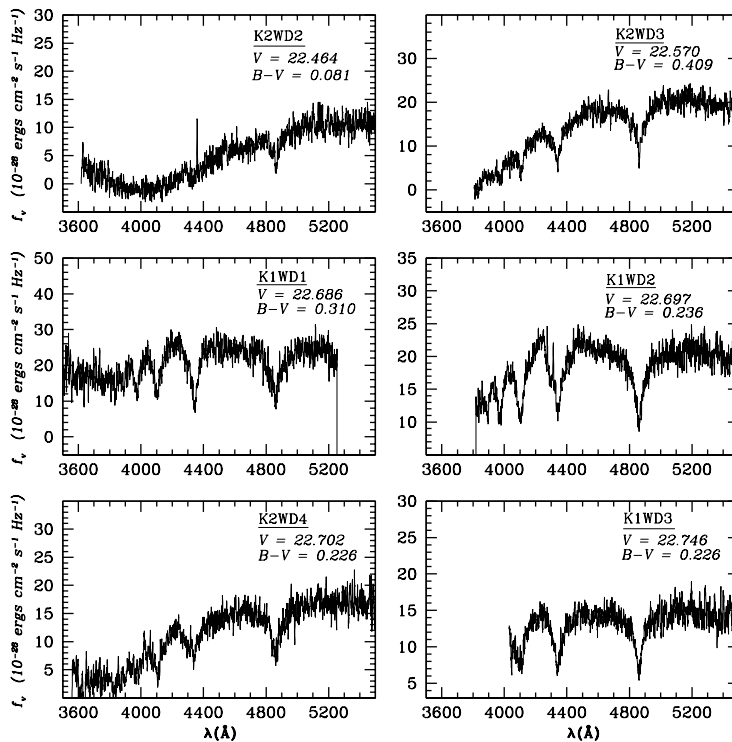
Figure 4.8: Spectra of the six brightest objects in the *Keck* fields are shown. All six objects are confirmed to be DA white dwarfs. Notice the higher sensitivity in the blue of the *Keck* LRIS detector and the higher resolution of the spectra. The object in the top-right panel, K2WD3, is the same star shown as GWD1 in Figure 4.6 (top-left). The object in the bottom-left panel, K2WD4, is the same star shown as GWD2 in Figure 4.6 (top-right). Notice the missing flux in both of the *Keck* field 2 spectra for these objects, as discussed in §4.3.2.

limited to objects 2–3 magnitudes brighter.

An interesting result from the spectra in Figure 4.11 (which displays all of the spectra in one panel) is that all of the white dwarfs are spectral type DA. The distribution of DA vs non-DA in the field is marginally constrained as a function of temperature, but not very well as a function of mass. For example, Kleinman et al. (2004) shows the distributions of several hundred DAs and DBs from Sloan and find a peak for DAs at $\sim$ 10,000 K, and $\sim$ 16,000 K for DBs, both with a tail to higher temperatures. Therefore our sample of white dwarfs should be sensitive to both DAs and DBs. In the field, about 80% of all white dwarfs are DA spectral type, over all masses. However, the field distributions as a function of mass are not well constrained. For DAs, there is believed to be two peaks, one
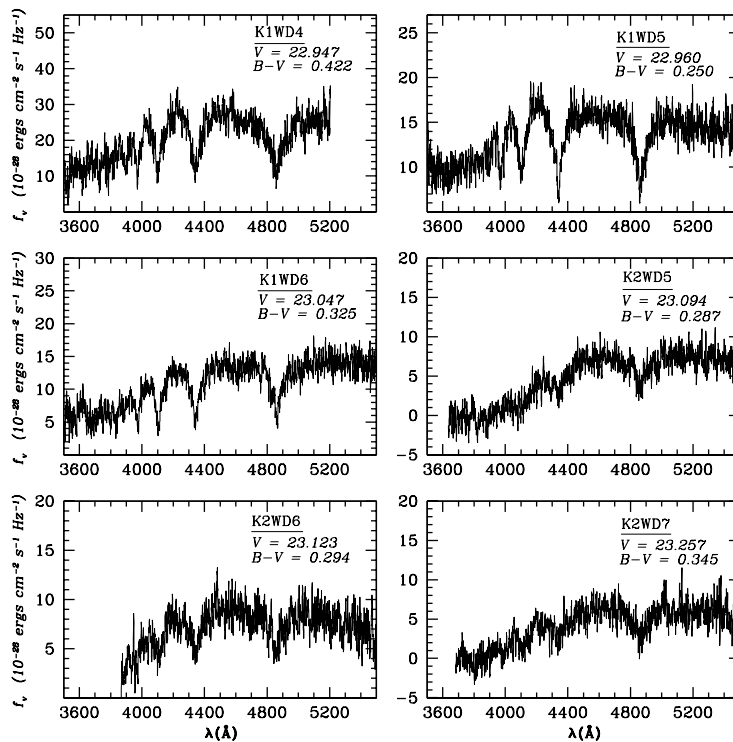
Figure 4.9: Spectra of six more DA white dwarfs in the *Keck* fields are shown. The object in the bottom-right panel, K2WD7, is the same star shown as GWD6 in Figure 4.7 (top-right).

near 0.6 $M_\odot$ and a smaller one at higher masses near 1.0 $M_\odot$. The distribution of DBs is based on a very small number of stars and does not show many massive objects (Bergeron, Leggett, & Ruiz 2001). Our work represents the first large open star cluster sample of spectroscopically determined white dwarfs, and possibly suggests that the DA/DB ratio may be different in clusters than the field. Previous efforts have only found a few white dwarfs at most, and were, therefore not statistically significant in saying anything about the DA/DB dichotomy. With an 80% DA/DB white dwarf ratio, we would expect four of our objects to be DB. None were found, the chances of which are statistically not likely (less than 1.8% probability in a Poisson distribution). Of course, the ratio of DAs to DBs may in fact be higher than 80% for these masses (0.8 $M_\odot$). This could suggest that convecting mixing of the subsurface helium layer with the surface hydrogen layer is inhibited in massive white dwarfs. Alternatively, the cluster environment may play a role in producing hydrogen dominated white dwarfs, for example through accretion of gas in the inter-cluster medium.
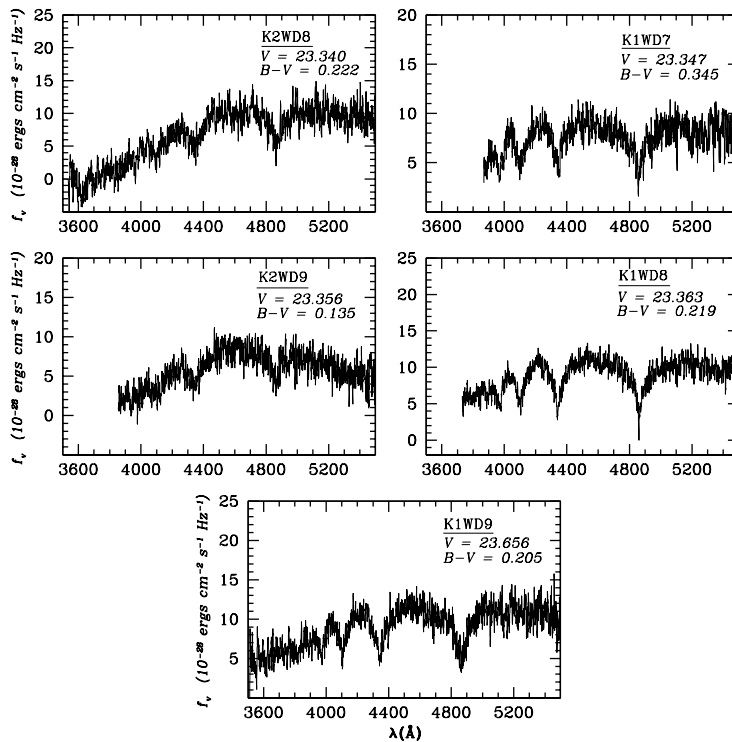
Figure 4.10: Spectra of the five faintest white dwarfs in the *Keck* fields are shown. Notice the higher quality of the field 1 spectra compared with field 2 (discussed in text).

As stated in the Figure captions, the three white dwarfs which are common between the *Gemini* and *Keck* observations are GWD1 and K2WD3, GWD2 and K2WD4, and GWD6 and K2WD7. Both GWD1 and GWD2 are well measured in the *Gemini* data and should yield accurate masses. For GWD6 on the other hand, only two Balmer lines can be used to derive masses due to the redder spectral coverage of this star (see §4.3.1). In the *Keck* data, both K2WD3 and K2WD4 are well measured and show 3–4 absorption lines each. K2WD7, on the other hand, is a very low signal-to-noise object for which it will be difficult to obtain masses from spectral line fitting. For each of these three white dwarfs, the *Keck* spectra are from field 2 and therefore show signs of missing flux in the blue (see §4.3.2). A comparison between the masses of the white dwarfs from these *Keck* spectra (at least for the brighter two objects) and the *Gemini* spectra should confirm whether the missing flux has any effect on the derived mass given our fitting technique (described in §4.6.1).

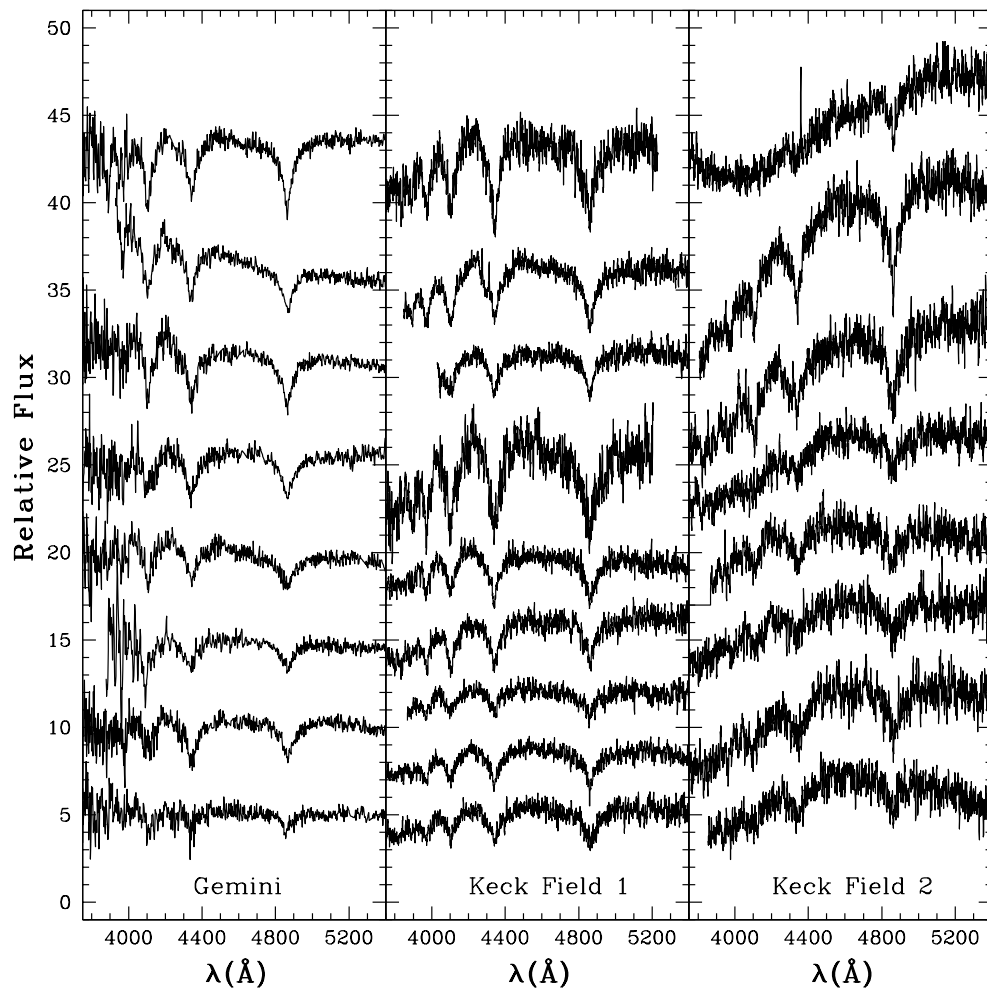Table 4.2 summarizes observational parameters for all of the white dwarfs in this study.

Figure 4.11: Spectra of all white dwarfs are shown.

Star	α_{J2000}	δ_{J2000}	V	σ_V	$B - \text{V}$	σ_{B-V}
GWD1	05:52:26.80	32:30:46.7	22.57	0.02	0.41	0.03
GWD2	05:52:17.54	32:29:03.4	22.70	0.02	0.23	0.03
GWD3	05:52:36.26	32:32:51.5	22.89	0.03	0.18	0.04
GWD4	05:52:34.53	32:29:12.4	23.01	0.03	0.23	0.04
GWD5	05:52:25.11	32:30:55.7	23.12	0.03	0.29	0.04
GWD6	05:52:18.08	32:29:38.4	23.26	0.04	0.35	0.05
GWD7	05:52:18.44	32:29:37.6	23.32	0.04	0.23	0.05
GWD8	05:52:26.16	32:30:27.8	23.48	0.04	0.37	0.06
K2WD2	05:52:13.32	32:28:55.9	22.46	0.02	0.08	0.03
K2WD3	05:52:26.80	32:30:46.7	22.57	0.02	0.41	0.03
K1WD1	05:52:25.14	32:40:03.6	22.69	0.02	0.31	0.03
K1WD2	05:52:25.82	32:36:03.8	22.70	0.02	0.24	0.03
K2WD4	05:52:17.54	32:29:03.4	22.70	0.02	0.23	0.03
K1WD3	05:52:26.57	32:35:25.4	22.75	0.02	0.23	0.03
K1WD4	05:52:11.96	32:40:39.5	22.95	0.03	0.42	0.04
K1WD5	05:52:16.21	32:38:18.5	22.96	0.03	0.25	0.04
K1WD6	05:52:06.43	32:38:29.4	23.05	0.03	0.33	0.05
K2WD5	05:52:26.42	32:30:04.3	23.09	0.03	0.29	0.04
K2WD6	05:52:25.46	32:30:54.4	23.12	0.03	0.29	0.04
K2WD7	05:52:18.44	32:29:37.6	23.26	0.04	0.35	0.05
K2WD8	05:52:25.34	32:29:35.2	23.34	0.04	0.22	0.05
K1WD7	05:52:27.42	32:35:50.0	23.35	0.04	0.35	0.06
K2WD9	05:52:12.88	32:29:50.0	23.36	0.04	0.14	0.05
K1WD8	05:52:22.89	32:36:29.4	23.36	0.04	0.22	0.05
K1WD9	05:52:29.29	32:37:06.7	23.66	0.05	0.21	0.07

Table 4.2: Observational parameters of white dwarfs

4.6 Determining Masses of White Dwarfs

The mass distribution of white dwarfs in the Galactic disk is of fundamental importance. Bergeron, Saffer, & Liebert (1992) remark that the complete history of star formation in the disk could be reconstructed with a good understanding of the mass distribution of white dwarfs, their luminosity function, and the initial-final mass relationship. Although there are previous constraints (see Leggett, Ruiz, & Bergeron 1998 or Bergeron, Saffer, & Liebert 1992) and impressive new results from the Sloan Digital Sky Survey (Madej, Nalezyty, & Althaus 2004) on both the mass distribution and luminosity function of white dwarfs, the initial-final mass relationship is still very poorly understood (see §4.2).

Several methods have been used to determine the masses of white dwarfs, both in the field and in open star clusters. If members of a binary system and with sufficient information, Kepler's Laws directly yield the masses of the components from the orbital solution. This method is only applicable to a few systems in wide binary orbits where no mass exchange has occurred. For those white dwarfs which pulsate, asteroseismology can directly yield masses through pulsation mode analysis and the effect of large surface gravities on pulsation eigenfunctions (see e.g., Winget et al. 1994; Fontaine et al. 1996). As discussed in many papers (such as Kawaler 1991), this approach is most successful for very hot, young white dwarfs. A third method to measure the masses of white dwarfs involves the use of the gravitational redshift. Because of the large gravities of white dwarfs, photons lose energy in escaping the surfaces of these stars. The corresponding shift in the spectrum of the Balmer lines can be measured and used to constrain the mass/radius ratio (see e.g., Bergeron, Liebert, & Fulbright 1995). Theoretical mass-radius relations can directly yield the mass from this ratio (see e.g., Wood 1990). The main drawbacks of the gravitational redshift method is that it requires high resolution, sharp H_α and H_β line cores and a good measurement of the star's intrinsic radial velocity, criteria which are rarely fulfilled. Finally, if the distance to a white dwarf is known, then its radius can also be estimated by using its luminosity and effective temperature. This method requires a minor application of the spectroscopic technique (see §4.6.1). Again, a theoretical mass-radius relationship then directly yields the mass from the radius.

Perhaps the most general and best method for determining white dwarf masses is the full comparison of the observed spectrum to a model prediction. This technique was first discussed in detail and applied by Bergeron, Saffer, & Liebert (1992) and has been refined in the past decade, primarily by Pierre Bergeron. Stellar atmosphere models are used to to estimate both the surface gravity and the effective temperature of the star. The only drawback of this method is that the spectra must have a sufficient signal-to-noise ratio (at least 20, preferably more) for the fitting to yield accurate results. This is especially

the case if only a few Balmer lines are detected. For the present data, we will use the spectroscopic fitting technique to derive masses for all of our higher signal-to-noise objects, and use the distance dependent method for the faintest few objects.

The spectroscopic method has been tested in various papers against independent mass measurements from the other methods above. This is important to evaluate any systematic errors that might exist in measuring masses from fitting white dwarf spectra. For example, Bergeron, Liebert, & Fulbright (1995) compared the masses of 35 DA white dwarfs measured with gravitational redshift determinations to spectroscopic masses and found a very good correlation for all but the coolest stars ($T_{\text{eff}} < 12,000$ K). All but one of our white dwarfs are hotter than this temperature, therefore, indicating that systematic effects from the fitting will be very small. Recent high signal-to-noise measurements of the spectrum of Sirius B, the closest white dwarf, also yield an excellent agreement between the gravitational redshift mass and the spectroscopic mass (M. Barstow 2004, private communication). Comparison of masses derived from white dwarfs with parallax measurements through photometric techniques also agree well with the spectroscopic method (see e.g., Bergeron, Leggett & Ruiz 2001). Finally, photometric fits of white dwarf cooling sequences in open star clusters are in good agreement with spectroscopic mass determinations. NGC 2168 is a good example of this. The cluster white dwarf candidates appear to be massive as shown in §3.6.2. Recent work by Williams et al. (2004) confirms this. They have spectroscopically shown that all six white dwarfs in NGC 2168 are massive. Further evidence of this agreement will be shown for the NGC 2099 white dwarf later.

4.6.1 Spectroscopic Fitting of White Dwarfs

Fitting white dwarf spectra is possible given the extreme sensitivity of the Balmer absorption lines to changes in the surface temperature (T_{eff}) and gravity ($\log g$). The temperature dependence results from the excitation and ionization equilibrium between electrons (Shulz & Wegner 1981). The direct effect of this dependence on the spectrum is for lower temperature stars to possess Balmer lines with deeper cores. Lower temperature stars also show better defined higher order Balmer lines due to higher equivalent widths. This effect, however, peaks for stars with $T_{\text{eff}} = 11000$–15000 K and with $\log g$ between 7.0 and 9.0, while there are smaller equivalent widths for much cooler stars. At very cool temperatures, $T_{\text{eff}} = 6000$ K, the higher order Balmer lines are almost non-existent, due to the destruction of the upper levels of the hydrogen atom by other neutral hydrogen atoms (Bergeron, Wesemael, & Fontaine 1991). The effect due to increasing gravity (and pressure) is to blend the electric fields of neighbouring atoms, thereby splitting the hydrogen spectral lines into a number of components and increasing the number of energy levels that electrons can jump to. This Stark broadening causes stars with higher gravities to

possess a higher electron pressure, and therefore have a stronger line absorption for H_β and H_γ. For higher order Balmer lines (H_δ and higher), the effect of increasing the surface gravity is the opposite. The equivalent widths of these lines decrease with increasing surface gravity due to the destruction of the atomic levels of the hydrogen atom (Bergeron, Saffer, & Liebert 1992). This "quenching" is a result of the perturbations that an atom feels from neighbouring atoms, and is obviously a strong function of increasing pressure (hence gravity). This effect is the primary reason that modelling multiple absorption lines can be a very powerful indicator of the gravity of a star. Other effects on the emergent spectrum, such as from rotation or metallicity, are known to be very small in white dwarfs and can be ignored.

A qualitative look at the effects of changes in T_{eff} and log g on the spectral signature of a white dwarf is shown in Figure 4.12 (taken from Bergeron, Saffer, & Liebert 1992). The three panels show the Balmer lines for three different synthetic spectra with $T_{\text{eff}} = $ 15000 K, 25000 K, and 35000 K. The absorption lines shown are H_β (bottom) to H_9 (top), with each Balmer line shown for five different log g values, 7.0, 7.5, 8.0, 8.5, and 9.0. The log g = 7.0 lines are the dashed lines, with the lines increasing monotonically for the other gravities. It is clear that lower temperature stars (left-panel) have deeper cores than their higher temperature counterparts. Also seen is the inversion of shallower/steeper to steeper/shallower profiles as log g increases, when going from lower order lines such as H_β to the higher order lines (top of panels).

The technique used to fit the stars is described in §3.2 of Bergeron, Saffer, & Liebert (1992). The models and the code were kindly provided to us by Dr. Pierre Bergeron. The actual fitting of the spectra and analysis was carried out by the author under the supervision of Dr. Bergeron.

The first step in the fitting is to normalize the line profiles based on two points on the continuum on either side of the absorption line. The location of these continuum points is derived from first finding a model for the entire spectrum that consists of an arbitrary number of terms. This will include a linear, squared, cubic, and possibly higher order terms plus any number of Lorentzian profiles. Once the position of the continuum is known, the model comparisons are carried out solely based on the line shapes and depths. This approach has the advantage that the results from the fitting will not be affected if the continuum is improperly calibrated, provided that it is smooth and there is no "kink" or slope change at the location of a Balmer line. The actual fitting of the line shapes uses the nonlinear least-squares method of Levenberg-Marquardt (Press et al. 1986). The χ^2 statistic is calculated and minimized for combinations of T_{eff} and log g, using normalized model line profiles of all absorption lines simultaneously. Further details of the fitting procedure are given in Bergeron, Saffer, & Liebert (1992). The errors in T_{eff} and log g are
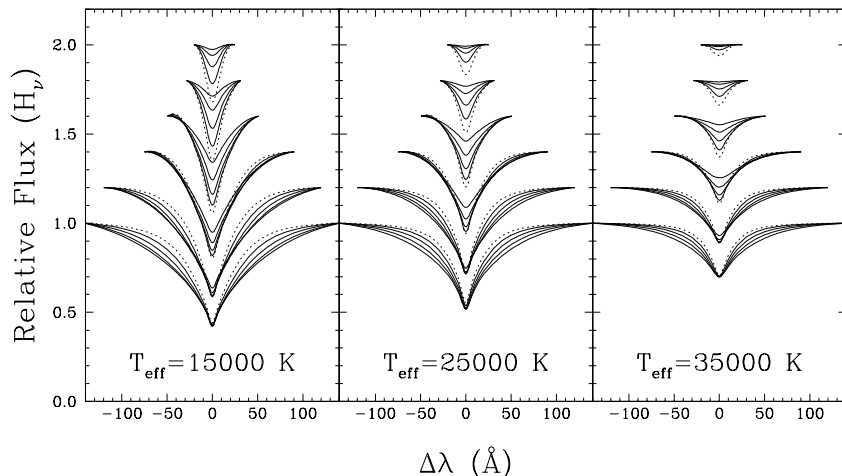
Figure 4.12: Balmer line profiles are shown for synthetic spectra with different T_{eff} and log g values. The absorption lines are H_β (bottom) to H_9 (top), with each Balmer line shown for five different log g values, 7.0 (dashed), 7.5, 8.0, 8.5, and 9.0. See §4.6.1 for a discussion.

very weakly correlated and have been tested using methods that do not minimize the χ^2 statistic. The results indicate that the errors are accurate for spectral fits with data that have are somewhat noisy, such as that presented in this work. For very high signal-to-noise data (S/N > 50), the errors are forced to zero in this method by driving the χ^2 to 1, and are therefore meaningless. We will test these errors using synthetic spectra in §4.6.2.

4.6.2 Results

In Figures 4.13–4.16 we present spectroscopic model fits to our white dwarfs. In total, we are able to fit seven of the eight *Gemini* white dwarfs and twelve of the seventeen *Keck* white dwarfs. The fits for individual white dwarfs are presented in different panels, with multiple absorption lines in each panel. The red lines indicate the normalized atmosphere models, from the simultaneous fits of all absorption lines. Figure 4.13 shows the fits to the four brightest *Gemini* white dwarfs. All of these objects have high signal-to-noise and the resulting fits yield well constrained T_{eff} and log g values. One of three white dwarfs in Figure 4.14, GWD6, contains a fairly noisy spectrum combined with only 2 spectral lines.
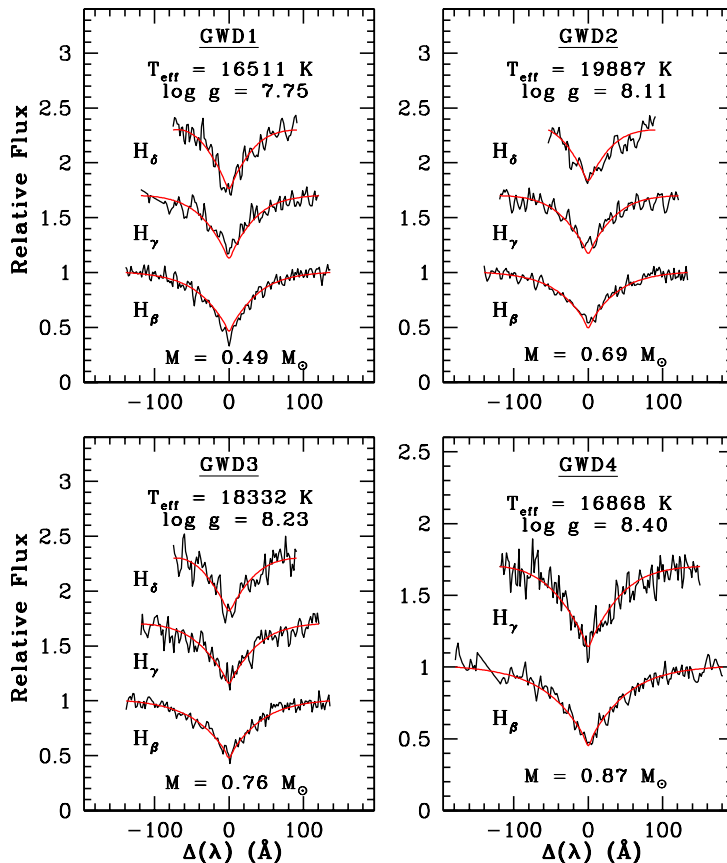
Figure 4.13: The spectroscopic model fits are shown for the four brightest *Gemini* white dwarfs. The best fit values of T_{eff} and log g are also shown along with the masses of the white dwarfs (see §4.6.2).

The resulting T_{eff} and log g values for this object have larger uncertainties than the other objects. The six brightest *Keck* white dwarfs that are fit with masses are shown in Figure 4.15. In general, the higher sensitivity of the *Keck* LRIS detector in the blue allows for higher order Balmer lines to be measured thereby better constraining the parameters for the stars (see e.g., K1WD1) even though the spectra are generally at lower signal-to-noise compared to the Gemini spectra. The resulting uncertainties in the T_{eff} and log g values for these stars are significantly lower than for the *Gemini* objects. We will evaluate the internal uncertainties in the model fits later. The final six objects that we are able to fit in the *Keck* data are shown in Figure 4.16. Again, the measurement of higher order Balmer lines allows accurate T_{eff} and log g values to be determined despite the somewhat lower
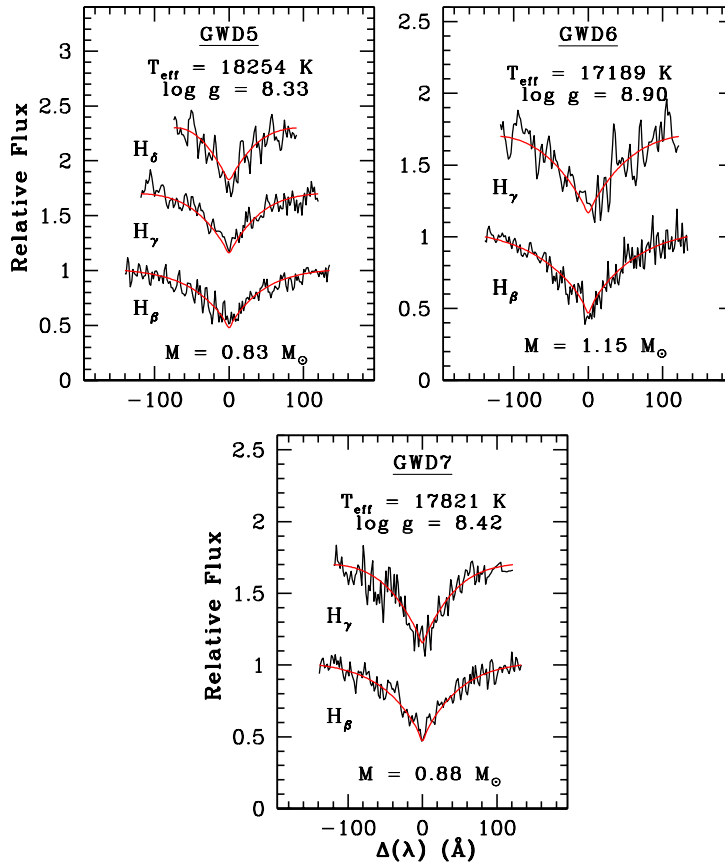
Figure 4.14: The spectroscopic model fits are shown for three of the fainter *Gemini* white
dwarfs.

signal-to-noise (see §4.6.1).

The single *Gemini* white dwarf and five *Keck* white dwarfs that were not fit using
the spectroscopic method suffered from either not having enough signal-to-noise in their
spectra or having an insufficient number of spectral absorption lines. In fact, most of the
objects suffered from a combination of both these effects. As we will show in §4.6.2, we
can still measure the masses of one of these stars using a pseudo-spectroscopic technique
assuming they are members of NGC 2099.

The masses shown at the bottom of the panels in Figures 4.13–4.16 are determined
from coupling the $T_{\rm eff}$ and log g values found above with the white dwarf evolutionary
models of Wood (1995). These models have carbon-core compositions with thick hydrogen
layers of $q({\rm H}) = M_{\rm H}/M = 10^{-4}$ and helium layers of $q({\rm He}) = 10^{-2}$. The masses are found
automatically by interpolating within detailed tables. A quick look at the masses suggests
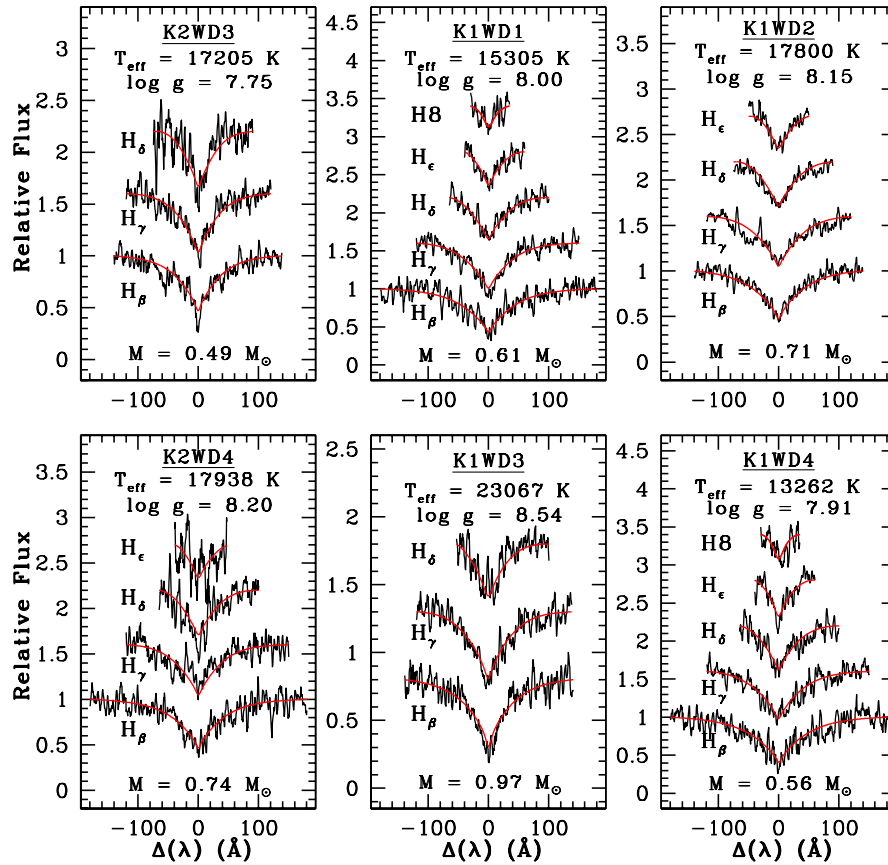
Figure 4.15: The spectroscopic model fits are shown for six of the *Keck* white dwarfs.

that a large fraction of our white dwarfs are in fact quite massive, between 0.7 and 0.8 $M_\odot$, as we predicted in §4.4. As we will see in §4.6.3, there is some evidence that a few of the lower mass white dwarfs are in fact either field objects or overluminous binary white dwarfs. These can be separated by comparing the theoretical luminosities of the objects with the observationally measured luminosities assuming they are cluster members.
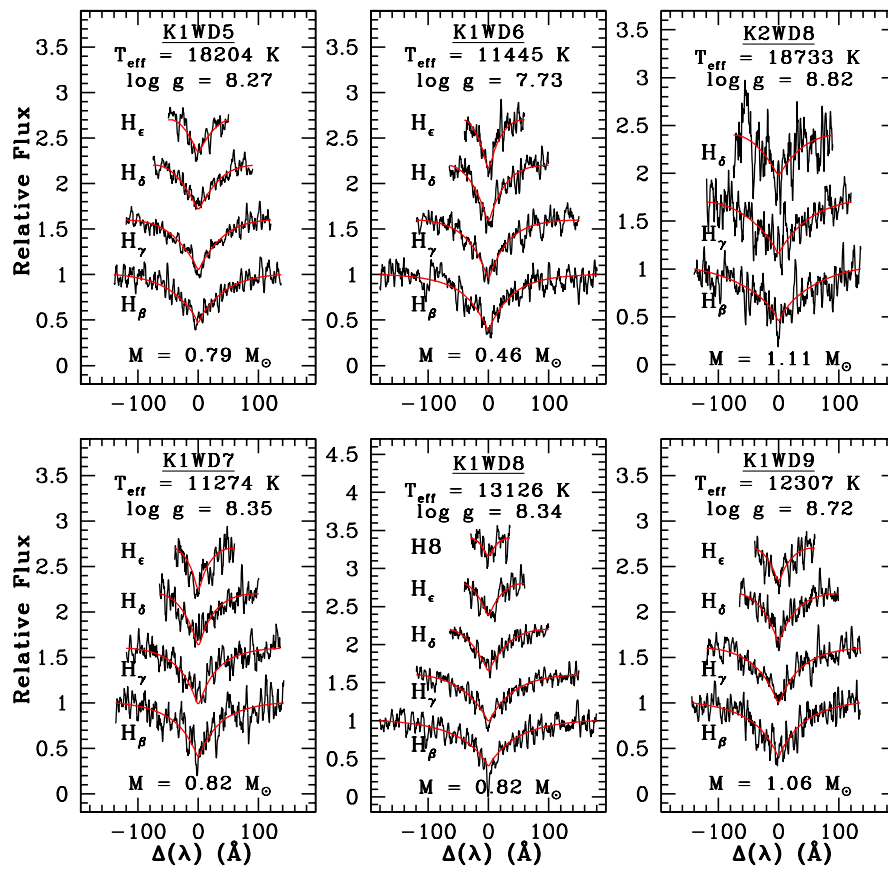
Figure 4.16: The spectroscopic model fits are shown for six of the *Keck* white dwarfs.

Pseudo-spectroscopic Masses

As Figures 4.13–4.16 show, we are able to use the spectroscopic fitting technique for a total of seven of the *Gemini* white dwarfs and 12 of the *Keck* white dwarfs. Two of the objects that are in common between the spectra from two telescopes are fit. For the remaining single *Gemini* white dwarf, and five *Keck* white dwarfs, we will attempt to determine pseudo-spectroscopic masses. This can be done by combining the temperatures of the stars from the spectral fits (which is more reliable than the log g values) with their luminosities, assuming they are cluster members. We must use this approach with caution, however, as these white dwarfs could in fact be field objects (to be discussed later). A temperature and luminosity together give the radius of the star, from which we can derive the mass using the mass-radius relationship (Wood 1995).

The one remaining *Gemini* object, GWD8, has a very large uncertainty (± 7000 K) in its temperature measurement and therefore it is not possible to use the pseudo-spectroscopic technique. An additional *Gemini* object, GWD6, had a somewhat noisy spectrum with only two absorption lines. The best fit mass from Figure 4.14 was found to be quite high, 1.15 $M_\odot$. The theoretical M_V for this star is discrepent with the observed luminosity by 0.82 magnitudes. As the temperature appears well constrained, we use the pseudo-spectroscopic method to rederive the mass of the star assuming it is a cluster member. The result gives a mass of $M = 0.92\ M_\odot$, which we will use rather than the spectroscopic result. For the one other faint *Gemini* object with two Balmer lines, GWD7, we find consistency between this method and the purely spectroscopic one.

Most of the remaining *Keck* objects do not have enough signal-to-noise for reliable temperatures to be estimated. After trying the pseudo-spectroscopic technique, we are only able to recover one star for which we could not measure a spectroscopic mass, K2WD5, for which we measure a final mass of $M = 0.85\ M_\odot$ using this technique.

Since our method for determining masses of these two white dwarfs suffers from not knowing if they are cluster members, we will plot these objects with caution on our initial-final mass relationship. However, we have tested the pseudo-spectroscopic technique by comparing the derived masses of other stars (from both this technique and spectral line fitting) and it confirms that the method does give consistent results.

Using Simulated Spectra to Determine Errors

The spectroscopic fitting technique that we are using to derive masses of white dwarfs directly gives us formal uncertainties in the errors in each of the parameters. These errors are the 1-σ results from the χ^2 fitting described in §4.6.1. We can partially test the reliability of these errors by using simulated spectra of known masses, and seeing what

output masses we derive after propagating them through the spectral fitting routines.

To test these errors, we simulate a large grid of hundreds of synthetic white dwarf spectra for various values of log g and T_{eff}. We add Gaussian noise to these spectra until we achieve a signal-to-noise that is consistent with the data. The resolution is also adjusted to match that in the data. By fitting the synthetic spectra, we can estimate how much the derived parameters, such as mass, change from each fit. Figure 4.17 shows examples of these synthetic spectra for five different signal-to-noise values, 1000, 100, 20, 10, and 5, at 3 Å resolution as in the *Keck* data.
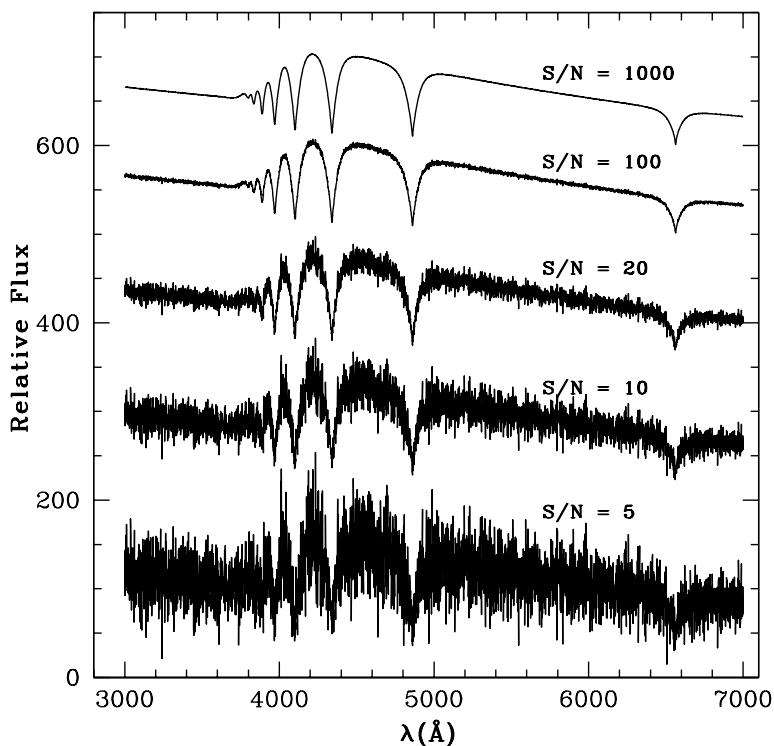
Figure 4.17: Five different synthetic spectra are shown at 3 Å resolution (similar to the *Keck* data) for $T_{\text{eff}} = 16000$ K, log $g = 8.0$, and signal-to-noise 1000 (top), 100, 20, 10, and 5 (bottom).

Figure 4.17 clearly shows that most of our *Keck* spectra, at least the ones that we are fitting for masses, fall between the signal-to-noise = 10 and signal-to-noise = 20 spectra. A few of the brighter Keck spectra, as well as some of the *Gemini* spectra, are of higher signal-to-noise. By matching the resolution of the synthetic spectra to that in the data, we computed many trials of input spectra with a given T_{eff} and log g to see what the

effects were on the derived masses of the stars. The tests were computed using various signal-to-noise values and fitting 2, 3, 4, or 5 Balmer lines. The results are in excellent agreement with our formal uncertainties from the model fits. For example, star K1WD1 is a bright star with five Balmer lines for which we derived $M = 0.61 \pm 0.04 \ M_\odot$. The signal-to-noise of the star is approximately 30. From simulations of stars with the same T_{eff}, log g, and signal-to-noise, the derived mass is found to be $M = 0.62 \pm 0.04 \ M_\odot$. We see a similar agreement between the fitted uncertainties and these uncertainties for fainter stars and for stars with fewer absorption lines. As another example, star GWD5 is a fainter *Gemini* white dwarf with only three Balmer lines. The signal-to-noise of this object is about 20. Our derived mass and uncertainty, $M = 0.83 \pm 0.14 \ M_\odot$ is again in very good agreement with the results from the simulations for this T_{eff} and log g, $M = 0.82 \pm 0.13 \ M_\odot$. In Figure 4.18, we show the results for 500 trials of an input spectrum with $T_{\text{eff}} = 16000$ K, log $g = 8.0$, $M = 0.617 \ M_\odot$, and signal-to-noise $= 20$. The final output histogram has a mean mass of 0.616 $M_\odot$, with a standard deviation of $\sigma = 0.056$.

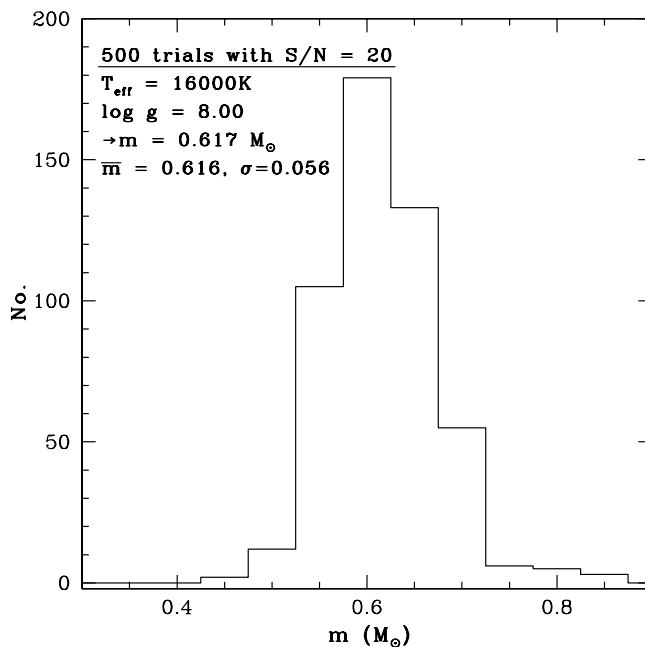Figure 4.18: The distribution of derived stellar masses is shown as a histogram for 500 simulated input stars with signal-to-noise = 20, $T_{\text{eff}} = 16000$ K, log $g = 8.0$, and $M = 0.617 \ M_\odot$. The mean of the distribution is found to be M = 0.616 $M_\odot$ with a standard deviation of σ=0.056.

Given the agreement between the errors derived using the two approaches, we have

chosen to use the formal uncertainties from the fitting routines. The reason is that these values also incorporate other deficiencies in the actual data, such as poor flux calibration, as opposed to the synthetic method where the errors are based solely on the signal-to-noise. In almost every case, the fitted errors are found to be slightly larger than those from the synthetic method. For the two stars where we used the pseudo-spectroscopic method, we use errors from the synthetic method. The systematic errors in the spectroscopic technique are known to be very small at these temperatures, as discussed in §4.6.1.

Determining White Dwarf Cooling Ages and Progenitor Masses

We determine the white dwarf cooling ages from the same models that were used to derive the masses (Wood 1995). The white dwarf cooling age of each star represents the time the star has taken to traverse from the tip of the AGB down to its current location on the white dwarf cooling sequence in the CMD. We can now determine the progenitor mass of the star that created the white dwarf. This is done by first calculating the progenitor lifetime by subtracting the white dwarf cooling age from the cluster age of 650 Myrs (§4.4). This progenitor age now represents the lifetime of the star that created the white dwarf ($t_{\rm ms}$). The age includes post-main sequence evolutionary phases up to the tip of the AGB. We use the models of Hurley, Pols & Tout (2000) for metallicity $Z = 0.01$ and calculate the resulting masses from an automated routine kindly provided by Jarrod Hurley. Table 4.3 summarizes the derived theoretical parameters for all white dwarfs, as well as the calculated initial progenitor lifetimes and masses. Also shown are 1-σ errors in each of the parameters.

Star	$T_{\rm eff}$ (K)	$\log (g)$	$M_{\rm f}$ ($M_\odot$)	M_V	$t_{\rm cool}$ (Myrs)	$t_{\rm ms}$ (Myrs)	$M_{\rm i}$ ($M_\odot$)
K1WD5	18200 ± 400	8.27 ± 0.08	0.79 ± 0.05	11.31	208 ± 26	442 ± 26	$2.98^{+0.07}_{-0.06}$
K1WD8	13100 ± 500	8.34 ± 0.10	0.82 ± 0.06	11.98	573 ± 87	77 ± 87	$6.04^{+?}_{-1.68}$
K1WD2	19300 ± 400	8.20 ± 0.07	0.74 ± 0.04	11.09	156 ± 19	494 ± 19	$2.87^{+0.04}_{-0.04}$
K2WD8	18700 ± 1100	8.82 ± 0.24	1.11 ± 0.12	12.23	540 ± 251	110 ± 251	$5.15^{+?}_{-1.94}$
GWD7	17800 ± 1400	8.42 ± 0.32	0.88 ± 0.20	11.58	321 ± 153	329 ± 153	$3.32^{+0.89}_{-0.43}$
GWD5	18300 ± 1000	8.33 ± 0.22	0.83 ± 0.14	11.40	247 ± 80	403 ± 80	$3.09^{+0.26}_{-0.20}$
GWD4	16900 ± 1100	8.40 ± 0.26	0.87 ± 0.16	11.65	346 ± 127	304 ± 127	$3.42^{+0.80}_{-0.41}$
GWD3	18300 ± 900	8.23 ± 0.21	0.76 ± 0.13	11.22	207 ± 64	443 ± 64	$2.99^{+0.17}_{-0.15}$
GWD2	19900 ± 900	8.11 ± 0.16	0.69 ± 0.10	10.90	131 ± 39	519 ± 39	$2.81^{+0.09}_{-0.06}$
K1WD7	11300 ± 200	8.35 ± 0.15	0.82 ± 0.10	12.30	815 ± 171	$- \pm 171$	7
K1WD9	12300 ± 400	8.72 ± 0.10	1.06 ± 0.05	12.76	1289 ± 232	$- \pm 232$	7
K1WD3	23000 ± 600	8.54 ± 0.10	0.97 ± 0.06	11.34	161 ± 32	489 ± 32	$2.88^{+0.07}_{-0.07}$
K1WD6	11400 ± 200	7.73 ± 0.16	0.46 ± 0.08	11.35	349 ± 64	301 ± 64	$3.43^{+0.33}_{-0.24}$
K1WD4	13300 ± 1000	7.91 ± 0.12	0.56 ± 0.07	11.32	344 ± 76	306 ± 76	$3.42^{+0.39}_{-0.27}$
K1WD1	15300 ± 400	8.00 ± 0.08	0.61 ± 0.04	11.19	228 ± 32	423 ± 32	$3.03^{+0.09}_{-0.07}$
GWD1	16500 ± 800	7.75 ± 0.19	0.49 ± 0.09	10.70	131 ± 38	519 ± 38	$2.81^{+0.08}_{-0.06}$
K2WD5	17200 ± 2000	8.14 ± 0.50	0.85 ± 0.29	11.20	261 ± 100	389 ± 100	$3.13^{+0.36}_{-0.25}$
GWD6	17200 ± 1600	8.90 ± 0.40	0.92 ± 0.21	12.53	300 ± 100	350 ± 100	$3.25^{+0.44}_{-0.28}$

Table 4.3: Derived parameters of white dwarfs

A key result from this work is that we can now, for the first time, provide a bona-fide white dwarf cooling age of a star cluster. Previously, such measurements were limited to using white dwarf candidates identified in imaging projects. For example, Richer et al. (1998) looked at white dwarfs in M67 and von Hippel & Gilmore (2000) searched in NGC 2420. The difficulties in these studies were that the photometry does not extend much fainter than the end of the cooling sequence and that the termination of the white dwarf cooling sequence is buried in field stars or unresolved galaxies making it very difficult to actually isolate it on the CMD. The statistics in these clusters do show that the end of the cooling sequence has been reached, but the results are affected by large errors.

In NGC 2099, we can spectroscopically select the white dwarfs and determine the star cluster age by finding the cooling age of the faintest white dwarf and adding in the main-sequence lifetime of that star. The NGC 2099 CMD clearly shows evidence of a clump which terminates at $V \sim 23.5$. In Kalirai et al. 2001c, we used this limit to derive the white dwarf cooling age of the cluster as 560 Myrs. We can now update this value by using K1WD9, the faintest observed white dwarf ($V = 23.66$). We also point out here that the two objects which are fainter than this star, and included in our sample, are not white dwarfs, thereby strengthening the measurement from K1WD9. As Figure 4.5 shows, K1WD9 falls near the 0.9 $M_\odot$ white dwarf cooling sequence. For a 0.9 $M_\odot$ cooling sequence, the cooling age of this star is measured to be 590 Myrs. This is therefore a lower limit to the age of the cluster, as the progenitor star of this white dwarf would have spent some time on the main sequence and in post-main sequence evolutionary phases. The latter, for a canonical mass of 7 $M_\odot$ is 50 Myrs. The white dwarf cooling sequence is therefore in good agreement with the main-sequence turn-off age presented in §4.4 (650 Myrs).

In Figure 4.19 we present theoretical white dwarf isochrones in the M–$T_{\rm eff}$ plane. The isochrones were constructed from a multi-step process. First, an initial distribution of stars ranging from the present day turnoff of the cluster up to 8 $M_\odot$ is produced. Lifetimes up to the tip of the AGB of these stars are derived from the Hurley, Pols & Tout (2000) models for $Z = 0.01$. White dwarf cooling ages are then calculated by subtracting this lifetime from the cluster age. White dwarf masses are calculated from a metal-poor theoretical white dwarf initial-final mass relationship (Marigo 2001). The resulting masses can now be interpolated from the Wood (1995) models to derive $T_{\rm eff}$. The M–$T_{\rm eff}$ plane (Figure 4.19) shows an obvious "string" of white dwarfs with a few outliers. The 650 Myr isochrone matches a number of these data points very well. Other, less massive, white dwarfs are found to be discrepent with the 650 Myr isochrone, yet they are still younger than an age of 750 Myrs. This age measurement is distance independent, and is in very good agreement with the age we found from fitting the turn-off in §4.4. As we will see

later when we present the initial-final mass relationship for these white dwarfs, the fact that all of these white dwarfs do not sit along one age sequence tells us that the theoretical initial-final mass relationship that we have chosen here may not follow the observed data. The tight sequence of data points has little scatter in the temperature axis, but this is expected given the formation of these stars in a star cluster. First, the white dwarf cooling sequence is only 1 magnitude long and therefore does not cover a large temperature range on the CMD. Hotter white dwarfs are not expected in large numbers given the relatively short amount of time a white dwarf spends early in its cooling phase. Cooler white dwarfs are, of course, not expected given that cluster has a finite age and so the white dwarfs have not had a chance to release enough stored thermal heat. The outliers that do not agree with the isochrones may represent field white dwarfs in our data.
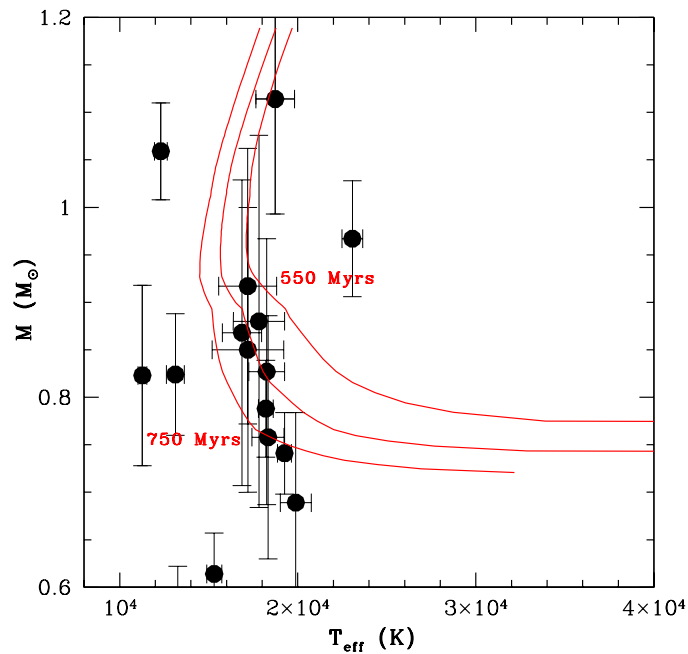

Figure 4.19: The distribution of white dwarfs in the M–$T_{\rm eff}$ plane is shown with error bars. White dwarf isochrones for 550 Myrs, 650 Myrs, and 750 Myrs are found to be in good agreement with the observed sequence of tight data points. The small scatter in $T_{\rm eff}$ of the data points is a consequence of the young age of this star cluster (i.e., it is not old enough for white dwarfs to have cooled any more). The 1-σ error bars are those from fitting the spectral models.

4.6.3 Analysis

In total, we have measured masses, cooling ages and progenitor lifetimes for 18 distinct white dwarfs in this project. This includes 10 *Keck* and 6 *Gemini* objects through the spectroscopic fitting method from §4.6.2, and two objects from the pseudo-spectroscopic mass measuring technique in §4.6.2. Recall that 2 stars were shown twice in the 19 spectra from Figures 4.13–4.16, one of which was measured using the pseudo-spectroscopic technique instead, and one additional object was measured using the pseudo-spectroscopic method.

The derived masses are well constrained for most stars (see Table 4.3). A few of the *Gemini* white dwarfs have larger error bars because fewer absorption lines were available in the fitting. The white dwarf cooling ages are mostly very well constrained, although two of the progenitor lifetimes clearly do not make sense. Stars K1WD7 and K1WD9 have unphysical negative lifetimes, due to the white dwarf cooling age being larger than the cluster age. This inconsistency gives us some idea of the size of the errors in our values, as well as the uncertainties in both the cooling models and the age of the cluster. A similar discrepency has been seen in similar studies as well, depending on whose age measurements one uses for a cluster, for example in the case of the single Pleiades white dwarf (see Williams 2002). The initial masses of these stars will contain large errors, given that the longer cooling ages produce initial stars with short lifetimes and hence larger masses. A change of just 40 Myrs in the lifetime of the star up to the AGB results in roughly a 2 $M_\odot$ difference in the mass for stars in the mass range 6–8 $M_\odot$. We will discuss the direct implications of this on the white dwarf initial-final mass relationship in the next section. For the initial progenitor mass of these two stars we set the mass to 7 $M_\odot$ as this is the upper mass limit to white dwarf production in the stellar evolutionary models that we are using (F. D'Antona, 2004, private communication).

For the three stars in common, we derive very similar parameters from the two independent photometry sets. For example, star K2WD4 has $M = 0.739 \pm 0.080$ $M_\odot$, whereas the same star in the *Gemini* data (GWD2) has $M = 0.689 \pm 0.095$ $M_\odot$. Another example is star K2WD3, which has $M = 0.488 \pm 0.091$ $M_\odot$ and star GWD1 which has $M = 0.485 \pm 0.088$ $M_\odot$. The other combination of common stars, K2WD7 and GWD6, is not usable for this comparison, as K2WD7 could not be fit using the spectroscopic technique and GWD6 was fit using the pseudo-spectroscopic technique. The two *Keck* stars that were fitted and are in common both come from field 2. As we discussed in §4.3.2, large air-masses towards the end of the observing night resulted in missing flux from the blue end of the slit. This is not believed to have affected the fitting of masses, given that the method used to normalize the continuum would compensate for any smooth trends in the flux calibration (see §4.6.1). In total, three of our white dwarfs that were fit with

masses came from field 2. The similar masses between the only two of these three stars for which we have *Gemini* data confirms that the missing flux problem does not affect the final masses of the stars. We will assume that the derived mass of the third object is also not affected.

As we mentioned in §4.4 we expect 30% of our white dwarfs to be field stars. We would also expect some of the objects to have suffered binary star evolution and mass transfer, thereby contaminating the initial-final mass relationship. We believe that binary evolution is a significant factor in the more compact cluster NGC 6819 and less of a concern in NGC 2099. In NGC 6819, Hurley & Shara (2003) have used the Kalirai et al. 2001b data to demonstrate that the observed white dwarf cooling sequence may in fact be two sequences, one from those stars which follow single star evolution, and one from those that are affected by mass transfer (see §3.6.1). NGC 2099 does not show any such obvious effect, although the white dwarf clump is not very tight, making it difficult to observe. To try and separate out field white dwarfs, as well as those that may be affected by binary evolution, we can compare the theoretical luminosities of the white dwarfs with their observational magnitudes. For binaries, the spectra from two white dwarfs will simply co-add and give a mass, whereas the theoretical magnitude will be fainter than the observational magnitude which measures the light from two stars. This potential "over-luminosity" can discriminate binaries. For field white dwarfs, the theoretical magnitudes should disagree with the observational magnitudes, given that we have applied the wrong distance modulus to the star (unless it is a disk white dwarf near the location of the cluster).

In Figure 4.20, we plot the resulting distribution of theoretical magnitudes versus observational magnitudes for the 18 white dwarfs in Table 4.3. There is very good agreement between the theoretical luminosities derived from the spectral line fits, and the observational luminosities derived from the photometry. Most of the data points sit near the solid line which equates the two magnitudes. There are four stars for which the agreement is not so good, the brightest object and the three faintest objects. We will flag these four objects for further inspection.

4.7 The Initial-Final Mass Relation

With both initial and final masses derived, we can now plot our initial-final mass relationship. First, we recall from §4.2 that there have been a number of previous studies providing some data points on the initial-final mass plane. We summarize all of these studies below.

Table 4.4 gives the final and initial masses of white dwarfs in the Hyades, Praesepe,
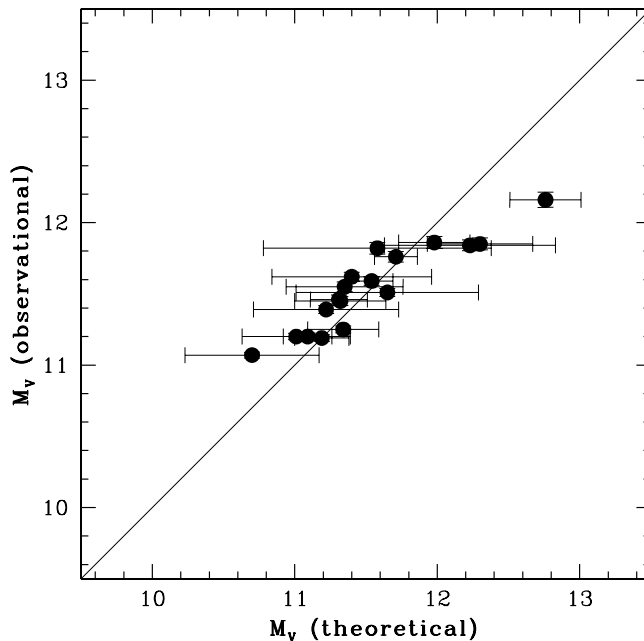
Figure 4.20: The theoretical magnitudes from the spectral fits of the white dwarfs in NGC 2099 are compared to their observational magnitudes assuming a distance modulus of $(m-M)_V = 11.5$ to the cluster. The two objects with pseudo-spectroscopic masses have been fitted for the correct distance to the cluster. The 1-σ error bars are very small in the observed axis, and much larger in the theoretical direction.

Pleiades, NGC 3532, and NGC 2516. For the Hyades, Praesepe and Pleiades clusters (see Claver et al. 2001 and references therein) the masses of all white dwarfs, and progenitors are calculated with the same Wood (1995) models that we use earlier. For NGC 3532, we use the values presented in Table 4 of Koester & Reimers (1993) for the three white dwarfs they discovered. The four NGC 2516 white dwarfs are taken from Koester & Reimers (1996).

The errors for these white dwarfs have not been computed in a homogeneous way. We include them in Table 4.4 for completeness, but will not use them when describing the initial-final mass relationship in any relative context. Depending on the authors, some of the errors above include uncertainties in cluster ages, or in white dwarf cooling models, whereas others do not.

In Figure 4.21 we plot the white dwarf initial-final mass relationship with all previous data points (top) and with our 18 white dwarfs from this study (red dots; bottom). First,

Star	M_f $(M_\odot)$	M_i $(M_\odot)$
Hyades and Praesepe		
WD0836+201	0.62 ± 0.03	$3.04^{+0.05}_{-0.04}$
WD0836+199	0.83 ± 0.04	$4.12^{+0.67}_{-0.40}$
WD0837+199	0.82 ± 0.03	$3.25^{+0.07}_{-0.06}$
WD0840+200	0.75 ± 0.03	$3.69^{+0.18}_{-0.15}$
WD0836+197	0.91 ± 0.03	$2.99^{+0.03}_{-0.03}$
WD0352+098	0.71 ± 0.03	$3.42^{+0.11}_{-0.09}$
WD0406+169	0.80 ± 0.03	$3.55^{+0.14}_{-0.12}$
WD0421+162	0.68 ± 0.03	$2.93^{+0.03}_{-0.03}$
WD0425+168	0.70 ± 0.03	$2.81^{+0.01}_{-0.01}$
WD0431+125	0.65 ± 0.03	$2.85^{+0.02}_{-0.02}$
WD0438+108	0.68 ± 0.03	$2.77^{+0.01}_{-0.01}$
WD0437+138	0.75 ± 0.03	$3.67^{+0.23}_{-0.18}$
Pleiades		
WD0347+247	1.09 ± 0.02	7
Other clusters		
NGC3532-8	0.60 ± 0.06	$3.72^{+1.44}_{-0.490}$
NGC3532-9	0.61 ± 0.05	$3.66^{+1.24}_{-0.470}$
NGC3532-10	0.91 ± 0.10	$5.74^{+1.91}$
NGC2516-1	0.91 ± 0.10	$5.60^{+0.35}_{-0.23}$
NGC2516-2	1.05 ± 0.06	$5.45^{+0.19}_{-0.16}$
NGC2516-3	0.98 ± 0.04	$6.97^{+2.13}_{-0.77}$
NGC2516-5	1.02 ± 0.06	$5.95^{+0.88}_{-0.47}$

Table 4.4: Previous constaints on the initial-final mass relation - see text for references

it is worth noting that in this study we have almost doubled the number of data points on the relationship, the previous points having taken 25 years to establish. Furthermore, half of our data points sit along a very tight sequence with initial masses in the range 2.8—3.5 $M_\odot$ and final masses in the range 0.70–0.90 $M_\odot$. In §4.4 we estimated that most of our white dwarfs should come from stars above 2.5 $M_\odot$, and not too far above this mass, given the present day mass of the turn-off of NGC 2099. We also predicted that most of our white dwarfs should be ~ 0.8 $M_\odot$ given that the white dwarf cooling model for this mass agreed best with the location of our white dwarfs. Therefore the imaging observations of NGC 2099 are in agreement with this independent spectroscopic study. The very tight correlation that is seen in Figure 4.21 is not seen in any of the previous studies and reflects the advantages of using a homogeneous sample to attack the

relationship, rather than relying on data points from several clusters analyzed by various investigators and using different models.
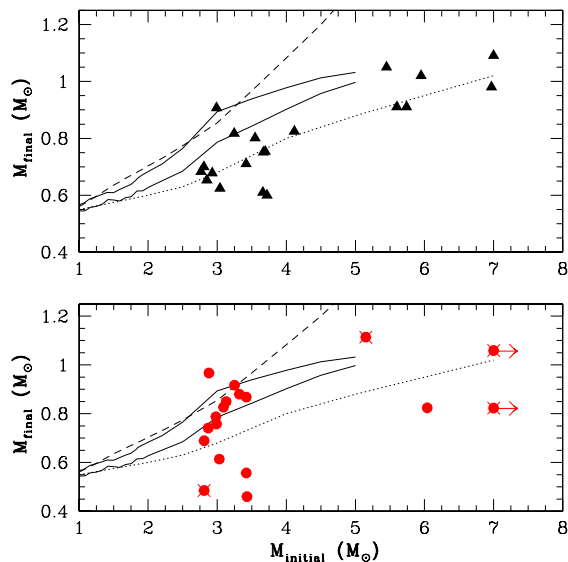

Figure 4.21: The white dwarf initial-final mass relationship is shown for all previous work (black triangles; top) and data in this work (red dots; bottom). Half of the NGC 2099 white dwarfs form a very tight sequence with initial masses between 2.8 and 3.5 $M_\odot$ and final masses between 0.70 and 0.90 $M_\odot$. Outliers are discussed in §4.7. Crosses represent those objects with inconsistent theoretical magnitudes. Also shown is the revised Weidemann (2000) empirical initial-final mass relation (dotted) as well as theoretical relations from Girardi (2000 - dashed), and improved relations from Marigo (2001) for $Z = 0.008$ (solid; top) and $Z = 0.02$ (solid; bottom). The NGC 2099 data points sit between the two Marigo (2001) relations, as expected given the cluster metallicity. The NGC 2099 points also sit systematically above the other data points, as expected given the lower cluster metallicity.

There are a few outliers in Figure 4.21 that need to be discussed. First, we note that the two objects that we measured using the pseudo-spectroscopic technique fit very nicely in the stream of data points located between 2.5 and 3.5 $M_\odot$. White dwarf K2WD5 has $M_f = 0.85$ $M_\odot$ and $M_i = 3.13$ $M_\odot$, while white dwarf GWD6 has $M_f = 0.92$ $M_\odot$ and $M_i = 3.25$ $M_\odot$. The two objects with arrows pointing to larger masses are those objects, K1WD7 and K1WD9, which were presented in §4.6.3 as having longer white dwarf cooling ages than the age of the cluster. We have plotted these two stars at lower limit initial

masses of 7 $M_{\odot}$, the upper mass limit to white dwarf production according to the models we use in §4.4. Two other white dwarfs, K2WD8 and K1WD8, are also found at high initial masses. The spectral fitting of these objects is accurate and consistent with the values obtained using the pseudo-spectroscopic technique. We believe that these objects are most likely examples of more massive initial stars in NGC 2099. The absence of a distribution between these two stars and the rest may be a selection effect given that we have not obtained spectroscopy of the entire cluster white dwarf sample and the relative numbers of these massive progenitors is small compared to the stars with masses just above the turnoff. Finally, there is a group of four white dwarfs which appear to be under-massive for this cluster. For three of these objects, there is no obvious discrepency between the theoretical luminosity and the observed luminosity, and therefore we can not rule them out as being field white dwarfs (the crosses show those objects with inconsistent theoretical magnitudes). It is possible that these are field white dwarfs located near the location of the cluster. It is also possible that these stars may have suffered some binary interactions and mass loss during their evolution and are therefore under-massive. In total, half of these eight outliers have theoretical magnitudes that differ from the observed luminosities as found in §4.6.3. This reflects 22% of the entire sample of white dwarfs and therefore is in decent agreement with the expected 30% that should be field white dwarfs. A faint proper motion analysis of this cluster would be very useful in discriminating non-cluster objects from cluster objects.

We have plotted several theoretical and semi-empirical relations in Figure 4.21. The dotted line is the revised semi-empirical initial-final mass relationship from Weidemann (2000). The dashed line is the theoretical initial-final mass relationship from the Padova group stellar evolution models (Girardi et al. 2000; L. Girardi, 2004, private communication) for $Z = 0.008$. The two solid lines are theoretical initial-final mass relations from Marigo (2001), for $Z = 0.008$ (top) and $Z = 0.02$ (bottom). The latter models have improved mass-loss mechanisms in their post-main sequence evolutionary phases and therefore should be preferred over the others (L. Girardi, 2004, private communication). Considering this, it is interesting to note that the majority of our NGC 2099 cluster white dwarfs reside in a region of the initial-final mass relationship bound by the two Marigo (2001) relations. This is what we would expect, given that the cluster metallicity falls between that used in the two models ($Z = 0.011$). We point out however that the errors in our measurements are too large for us to be able to discriminate between the two relations (see below). Our data points are, however, systematically located above the other previous estimates. This can also be explained by the fact that all of the other clusters are solar or higher metallicity, resulting in more efficient mass loss during stellar evolution. Not only are we almost doubling the available data on this very fundamental

stellar evolution relation, but we may be also beginning to see the effects of metallicity on the initial-final mass relationship.

In Figure 4.22 we plot the same diagram as in Figure 4.21, except we also include the error bars. The errors in the cooling ages have been determined from the errors in the derived final masses of the stars (see §4.6.2). From this, we compute the lifetimes of the progenitor stars and their uncertainties. The effects of an uncertainty in the cluster age will be evaluated below. We then use the Hurley, Pols & Tout (2000) models to determine the uncertainties in the derived initial mass, based on the uncertainties in the progenitor lifetimes. An expanded view of the white dwarfs in the tight sequence of points with initial masses 2.8–3.5 $M_\odot$ is also shown in the bottom panel of Figure 4.22.
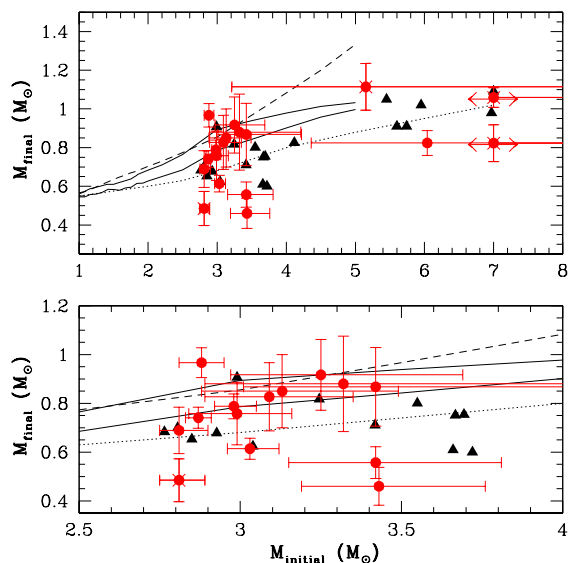

Figure 4.22: As in Figure 4.21 but with error bars (see text). The bottom panel presents an expanded view of those white dwarfs with initial masses between 2.8 and 3.5 $M_\odot$

In §4.4 we determined the age of NGC 2099 to be 650 Myrs. Given the progenitor lifetimes of 14/18 of our white dwarfs, the location of these points will shift by $\sim 0.2\ M_\odot$ in initial mass for a change of 50 Myrs in the age of NGC 2099. This effect, therefore, would not alter the conclusions that we draw above. The other four white dwarfs with smaller progenitor lifetimes, and therefore higher initial masses, would be more affected, given the larger sensitivity of masses for younger ages. These objects contain larger error bars and, as discussed above, have theoretical magnitudes that are inconsistent with the observed brightnesses. A much better constraint on this part of the initial-final mass relationship

can be made by using the white dwarfs that we found in Chapter 3. With an age of only 180 Myrs, all white dwarfs in NGC 2168 must have originated from stars with initial masses greater than $\sim 5~M_\odot$, and therefore we suspect that we would see a tight sequence of points at higher masses, similar to what we see from this project between 2.8 and 3.5 $M_\odot$. We could also constrain the lower mass range of this relationship by observing white dwarfs in NGC 6819, which has a turnoff mass of $\sim 1.6~M_\odot$.

The string of points between 2.8 and 3.5 $M_\odot$ contain final masses ranging from ~ 0.7 to 0.9 $M_\odot$. If we connect these points with a straight line, it is remarkable to see that the amount of mass lost for any star is $\sim 75\%$, with a very small scatter. This powerful constraint illustrates that stars with masses 2.8 and 3.5 $M_\odot$ and metallicities slightly less than the Sun will lose 3/4 of their mass through stellar evolution. By observing white dwarfs in other clusters, we will be able to make similar statements across the entire mass range of intermediate and low mass stars.

We defer the conclusions of this project to the next chapter, where we conclude the thesis.

Chapter 5

Conclusions

We have presented three different studies of white dwarf stars and discovered a number of interesting results. First, in Chapter 2 we used very deep *HST* imaging to probe the inner halo in search of white dwarfs. These objects are believed to possibly comprise 20% of the Galactic dark matter. Our search, does not find these dark matter white dwarfs but does successfully find white dwarfs from each of the other three components of our Galaxy, the thin disk, the thick disk, and the spheroid. In Chapter 3, we provided a detailed step-by-step decomposition of two very young star clusters NGC 2168 and NGC 2323. The photometry for these clusters yielded many interesting scientific results, including the potential discovery of several very high mass white dwarfs. These objects represent the only available sample of such white dwarfs and are sure to provide unprecedented constraints on the initial-final mass relationship. Finally, in Chapter 4 we presented the first large homogeneous project to spectroscopically measure the masses of white dwarfs in an open star cluster. Eighteen of the white dwarfs that were identified in NGC 2099 were fit with atmospheric models to derive their masses, as well as those of the progenitor stars that created the white dwarfs. We find all of our white dwarfs to be of DA spectral class. Based on field ratios, we expected 4 of these objects to be DB, and therefore there is some evidence that the DA/DB ratio for massive white dwarfs is different than for less massive objects. The spectroscopic confirmation of these white dwarfs provides us with the first ever true measurement of the white dwarf cooling age for a star cluster, 640 Myrs for NGC 2099. The masses of these white dwarfs provide constraints on a key part of the initial-final mass relationship, improving on what has been possible in the past. For the first time, we may be seeing metallicity effects on the initial-final mass relationship, proof that stars with higher metal abundances have more efficient mass loss mechanisms. We have convincingly shown that stars with initial masses between 2.8 and 3.5 $M_\odot$ lose 75% of their mass through stellar evolution.

The first project in this thesis is distinct from the other two in that we use white dwarfs to better understand the make-up of our Galaxy. The second and third projects concentrate more on learning about fundamental ingredients of stellar evolution. The initial-final mass relationship has eluded constraints for several decades and were it not for the enormous efforts of D. Koester, D. Reimers and V. Weidemann, we would still

not understand this basic phase of stellar evolution. Now, with the power of the *Gemini North* and *Keck* telescopes, we are hopeful that we can populate this diagram with over 100 data points in the near future. To this end, I have been heavily involved in continuing observations of rich open star clusters to find more white dwarfs. I have successfully been granted more *CFHT* time in the coming semester to observe two very young open star clusters, NGC 6705 (M11) and NGC 7654 (M52), which will hopefully increase the number of data points available for the high mass region of the initial-final mass relationship. We also have on-going programs at both *Gemini* and *Keck* to continue obtaining spectroscopy of white dwarfs in other clusters, such as those that we identified in NGC 6819 and NGC 2168.

In Figure 5.1, I present the CMDs of the first six clusters that we have looked at in our *CFHT* Survey. This includes four of the clusters that have been discussed in this project, as well as two others that comprise the undergraduate thesis work of Doris Leong and Rob Eakin, students at UBC. By working closely with these students and training them to use the tools that we have developed to analyze star cluster photometry, we have increased the sample size of available white dwarfs for spectroscopy. The panels in Figure 5.1 are arranged from the oldest cluster ($\sim$ 10 Gyrs, top-left) to the youngest ($\sim$ 100 Myrs, bottom-right). Clearly, the entire age range, and therefore progenitor mass range, can be explored through the use of open star clusters as probes of white dwarfs. In just 5 years, from the time the first proposal was written to *CFHT* to obtain the photometry in the original Survey, we have become the only group in the world with a systematic plan for attacking the initial-final mass relationship with many targets. The first results, from NGC 2099, provide much encouragement that this relation will very soon be understood in great depth.

The results from this thesis can be directly applied to other astrophysical measurements. For example, our measurement of the absence of dark halo white dwarfs has important consequences. Our survey represents a deep look into the halo of our Galaxy whereas previous surveys have been much shallower, yet with a larger field of view. What we require to settle the longstanding issue of whether white dwarfs comprise a large fraction of the dark matter is clearly a very deep, wide field image of the Galactic halo. Such studies are now feasible with the new Acquisition Camera on *HST*. Our work shows that such a survey would be sensitive to 10's of white dwarfs in the halo based on a 20% MACHO fraction. The findings could potentially solve the dark matter problem. A more direct application of the results in this thesis can be made by considering the recent work of Hansen et al. (2004), who successfully measured the age of globular cluster M4 using white dwarf cooling theory. The modelling of the observed white dwarf cooling sequence in M4, however, requires an initial-final mass relationship. As we have shown, metallicity

effects may be important in the slope of this relationship, and therefore the results would affect the age of M4 (being a metal-poor cluster). Since globular clusters are believed to be among the oldest populations in the Galaxy, refining this age measurement changes the age of the Galaxy measured from this method. Other results, such as our finding of all DA white dwarfs in NGC 2099, may suggest that cluster environments lead to gas accretion by stars unlike that seen in the field. This is a new finding which would not only constrain dynamical models of accretion, but also help constrain what the thickness of the hydrogen envelope must be in white dwarfs. More importantly, our measurement of the masses of white dwarfs which have $V = 23$–24 represents a big advance over what had been previously possible. Since the luminosity function of white dwarfs rises towards fainter magnitudes, the sample size of accessible white dwarfs has been increased by more than an order of magnitude. This will surely translate to many collaborations and new projects which will advance our understanding of white dwarfs.
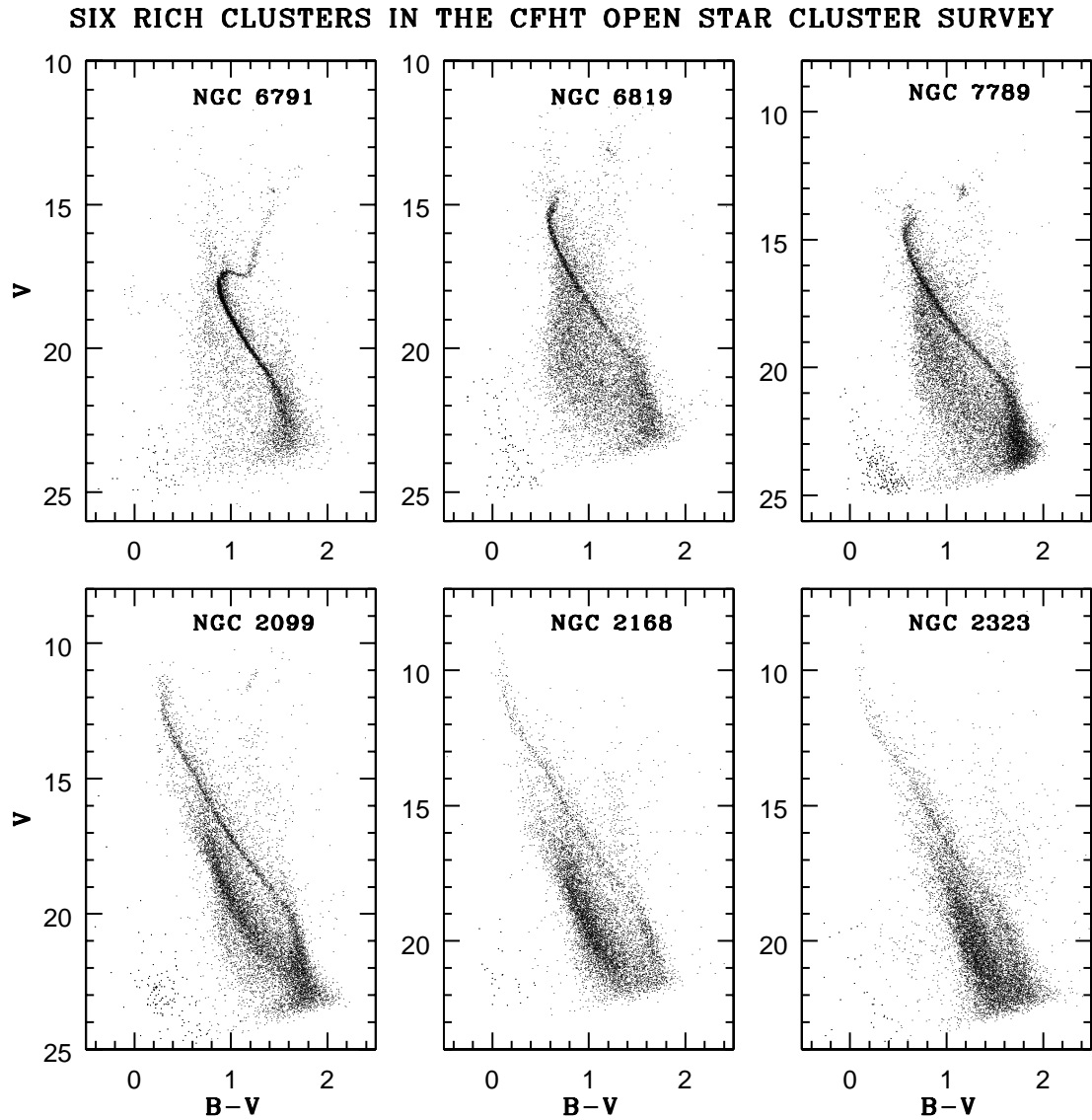
SIX RICH CLUSTERS IN THE CFHT OPEN STAR CLUSTER SURVEY

Figure 5.1: CMDs are presented for the first six open star clusters in the *CFHT* Open Star Cluster Survey. The clusters range from an age of ~ 10 Gyrs (top-left) to ~ 100 Myrs (bottom-right).

Bibliography

[1] Adams, W. S. 1925, PASP, 37, 158

[2] Adams, W. S. 1915, PASP, 27, 236

[3] Alcock, C. et al. 2000, ApJ, 542, 281

[4] Arendt, R. G. et al. 1998, ApJ, 508, 74

[5] Backer, D., & Stramek R. A. 1999, ApJ, 524, 805

[6] Barrado y Navascues, D. et al. 2001, ApJ, 546, 1006

[7] Barrado y Navascues, D., Deliyannis, C.P., & Stauffer, J.R. 2001, ApJ, 549, 452

[8] Barrado y Navascues, D. et al. 1999, Astrophysics and Space Science, 263, 303

[9] Battinelli, P., & Capuzzo-Dolcetta, R. 1991, MNRAS, 249, 76

[10] Bedin, L. R. et al. 2003, ApJL, 126, 247

[11] Bergeron, P., Leggett, S. K., & Ruiz, M. T. 2001, ApJS, 133, 413

[12] Bergeron, P., Ruiz, M. T., & Leggett, S. K. 1997, ApJS, 108, 339

[13] Bergeron, P., Saumon, D., & Wesemael, F. 1995, ApJ, 443, 764

[14] Bergeron, P., Liebert, J., & Fulbright, M. S. 1995, ApJ, 444, 810

[15] Bergeron, P., Saffer, R. A., & Liebert, J. 1992, ApJ, 394, 228

[16] Bergeron, P., Wesemael, F., & Fontaine, G. 1991, ApJ, 367, 253

[17] Bertin, E., & Arnouts, S. 1996, A&AS, 117, 393

[18] Bessell, M.S., Castelli, F., & Plez, B. 1998, A&A, 333, 231

[19] Bessel, F. W. 1844, MNRAS, 6, 136

[20] Bienaymé, O., Robin, A. C., & Crézé, M. 1987, A&A, 180, 94

[21] Binney, J., & Merrifield, M. 1998, Galactic Astronomy (Princeton: University Press)

[22] Binney, J., Gerhard, O., & Spergel, D. 1997, MNRAS, 288, 365

[23] Binney, J., & Tremaine, S. 1987, Galactic Dynamics (Princeton: University Press)

[24] Biretta, L. et al. 2002, WFPC2 Instrument Handbook, Version 7.0 (Baltimore: STScI)

[25] Bradley, P. A. 1994, PASP, 106, 104

[26] Brook, C. B., Kawata, D., & Gibson, B. K. 2003, MNRAS, 343, 913

[27] Canuto, V. M., & Mazzitelli, I. 1992, ApJ, 389, 724

[28] Chabrier, G. 1999, ApJ, 513, L103

[29] Chandrasekhar, S. 1937, ApJ, 86, 623

[30] Chiosi, C., Bertelli, G., & Bressan, A. 1992, ARA&A, 30, 235

[31] Claria, J.J., Piatti, A.E., & Lapasset, E. 1998, A&AS, 128, 131

[32] Clark, A. G. 1862, MNRAS, 22, 170

[33] Claver, C. F. et al. 2001, ApJ, 563, 987

[34] Cole, A. A., & Weinberg, M. D. 2002, ApJ, 574, L43

[35] Crampton, D. et al. 2000, SPIE, 4008, Optical and IR Telescope Instrumentation and Detectors, 114

[36] Cudworth, K. M., & Rees, R. 1990, AJ, 99, 1491

[37] Cuillandre, J. -C. et al. 2000, in Astronomical Telescopes and Instrumentation, Proc. SPIE, 4008, 1010

[38] D'Antona, F. 1998, ASP Conference Series, 142, 157

[39] de Bruijne, J.H.J., Hoogerwerf, R., & de Zeeuw, P.T. 2001, A&A, 367, 111

[40] Dehnen, W., & Binney, J. J. 1998, MNRAS, 298, 387

[41] Dinescu, D. I. et al. 1999, AJ, 117, 277

[42] Dinescu, D. I. et al. 1997, 191st AAS Meeting, 98.03, Bulletin of the American Astronomical Society, 29, 1367

[43] Djorgovski, S. 1993, in ASP Conf. Proc. 50, Structure and Dynamics of Globular Clusters, ed. S. G. Djorgovski, & G. Meylan (San Francisco: ASP), 373

[44] Feast, M., & Whitelock, P. 1997, MNRAS, 291, 683

[45] Flynn, C. et al. 2001, MNRAS, 322, 553

[46] Fontaine, G., Brassard, P., & Bergeron, P. 2001, PASP, 113, 409

[47] Fontaine, G. et al. 1996, ApJ, 469, 320

[48] Fontaine, G., & Brassard, P. 1994, in Proceeding of IAU Colloquium 147, Cambridge: Cambridge University Press, edited by Gilles Chabrier and Evry Schatzman, 347

[49] Francic, S.P. 1989, AJ, 98, 888

[50] Frogel, J. A., Tiede, G. P., & Kuchinski, L. E. 1999, AJ, 117, 2296

[51] Fusi-Pecci, F., & Renzini, A. 1976, A&A 46, 447

[52] Gerhard, O. 2002, ASP Conf. Proc. 273, The Dynamics, Structure & History of Galaxies: A Workshop in Honour of Professor Ken Freeman, ed. G. S. Da Costa & H. Jerjen (San Francisco: ASP), 73

[53] Gibson, B. K., & Mould, J. R. 1997, ApJ, 482, 98

[54] Girardi, L. et al. 2000, A&AS, 141, 371

[55] Gunn, J. E., & Griffin, R. F. 1979, AJ, 84, 752

[56] Habing, H. 1996, ARA&A, 7, 97

[57] Hansen et al. 2004, astro-ph/0401443

[58] Hansen, B. M. S. et al. 2002a, ApJ, 574, L155

[59] Hansen, B. M. 2001, ApJ, 558, L39

[60] Hansen, B. M. 1999, ApJ, 520, 680

[61] Hauschildt, P. H., Allard, F., & Baron, E. 1999, ApJ, 512, 377

[62] Hoag, A. A., et al. 1961, Publ. US Naval Obs., 17, 7, 347

[63] Holberg, J. B., Oswalt, R. D., & Sion, E. M. 2002, ApJ, 571, 512

[64] Hurley, J. R., & Shara, M. M. 2003, ApJ, 589, 179

[65] Hurley, J. R., Pols, O. R., & Tout, C. A. 2000, MNRAS, 315, 543

[66] Ibata, R. A. 1999, ApJS, 120, 265

[67] Iben, I., & Renzini, A. 1983, ARA&A, 21, 271

[68] Jeffries, R. D. 1997, MNRAS, 288, 585

[69] Kalirai, J. S., & Tosi, M. 2004, MNRAS, 351, 649

[70] Kalirai, J. S. et al. 2004, ApJ, 601, 277

[71] Kalirai, J. S. et al. 2003, AJ, 126, 1402

[72] Kalirai, J. S. et al. 2001c, AJ, 122, 3239

[73] Kalirai, J. S. et al. 2001b, AJ, 122, 266

[74] Kalirai, J. S. et al. 2001a, AJ, 122, 257

[75] Kaspi, V., & Helfand, D. J. 2002, astro-ph/0201183

[76] Kawaler, S. D. 1995, in Astrophysical applications of stellar pulsation, ed. R. S. Stobie and P. A. Whitelock, ASP, 83, 81

[77] Kawaler, S. D. 1991, in Confrontation between Stellar Pulsation and Evolution, ed. C. Cacciari & G. Clemintini (ASP Conf. Ser., 11), 494

[78] Kerr, F. J., & Lynden-Bell, D. 1986, MNRAS, 221, 1023

[79] King, I. R. et al. 1998, ApJ, 492, L37

[80] Kleinman, S. J. et al. 2004, ApJ, 607, 426

[81] Koester, D., & Reimers, D. 1996, A&A, 313, 810

[82] Koester, D., & Reimers, D. 1993, A&A, 275, 479

[83] Koester, D., & Reimers, D. 1981, A&A, 99, L8

[84] Koopmans, L. V. E., & Blandford, R. D. 2001, astro-ph/0107358

[85] Kuijken, K., & Tremaine, S. 1994, ApJ, 421, 178

[86] Kuijken, K., & Gilmore, G. 1991, ApJ, 367, L9

[87] Landolt, A. U. 1992, ApJ, 104, 340

[88] Lee, S., & Sung, H. 1995, JKAS, 28, 1, 45

[89] Leggett, S. K., Ruiz, M. T., & Bergeron, P. 1998, ApJ, 497, 294

[90] Leonard, P. J. T., & Merritt, D. 1989, ApJ, 339, 195

[91] Liebert, J., Dahn, C. C., & Monet, D. G. 1988, ApJ, 332, 891

[92] Lupton, R. 1993, *Statistics in Theory and Practice* Princeton University Press

[93] Madej, J., Nalezyty, M., & Althaus, L. G. 2004, A&A, 419, L5

[94] Marigo, P. 2001, A&A, 370, 194

[95] McCook, G. P., & Sion, E. M. 1999, ApJS, 121, 1

[96] McWilliam, A., & Rich, R. M. 1994, ApJS, 91, 749

[97] Mendez, R. A. 2002, A&A, 395, 779

[98] Merrifield, M. R. 1992, AJ, 103, 1552

[99] Murowinski, R. et al. 2002, SPIE, 4841, Power Telescopes and Instrumentation into the New Millennium

[100] Murray, S. D., & Lin, D. N. C. 1996, ApJ, 467, 728

[101] Nelson, C. A. et al. 2002, ApJ, 573, 644

[102] Oppenheimer, B. R. et al. 2001, Science, 292, 698

[103] Perryman, M.A.C. et al. 1998, A&A, 331, 81

[104] Peterson, R. C., Rees, R. F., & Cudworth, K. M. 1995, ApJ, 443, 124

[105] Press, W. H. et al. 1986, Numerical Recipes, Cambridge: Cambridge Univ. Press

[106] Reid, I. N., Sahu, K. C., & Hawley, S. L. 2001, ApJ, 559, 942

[107] Reid, M. J. et al. 1999, ApJ, 524, 816

[108] Reimers, D., & Koester, D. 1988, A&A, 202, 77

[109] Reimers, D., & Koester, D. 1988b, ESO Messenger, 54, 47

[110] Reimers, D., & Koester, D. 1982, A&A, 116, 2, 341

[111] Renzini, A., & Fusi-Pecci, F. 1988, ARA&A, 26, 199

[112] Richer et al. 2004, AJ, 127, 2771

[113] Richer, H. B. et al. 2002, ApJ, 574, L151

[114] Richer H.B. 2001, astro-ph/0107079

[115] Richer, H.B, et al. 2000, ApJ, 529, Issue 1, 318

[116] Richer, H.B. et al. 1998, ApJ, 504, L91

[117] Richer, H. B., et al. 1997, ApJ, 484, 741

[118] Richer, H. B., et al. 1995, ApJ, 451, L17

[119] Romanishin, W., & Angel, J. R. 1980, ApJ, 235, 992

[120] Saumon, D., & Jacobson, S.B. 1999, ApJ, 511, L107

[121] Sarajedini, A. et al. 2004, AJ, 127, 991

[122] Sarrazine, A. R. et al. 2000, A&AS, 32, 742

[123] Shapiro, S. L., & Teukolsky, S. A. 1983, Black holes, white dwarfs, and neutron stars: The physics of compact objects

[124] Shulz, H., & Wegner, G. 1981, A&A, 94, 272

[125] Somerville, R. S., & Primack, J. R. 1999, MNRAS, 310, 1087

[126] Spergel, D. N. et al. 2003, ApJS, 148, 175

[127] Srinivasan, G. 2002, ARA&A, 11, 67

[128] Stecklum, J. B. 1989, Astron. Nachr. 310, 375

[129] Stetson, P. B. 1987, PASP, 99, 191

[130] Stetson, P. B. 1994, PASP, 106, 250

[131] Sung, H., & Bessell, M.S. 1999, MNRAS, 306, 361

[132] Terndrup, D. M. et al. 1998, AJ, 115, 1476

[133] van den Bergh, S., & Tammann, G. 1991, ARA&A, 29, 363

[134] Ventura, P. et al. 1998, A&A, 334, 953

[135] Vidal, N. V. 1973, A&AS, 11, 93

[136] von Hippel, T., Steinhauer, A., Sarajedini, A., & Deliyannis, C. P. 2002, astro-ph/0206440

[137] von Hippel, T., & Gilmore, G. 2000, AJ, 120, Iss. 3, 1384

[138] Weidemann, V. 2000, A&A, 363, 647

[139] Weidemann, V. 1987, A&A, 188, 74

[140] Weidemann, V., & Koester, D. 1983, A&A, 121, 77

[141] Weidemann, V. 1977, A&A, 59, 411

[142] Wielen, R. 1991, ASPCS, Formation and Evolution of Star Clusters, 13, 343

[143] Wilkinson, M. I., & Evans, N. W. 1995, MNRAS, 310, 645

[144] Williams, K. et al. 2004, submitted to ApJ

[145] Williams, K. A. 2002, PhD thesis, White Dwarfs in Open Clusters: The Initial-Final Mass Relation, The Supernova Mass Limit, and the White Dwarf Deficit.

[146] Williams, R. E. et al. 1996, AJ, 112, 1335

[147] Winget, D. E. et al. 1994, ApJ, 430, 839

[148] Wood, M. A. 1995, in Ninth European Workshop on White Dwarfs, NATO ASI Series, ed. D. Koester, & K. Werner (Berlin: Springer), 41

[149] Wood, M. A. 1990, Ph.D. thesis, Univ. of Texas at Austin

[150] Yi, S. et al. 2001, ApJS, 136, 417

[151] Zinnecker, H., & McCaughrean, M. J. 1994, in Infrared Phys. Technol., Vol. 35, Oxford: Pergamon, 569